Implementation of a multinucleon neutrino interaction simulation and comparison with T2K data

Peter David Sinclair

High Energy Physics group

Imperial College London

A thesis submitted to The Imperial College of Science, Technology and Medicine for the degree of Doctor of Philosophy

May 1, 2014

Abstract

A multinucleon neutrino interaction mode is implemented into the NEUT neutrino interaction generator. The model allows the simulation of fully differential event kinematics and uses the prediction of Nieves et al. for the total cross section and final-state charged lepton kinematics. The model is fit to T2K near-detector data using a Markov chain monte carlo method, and the goodness-of-fit is evaluated.

The CCQE model in NEUT is fit to published data from the MiniBooNE experiment to inform the size of the prior systematic uncertainties associated with the charged-current quasielastic interaction mode. The priors were applied in the 2012 T2K analyses. The fit required development of monte carlo reweighting functions which allowed changes to the nuclear model to be simulated. Both the fits, and the development of the reweighting functions, are discussed in detail.

Contents

List of figures

List of tables

Declaration

I hereby declare that all work described in this thesis is my own, or has been properly attributed.

The material presented in Chapters 2 and 3 describes the main theoretical background to this work. Chapter 4 describes the T2K experiment in general. These chapters serve to place the T2K experiment and the work described in this thesis in a wider context, and contain no original research.

The work described in Chapter 5 makes extensive use of pre-existing software. The NEUT interaction generator was used, as is T2KReWeight, a bespoke T2K Monte Carlo reweighting package. Chapter 5 also makes use of data from the MiniBooNE experiment. The parameter fits described in this chapter use a statistical method based on similar work in a previous analysis, which has been properly credited. The parameter fitter used in the analysis was a pre-existing software package written by T2K collaborators.

Chapter 6 describes the implementation of a multinucleon neutrino interaction mode into the NEUT generator. The interaction model is the work of Juan Nieves and collaborators and has been properly credited. Extensions to the model proposed by others are also credited in the text.

Chapter 6 also describes fits to T2K data using MC simulations with NEUT. The data was collected over the period of several years and is the product of a great amount of work by T2K collaborators. Similarly, the simulation of NEUT events in the T2K detectors is performed by a large suite of software packages, both external to the T2K experiment and bespoke. The fits were performed using code written by T2K collaborators.

Acknowledgements

Over the course of my postgraduate studies I have had the privilege of working with a great number of excellent scientists and educators. Without the support of these colleagues and collaborators this work would not have been possible. To all these I express my sincere thanks.

My supervisor, Dr. Morgan Wascko, for the encouragement and guidance which enabled me to find a path of stimulating research.

Dr. Yoshi Uchida, for his insight and direction.

Dr. Asher Kaboth, for his help and effort which was instrumental in bringing this work to completion, and for his enthusiasm and passion for scientific research.

Dr. Matthew Malek, for his valuable and thoughtful advice. “Learn from everyone.”

Dr. Per Jonsson, for many useful and insightful discussions.

Dr. Ryan Terri for his patience and formative advice throughout my studies.

Dr. Panos Stamoulis, for his tireless work and substantial contributions to this research.

Chapter 1.

Introduction

The questions addressed by the study of particle physics are ancient ones. At least as early as the 6^{th} century BC, philosophers in India and in Greece speculated on the nature of matter, and on the fundimental constituents of the world around them. The questions are also very simple ones: what is the nature of the very smallest elements which exist, and how do they interact? It is precisely because these questions are so simple, and so natural to ask, that they continue to occupy the interest of modern academics.

The modern emphasis on the collection and interpretation of data gives current scientists a significant edge over those early thinkers. Experiments allow us to unambiguously compare our predictions to reality, which in turn helps to guide theoretical development. The combination of theory and experiment has driven the rapid development of particle physics in the 20^{th} and 21^{st} centuries.

The current best description of particle physics is known as the standard model. Put simply, this model argues that symmetries in the laws of nature give rise to particles and the forces between them. It has been an extrordinarily successful idea, and has succeeded in describing with great detail the vast range of datasets with which it has been confronted, including the most recent measurements from the LHC in Geneva. However, there are some observed phenomena which cannot be explained by present theory, and which therefore provide a window into physics beyond the standard model. These processes occur in the neutrino sector, and it is this area which has been the focus of the work described in this thesis.

As with all particles in the standard model, neutrinos can be classified according to their properties within the model. There are six types of neutrino: three neutrinos, each with a flavour corresponding to one of the three generations of leptons—ν_{e}, ν_{μ}, ν_{τ}—and

three antineutrinos of similar flavours, corresponding to the anti-leptons. In the standard model, neutrinos have zero mass and zero charge. All neutrinos are left-handed and have a weak-isospin quantum number of $+1/2$, and all antineutrinos are right-handed, and have weak a weak-isospin quantum number of $-1/2$. The standard model description was sufficient to characterise most neutrino phenomology for most of the 20^{th} century, however, the observation of neutrino oscillations has shown that there is more than just the standard model picture.

Neutrino oscillation is the process whereby a neutrino is created with a given flavour, and has an oscillating probability of being observed as a different flavour as a function of the distance of propagation. This can only happen if at least two neutrino mass eigenstates have non-zero mass—a property clearly outside the standard model description. Further, the parameters describing the form of the oscillations permit a difference between the behaviour of neutrinos and antineutrinos. This difference is an example of a CP-violating process, and could help us understand the observed matter-antimatter asymmetry of the universe, which has been one of the central questions in basic science for many decades.

The T2K experiment is one of the latest generation of experiments designed to measure the properties associated with neutrino oscillation. In T2K, a beam of muon neutrinos is produced, and the flavour profile is characterised just after production and once the neutrinos have propagated for 295 km. Differences in the flavour profile before and after propagation allow us to extract the parameters of interest and characterise the oscillation.

Measurements in T2K are performed by observing the interactions of neutrinos with matter, most often with the nuclei of carbon and oxygen atoms. In T2K analyses, care must be taken to both accurately model the interactions of neutrinos with nuclei, and to characterise any systematic uncertainties associated with the neutrino interactions. These two topics are the focus of this work.

In Chapter 2, the theory of neutrino oscillations is presented in detail, and the current state of the field is reviewed. Attention is paid to the current best measurements and constraints of oscillation parameters, and the place of T2K within the field is established. Chapter 3 presents the theory of neutrino-nucleus interactions in the energy range relevant to the T2K experiment. Most attention is paid to the charged-current quasi-elastic (CCQE) interaction, and the interaction of neutrinos with multiple nucleons. In Chapter 4 the T2K experiment is described, with some focus on the way in which uncertainties on neutrino cross sections enter into the measurement. Chapter 5 presents

original work on the characterisation of systematic uncertainties associated with the CCQE interaction as an input into the T2K oscillation analyses, and describes the creation of software to improve the treatment of cross section parameters in fits to T2K data. The main original research of this thesis is presented in Chapter 6, which describes the creation and implementation of a Monte Carlo simulation to model interactions between neutrinos and multiple nucleons. The updated interaction model is fit to T2K data, and a number of studies are performed to compare the complete model before and after the introduction of the new interaction simulation.

Chapter 2.

Neutrino oscillation theory

The theory of neutrino oscillations is well established, and is explained thoroughly in a number of textbooks. The discussion in this chapter largely follows the plane-wave derivation as explained in the reference [1] with additional notes from [2].

In charged-current interactions, the neutrinos which interact are eigenstates of the flavour operator, so are either of electron, muon or tau-type. In free-space, neutrinos of definite masses propagate. The wave functions of the particles which are eigenstates of the flavour and mass operators are related by the transformation

$$|\nu_\alpha\rangle = \sum_i U^*_{\alpha i} |\nu_i\rangle \tag{2.1}$$

where $|\nu_i\rangle$ $(i = 1, 2, 3)$ are the mass eigenstates, $|\nu_\alpha\rangle$ $(\alpha = e, \mu, \tau)$ are the flavour eigenstates, and U is a 3×3 matrix, usually assumed to be unitary. U is referred to as the Pontecorvo-Maki-Nakagawa-Sakata (PMNS) matrix. Mass states are eigenstates of the Hamiltonian and propagate according to the time-dependent Schrödinger equation as

$$|\nu_i(t)\rangle = e^{-ip_i.r} |\nu_i(0)\rangle \,. \tag{2.2}$$

where p_i is the four-momentum of the neutrino of mass m_i and r is the space-time four-vector traversed by the neutrino. From this we can express a flavour state at a general time

$$|\nu_\alpha(t)\rangle = \sum_i U^*_{\alpha i} e^{-ip_i.r} |\nu_i(0)\rangle \,. \tag{2.3}$$

Using the unitarity of U, we have the relation:

$$|\nu_i\rangle = \sum_\alpha U_{\alpha i} |\nu_\alpha\rangle . \tag{2.4}$$

Consider a process where a neutrino of a definite flavour is created at the point $r = 0$. The flavour state at a general time and position can be expressed in terms of pure flavour states at $r = 0$:

$$|\nu_\alpha(t)\rangle = \sum_\beta \left(\sum_i U^*_{\alpha i} e^{-ip_i.r} U_{\beta i} \right) |\nu_\beta(0)\rangle \tag{2.5}$$

hence neutrino flavour state at a general time is a mixture of the pure flavour states. The amplitude of the transition from flavour state α to flavour state β is

$$A_{\nu_\alpha \to \nu_\beta}(t) \equiv \langle \nu_\beta | \nu_\alpha(t) \rangle = \sum_i U^*_{\alpha i} U_{\beta i} e^{-ip_i.r}. \tag{2.6}$$

The probability of this transition (i.e. the probability of a neutrino produced in flavour α being observed at time t in flavour state β) is the square of this amplitude:

$$P_{\nu_\alpha \to \nu_\beta} = |A_{\nu_\alpha \to \nu_\beta}(t)|^2 = \sum_{i,j} U^*_{\alpha i} U_{\beta i} U_{\alpha j} U^*_{\beta j} e^{-i(p_i - p_j).r}. \tag{2.7}$$

Neutrinos at accelerator energies are relativistic (as indeed are all presently observable neutrinos), so we can use the approximation that

$$E_i \approx |p| + \frac{m_i^2}{2E}, \tag{2.8}$$

where E is the neutrino energy neglecting the contribution from the mass, $|p|$ is the momentum (i.e. $p = (E, \mathbf{p})$), and m_i is the neutrino mass. In the relativistic regime, we also have that $t = L$ where L is the distance travelled by the neutrinos expressed in natural units. The transition probability can then be expressed as

$$P_{\nu_\alpha \to \nu_\beta} = \sum_{i,j} U^*_{\alpha i} U_{\beta i} U_{\alpha j} U^*_{\beta j} e^{-i \frac{\Delta m^2_{ij}}{2E} L}. \tag{2.9}$$

where $\Delta m^2_{ij} = m^2_i - m^2_j$. We see then that the amplitude of the oscillation depends on the elements of the PMNS matrix, and the phase of the oscillation depends on the experimental quantities E and L, as well as the physical quantity Δm^2_{ij}. The transition

amplitudes depend on quartic products of U, not on the specific parameterisation of the matrix. For experimental convenience, the PMNS matrix is normally parameterised as

$$U_{\alpha i} = \begin{pmatrix} 1 & 0 & 0 \\ 0 & c_{23} & s_{23} \\ 0 & -s_{23} & c_{23} \end{pmatrix} \begin{pmatrix} c_{13} & 0 & s_{13}e^{-i\delta} \\ 0 & 1 & 0 \\ -s_{13}e^{i\delta} & 0 & c_{13} \end{pmatrix} \begin{pmatrix} c_{12} & s_{12} & 0 \\ -s_{12} & c_{12} & 0 \\ 0 & 0 & 1 \end{pmatrix} \tag{2.10}$$

where $c_{ij} = \cos\theta_{ij}$, $s_{ij} = \sin\theta_{ij}$ (θ_{ij} are the mixing angles) and δ is a complex phase.

This particular parameterisation came about due to the parameters which were able to be measured in early neutrino oscillation experiments: θ_{12} and θ_{23} are referred to as the solar and atmospheric mixing angles respectively, since experiments using solar or atmospheric neutrinos were primarily sensitive to those mixing angles. This separation came about because the values of Δm^2 associated with these two phenomena are so different, so the wavelengths of the oscillations are different.

The neutrino oscillation probability can be expressed in terms of the real and imaginary parts of the PMNS matrix

$$\begin{aligned} P_{\nu_\alpha \to \nu_\beta}(L, E) = \delta_{\alpha\beta} &- 4 \sum_{i>j} \mathrm{Re}\left[U^*_{\alpha i} U_{\beta i} U_{\alpha j} U^*_{\beta j}\right] \sin^2\left(\frac{\Delta m^2_{ij} L}{4E}\right) \\ &+ 2 \sum_{i>j} \mathrm{Im}\left[U^*_{\alpha i} U_{\beta i} U_{\alpha j} U^*_{\beta j}\right] \sin\left(\frac{\Delta m^2_{ij} L}{2E}\right). \end{aligned} \tag{2.11}$$

This result will be of importance later when comparing to the anti-neutrino case.

Neutrino oscillation in antineutrinos

The hermitian conjugation of neutrino states yields anti-neutrino states. In a similar way to Equation 2.3, the anti-neutrino flavour states can be expressed in terms of the anti-neutrino mass states as

$$|\bar{\nu}_\alpha(t)\rangle = \sum_i U_{\alpha i} e^{iE_i t} |\bar{\nu}_i(0)\rangle \tag{2.12}$$

A similar treatment of the neutrino oscillation process yields the transition probability for anti-neutrinos as:

$$P_{\bar{\nu}_\alpha \to \bar{\nu}_\beta} = \sum_{i,j} U_{\alpha i} U^*_{\beta i} U^*_{\alpha j} U_{\beta j} e^{i \frac{\Delta m^2_{ij}}{2E} L}. \tag{2.13}$$

In a similar way as Equation 2.11, this can be expressed in terms of the real and imaginary parts of the elements of U:

$$\begin{aligned} P_{\bar{\nu}_\alpha \to \bar{\nu}_\beta}(L, E) = \delta_{\alpha\beta} &- 4 \sum_{i>j} \mathrm{Re}\left[U^*_{\alpha i} U_{\beta i} U_{\alpha j} U^*_{\beta j}\right] \sin^2\left(\frac{\Delta m^2_{ij} L}{4E}\right) \\ &- 2 \sum_{i>j} \mathrm{Im}\left[U^*_{\alpha i} U_{\beta i} U_{\alpha j} U^*_{\beta j}\right] \sin\left(\frac{\Delta m^2_{ij} L}{2E}\right). \end{aligned} \tag{2.14}$$

which differs from the equivalent expression for neutrinos by only the sign of the imaginary part.

CP-violation

A CP transformation exchanges neutrinos with negative helicity for anti-neutrinos with positive helicity. This transforms the oscillation channel $\nu_\alpha \to \nu_\beta$ to $\bar{\nu}_\alpha \to \bar{\nu}_\beta$. CP-violation can then be observed by comparing these channels and observing the asymmetry:

$$A^{\mathrm{CP}}_{\alpha\beta} = P_{\nu_\alpha \to \nu_\beta} - P_{\bar{\nu}_\alpha \to \bar{\nu}_\beta} \tag{2.15}$$

The two transition probability terms in this expression differ only by the sign of the imaginary part of the quartic products of U, as in Equations 2.11 and 2.14, so can be expressed as

$$A^{\mathrm{CP}}_{\alpha\beta} = 4 \sum_{i>j} \mathrm{Im}\left[U^*_{\alpha i} U_{\beta i} U_{\alpha j} U^*_{\beta j}\right] \sin\left(\frac{\Delta m^2_{ij} L}{2E}\right). \tag{2.16}$$

For this term to be non-zero there must be an imaginary part of U: the CP-violating phase $e^{-i\delta}$ must have an imaginary component. This asymmetry is the channel through which the CP-violating phase in the PMNS matrix can be measured.

2.1. Current state of knowledge

The field of neutrino oscillation physics emerged from the first observations of a deficit in the expected solar neutrino flux by the Homestake experiment almost half a century ago [3]. Since then, and with increasing pace, the phenomenon of neutrino oscillations was confirmed and many of the associated parameters were measured. Today we are not far from further and potentially more profound insights with the possible measurement of CP violation in the current or next generation of experiments.

This section gives a summary of our knowledge of neutrino oscillation parameters as of early 2014, and describes the present areas of interest in the field. A more complete discussion can be found in the reference [4].

Measurement of solar neutrino parameters

Solar neutrinos are produced by the *pp fusion* reaction in the sun:

$$4p \rightarrow {}^{4}\mathrm{He} + 2e^{+} + 2\nu_e. \tag{2.17}$$

The first observation of the solar neutrino flux was made by Davis *et al.* in the Homestake experiment [3]. In this experiment, the flux of solar neutrinos was observed to be smaller than that expected from the standard solar model. This observation permitted a number of interpretations, including but not limited to neutrino oscillations. Specific evidence for neutrino oscillation was found by the Super Kamiokande and SNO experiments. Super Kamiokande measured the total neutrino flux via elastic interactions on water [5], and SNO measured the electron neutrino flux using charged-current interactions on deuterium [6], and the total interaction rate via the neutral current channel [7]. Taken together, these experiments showed that the total neutrino flux was as expected from the standard solar model, but the flavour composition was not.

Later, KamLAND performed a measurement of the solar parameters using reactor antineutrinos through the channel [8, 9, 10]:

$$\bar{\nu}_e + p \rightarrow e^{+} + n. \tag{2.18}$$

Their latest results constrain solar parameters and show sensitivity to other oscillation parameters:

$$\begin{aligned} \Delta m^2_{21} &= (7.53 \pm 0.18) \times 10^{-5}\text{eV}^2, \\ \tan^2\theta_{12} &= 0.436^{+0.029}_{-0.025}, \\ \sin^2 2\theta_{13} &= 0.023 \pm 0.002. \end{aligned} \tag{2.19}$$

Measurement of atmospheric neutrino parameters

Neutrinos are produced in Earth's atmosphere from the interaction of cosmic rays with air. These reactions produce pions and kaons which then decay to neutrinos. For the case of pions, the reaction chain is:

$$\begin{aligned} \pi^\pm \rightarrow & \mu^\pm + \nu_\mu(\bar{\nu}_\mu), \\ & \mu^\pm \rightarrow e^\pm + \nu_e(\bar{\nu}_e) + \bar{\nu}_\mu(\nu_\mu). \end{aligned} \tag{2.20}$$

Kaons have similar reactions, and can also decay directly to electrons. The flux ratio of muon to electron neutrinos is approximately $\Phi(\nu_\mu + \bar{\nu}_\mu)/\Phi(\nu_e + \bar{\nu}_e) \approx 2$.

First evidence of atmospheric neutrino oscillation came from Super Kamiokande in their 'zenith angle' and 'L/E' measurements [11, 12]. Experiments using neutrino beams from accelerator sources have also been used to measure atmospheric neutrino oscillation parameters. The first was K2K [13] which measured the muon neutrino disappearance channel and reported a result disfavouring no-oscillations at 4.9σ. The second major accelerator neutrino experiment was MINOS. MINOS was was able to measure parameters separately for neutrinos and anti-neutrinos, and reported [14]:

$$\begin{aligned} \sin^2 2\bar{\theta}_A &= 0.97^{+0.03}_{-0.08} \\ \sin^2 2\theta_A &> 0.8390\% \text{ C.L.} \\ |\Delta m^2_A| &= (2.41^{+0.09}_{-0.10}) \times 10^{-3}\text{eV}^2 \\ |\Delta m^2_A| - |\Delta \bar{m}^2_A| &= (0.12^{+0.24}_{-0.26}) \times 10^{-3}\text{eV}^2 \end{aligned} \tag{2.21}$$

where parameters with overbars apply to the antineutrino measurements. MINOS disfavoured maximal mixing for neutrinos ($\theta_A = \pi/4$) at 86% C.L. In a similar measurement

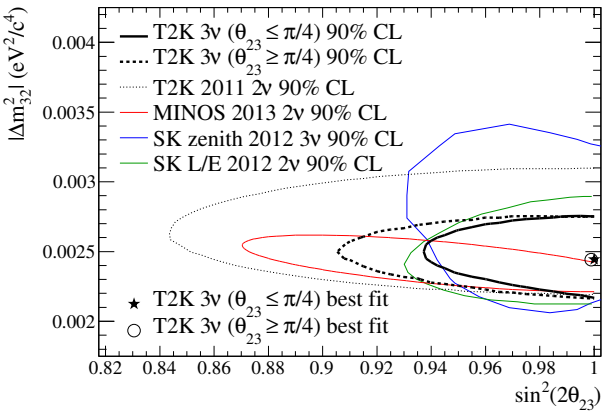

Figure 2.1.: Plot from [16] showing the main competitive constraints on atmospheric oscillation parameters. Data from T2K [15, 16], MINOS [14], and Super Kamiokande [17].

to MINOS, T2K reports [15, 16]:

$$\begin{aligned} \sin^2\theta_{23} &= 0.514 \pm 0.082 \\ |\Delta m^2_{32}| &= (2.44^{+0.17}_{-0.15}) \times 10^{-3}\text{eV}^2 \end{aligned} \tag{2.22}$$

(assuming normal mass hierarchy, $\sin^2 2\theta_{13} = 0.098$, $\Delta m^2_{21} = 7.5 \times 10^{-5}\text{eV}^2$, $\sin^2 2\theta_{12} = 0.857$ and $\delta = 0$). T2K finds no indication of non-maximal mixing.

Figure 2.1 from [16] shows the main competitive constraints on atmospheric neutrino parameters.

Measurement of θ_{13}

θ_{13} has been measured using accelerator neutrinos by T2K and MINOS, and using reactor neutrinos in Daya Bay, RENO and Double Chooz. Previously, θ_{13} was constrained by Chooz using reactor neutrinos.

Reactor experiments measure θ_{13} in the electron antineutrino disappearance channel via the reaction:

$$\bar{\nu}_e + p \rightarrow e^+ + n, \tag{2.23}$$

Prior to 2011, Chooz constrained θ_{13} as [18]:

$$\sin^2 2\theta_{13} \leq 0.17 \tag{2.24}$$

at 90% C.L. for $\Delta m^2 \geq 8 \times 10^{-4}\text{eV}^2$.

In 2011, T2K found indications of non-zero θ_{13} via electron neutrino appearance in a muon beam [19], with 2.5σ significance. Recent T2K results find zero θ_{13} disfavoured at 7.3σ [20, 21]. Assuming $\sin^2 2\theta_{23} = 1$, $\Delta m^2_A = 2.4 \times 10^{-3}\text{eV}^2$, $\delta = 0$, and normal mass hierarchy, T2K finds the best-fit θ_{13} to be:

$$\sin^2 2\theta_{13} = 0.088^{+0.049}_{-0.039} \tag{2.25}$$

Also in 2011, the MINOS collaboration found an indication of non-zero θ_{13} at 89% C.L. [22]. In a recent update, the best-fit parameters are reported as [23]:

$$2\sin^2 2\theta_{13}\sin^2\theta_{23} = 0.051^{+0.038}_{-0.030}, \tag{2.26}$$

(assuming normal hierarchy, $\delta = 0$ and $\theta_{23} < \pi/4$).

Reactor neutrinos measure θ_{13} through $\bar{\nu}_e$ disappearance. Daya Bay currently reports the strongest measurement of θ_{13} from a single experiment [24, 25]:

$$\sin^2 2\theta_{13} = 0.089 \pm 0.010(stat.) \pm 0.005(syst.). \tag{2.27}$$

RENO also measures θ_{13} through the same channel. They report [26, 27]:

$$\sin^2 2\theta_{13} = 0.100 \pm 0.010(stat.) \pm 0.015(syst.). \tag{2.28}$$

Similarly, Double Chooz reports [28, 29]:

$$\sin^2 2\theta_{13} = 0.109 \pm 0.030(stat.) \pm 0.025(syst.). \tag{2.29}$$

Currently the best limits on θ_{13} come from the reactor experiments. However, since the accelerator experiments measure both appearance and disappearance, combining the results of accelerator and reactor experiments can give us insight into the possibility of CP violation in neutrino oscillations.

CP violation in the lepton sector

Figure 2.2 from [21] shows a recent result from T2K, showing the best-fit contour in $\sin^2 2\theta_{13}$ and the CP-violating phase δ. Also shown is the average value of $\sin^2 2\theta_{13}$ from

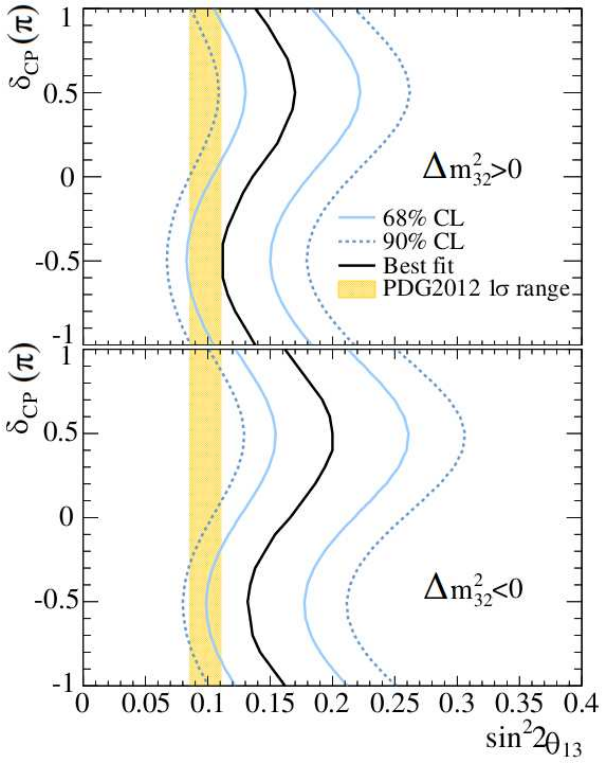

Figure 2.2.: Plot from [21] showing the T2K best-fit and confidence contours for $\sin^2 2\theta_{13}$ and δ with the $\sin^2 2\theta_{13}$ allowed range from [4]. Normal hierarchy (top) and inverted hierarchy (bottom).

PDG2012 [4]. When combined, these measurements have some sensitivity to δ. Figure 2.3 shows a log-likelihood plot for δ when the T2K data and the reactor constraints are taken together. Figure 2.4 shows the equivalent using the latest MINOS dataset. Sensitivty to δ is seen in both plots, with the best-fit around $\delta = -\pi/2$.

Outlook

There are many unanswered questions to be addressed by future experiments. Some areas of interest are as follows:

1. Are neutrinos Majorana or Dirac particles?
2. Is the neutrino mass hierarchy normal or inverted (i.e. is $\Delta m^2_{32} > 0$ or $\Delta m^2_{32} < 0$)?
3. What is the absolute neutrino mass scale?
4. Is $\theta_{23} = \pi/4$ (i.e. is there maximal mixing)?

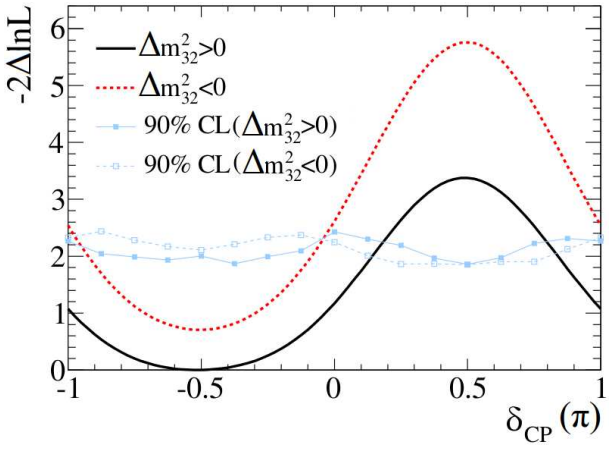

Figure 2.3.: Plot from [21] showing the log-likelihood over the range of δ when including both the T2K data in Reference [21] and the average $\sin^2 2\theta_{13}$ from Reference [4]. The blue lines show the 90% confidence level calculated using the Feldman-Cousins method.

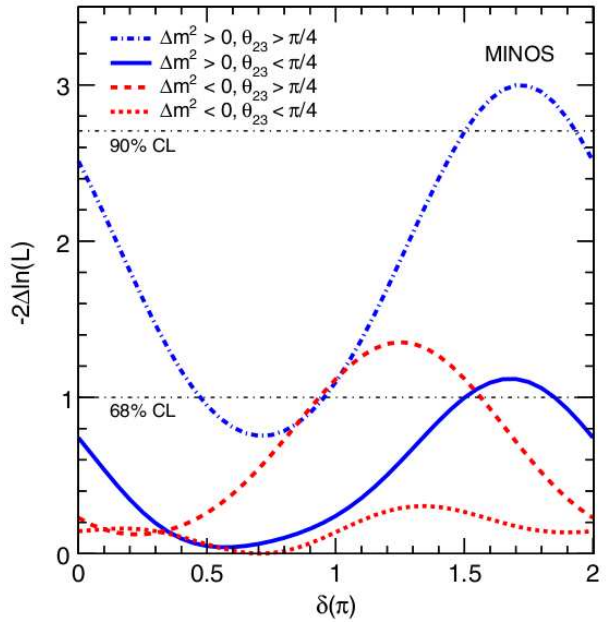

Figure 2.4.: Plot from [23] showing the log-likelihood over the range of δ when the data MINOS data in Reference [23] and the average $\sin^2 2\theta_{13}$ from the three main reactor experiments [28, 24, 26] are considered together.

5. What is the mechanism for neutrino mass generation?

6. Is lepton number conserved?

It is likely that many of the experimental questions may be answered by the current or next generation of neutrino oscillation experiments. However, a lesson from the history of science is that there are most probably many questions yet to be asked.

Chapter 3.

Neutrino cross section theory

An interaction model is a list of reasonable assumptions from which a prediction can be made of the value or distribution of some observable quantity. The collection of all models should permit a description of all observables relevant to a given measurement. The interaction models of interest to T2K describe (anti-)neutrino–nucleus interactions in the range $E_\nu = 0.01$–30 GeV. The nuclei of interest are those present in significant quantities in the T2K detectors, and the energy range is set by the spectrum of the T2K beam. We are also interested in the interactions of the products of the neutrino interactions within the nucleus, referred to as final-state interactions (FSI).

The neutrino interaction and FSI models used in T2K are contained in the NEUT Monte Carlo interaction generator [30] (another generator, GENIE [31], is also used for cross-checks against NEUT). In this chapter, the models employed by NEUT will be briefly described, and the models most relevant to this discussion will be explored in further detail.

3.1. The NEUT generator

NEUT simulates charged and neutral current processes for neutrinos of energies between 10 MeV and 100 TeV. Simulated processes include quasi-elastic scattering, nucleon resonance production, coherent interactions, and hadron and photon production. A number of nuclei are simulated, though the generator is most optimised for water targets. The neutrino interaction modes simulated by NEUT are defined and summarised in Table 3.1, and the cross sections of the main mode groups at neutrino energies around that of the T2K beam are shown in Figure 3.1.

Reaction	Name
$\nu + n \rightarrow \ell + n$	Quasi-elastic (CCQE)
$\nu + N \rightarrow \ell + N' + \pi^{+,-,0}$	Single pion from delta resonance
$\nu + A \rightarrow \ell + A + \pi^{+}$	Coherent pion production
$\nu + n \rightarrow \ell + p + \gamma$	Single gamma from delta resonance
$\nu + N \rightarrow \ell + N' +$ multi-π $(1.3 < W < 2.0$ GeV)	Multi-pion
$\nu + n \rightarrow \ell + p + \eta$	Single eta from delta resonance
$\nu + n \rightarrow \ell + \Lambda + K^{+}$	Single K from delta resonance
$\nu + N \rightarrow \ell + N' + X$ $(W > 2.0$ GeV)	Deep inelastic scattering

Table 3.1.: List of charged-current interaction modes simulated by NEUT. n = neutron, p = proton, N = nucleon, A = nucleus. All processes are simulated for neutrinos and anti-neutrinos. Equivalent neutral current processes are also simulated.

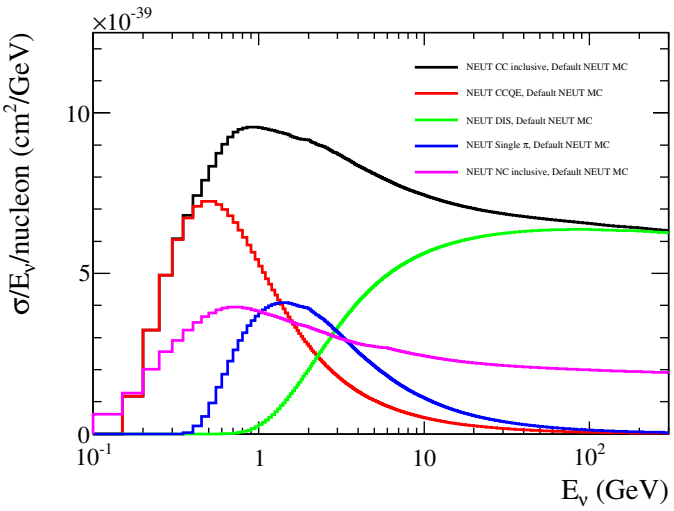

Figure 3.1.: Main NEUT interaction mode groups in the region 100 MeV to 100 GeV

The main signal mode in the far-detector is charged-current quasi-elastic (CCQE). In this mode, the neutrino energy can be reconstructed without significant bias from the final state charged lepton kinematics. The model of Llewellyn-Smith [32] is used to simulate CCQE assuming free nucleons. The Fermi-gas model of Smith and Moniz [33] is used to correct the nucleon-level cross section for nucleon motion. This model also includes the effect of the Pauli-exclusion principle on final-state nucleons (Pauli-blocking). Recently, there has been significant work to implement a more realistic nuclear model in NEUT, specifically the spectral function of Benhar *et al.* [34]. This would take into account nucleon correlations which are not considered by Smith-Moniz.

The Rein-Sehgal model is used for single pion production via intermediate resonances [35]. 18 resonances below $W = 2$ GeV (W is the invariant mass of the final hadronic system) are considered, with interference between the different resonances. Above $W = 2$ GeV there is a transition to a deep inelastic scattering (DIS) model for higher W. The Rein-Sehgal model is also used to simulate coherent interactions, though this mode is not very relevant to T2K measurements.

The cross section for DIS is calculated by integrating the GRV98 parton distribution function [36] with the correction proposed by Bodek and Yang [37]. High W events are handled by PYTHIA/JetSet, whereas low W are handled using bespoke code employing KNO scaling [38].

After NEUT has generated a nucleon-level event (i.e. an interaction between a neutrino and a nucleus), final-state particles are passed through the FSI subroutines. NEUT uses a cascade model in which the primary interaction position is chosen based on the nuclear density for a given nucleus, then particles are 'stepped through' the nuclear medium. At each step, an interaction probability for a number of possible FSI modes is calculated based on the nuclear density at that point, and the interaction mode (or lack thereof) is chosen by Monte Carlo. This continues until a particle interacts—at which point the interaction is simulated and further particles are produced—or exits the nucleus.

For pions, possible FSI modes are inelastic scattering, charge exchange, absorption and additional pion production. For lower momentum pions ($p < 500$ MeV), FSI probabilities were calculated by Oset and Salcedo [39]. For higher energy pions, FSI probabilities are determined from data. For final-state nucleons, the FSI modes are elastic scattering and single or double pion production. Nucleon FSI probabilities in NEUT are shown in Figure 3.2. These functions are taken from nucleon scattering experiments.

3.2. CCQE

The details of the CCQE interaction are important in the present discussion, since the work described in Chapter 5 concerns tuning of the CCQE model for input into the T2K oscillation analysis. It is therefore important to explore the models used to simulate this mode in NEUT.

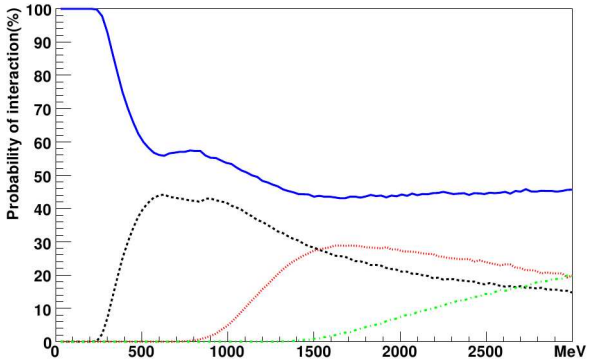

Figure 3.2.: Plot from [30]. Probability of nucleon FSI within oxygen nucleus. Blue (solid) curve is no interaction, black (dashed) curve is elastic scattering, red (dotted) curve is single pion production, green (dot-dashed) curve is double pion production.

3.2.1. Llewellyn-Smith

In his seminal review paper, Llewellyn-Smith summarised the quantum field theory formulation of weak interactions at accelerator energies as it stood upon publication in 1971 [32]. Much of the field has since progressed, however many fundamental aspects of the theory remain unchanged. In particular, his formulation of the charged-current quasi-elastic (CCQE) interaction mode is still used as the form of the basic interaction in neutrino interaction generators today, including in the NEUT generator.

The standard model description of weak interactions can be expressed in terms of a low-energy effective theory when the momentum transfer of the virtual weak boson is negligible compared to its mass. This is the case in neutrino interactions at accelerator energies. In the low-energy effective theory, the fundamental object describing weak interactions is the Lagrangian density:

$$\mathcal{L}_{\text{eff}} = \frac{G}{\sqrt{2}} J_\lambda^\dagger J_\lambda, \tag{3.1}$$

where G is Fermi's constant and J_λ is the weak current, expressed in terms of three components

$$J_\lambda = J_\lambda^{(\text{h})} + J_\lambda^{(\mu)} + J_\lambda^{(\text{e})} \tag{3.2}$$

where $J_\lambda^{(\mathrm{h})}$ is a current which encodes the possible transitions of the hadronic system, and $J_\lambda^{(\mathrm{e}),(\mu)}$ are the leptonic currents given by

$$j_\lambda^{(e),(\mu)} = \bar{\Psi}_{e,\mu}\gamma_\lambda(1-\gamma_5)\Psi_{\nu_e,\nu_\mu}. \tag{3.3}$$

The matrix elements of $\mathcal{L}_{\mathrm{eff}}$ give the transition elements for the weak interaction processes in the theory.

The model is based on a number of assumptions:

1. Lorentz invariance
2. CPT invariance
3. Lepton number conservation
4. Universality of electron and muon interactions
5. Absence of neutral currents
6. 2-component neutrino theory (i.e. only electrons and muons)

The final two assumptions are now known not to hold: neutral currents have since been measured, and there are three observed flavours of leptons, but both of these can be accommodated by modifications to Equations 3.2 and 3.3.

The CCQE process is the interaction of a neutrino with a neutron, with a charged lepton and proton in the final state:

$$\nu(k_1) + n(p_1) \rightarrow l^-(k_2) + p(p_2) \tag{3.4}$$

where k_1, k_2, p_1, p_2, are the 4-momenta of the initial and final state leptons, and initial and final state nucleons respectively. The hadronic current in the CCQE processes is written as

$$\left\langle p(p_2) \left| J_\lambda^\dagger \right| n(p_1) \right\rangle = \cos\theta_c \bar{u}(p_2)\Gamma_\lambda u(p_1) \tag{3.5}$$

where u and $\bar{u}$ are the spinors for the neutron and proton respectively, and Γ_λ is

$$\begin{aligned}\Gamma_\lambda =& \gamma_\lambda F_v^1(q^2) + \frac{i\sigma_{\lambda\nu}q^\nu\xi F_v^2(q^2)}{2M} + \frac{q_\lambda F_v^3(q^2)}{M} + \gamma_\lambda\gamma_5 F_A(q^2) + \\ & \frac{q_\lambda\gamma_5 F_p q^2}{M} + \frac{\gamma_5(p_1+p_2)_\lambda F_A^3(q^2)}{M}.\end{aligned} \tag{3.6}$$

In this equation, $q = p_1 - p_2$ is the momentum transfer from the leptonic to the hadronic system, $M = \frac{1}{2}(M_p + M_n)$ is the average nucleon mass, and $\xi = \mu_p - \mu_n$ is the difference in magnetic moments between proton and neutron. The various F are nucleon form factors: $F_{A,v,p}$ are the axial, vector and pseudoscalar form factors. The form-factors take into account the spatial distribution of weak charge in the nucleus. Some assumptions are made regarding the form of the hadronic current which lead to constraints:

1. T invariance $\Rightarrow$ All form factors are real
2. Charge symmetry $\Rightarrow F_v^{1,2}, F_A, F_p$ real, $F_{v,A}^3$ imaginary $\Rightarrow F_{v,A}^3 = 0$

The non-zero vector form-factors can be re-expressed in terms of the electric and magnetic Sachs form-factors, G_E^v and G_M^v as:

$$F_v^1(q^2) = \left(1 - \frac{q^2}{4M^2}\right)^{-1} \left[G_E^v(q^2) - \frac{q^2}{4M^2} G_M^v(q^2)\right], \tag{3.7}$$

$$\xi F_v^2(q^2) = \left(1 - \frac{q^2}{4M^2}\right)^{-1} \left[G_M^v(q^2) - G_E^v(q^2)\right]. \tag{3.8}$$

In the original formulation the Sachs form-factors are assumed to be dipoles, however a more modern and widely used form is the BBBA07 parameterisation [40] where the form-factors are parameterised using a high dimensional polynomial fit to data. The form of the axial form-factor, F_A, is often assumed to be a dipole:

$$F_A(q^2) = \frac{F_A(0)}{\left(1 - q^2/M_A^2\right)^2}, \tag{3.9}$$

where M_A is the axial-mass, and the value at $q^2 = 0$ is measured precisely in β-decay experiments. The dipole form comes from the assumption of an exponential distribution of weak axial charge in the nucleon. The value of the axial-mass is of some controversy, with different experiments measuring different values. A value of $M_{\mathrm{A}} = 1.21$ GeV^2 is used in NEUT.

The Llewellyn-Smith formulation gives the cross section for the interaction of neutrinos with free nucleons. The effects of the high nuclear density inside the nucleus are taken into account by Smith and Moniz in their Fermi-gas model.

3.2.2. Smith-Moniz

The Smith-Moniz model [33], takes into account nucleon momentum and binding energy in the cross-section calculation. The model neglects detailed nuclear structure such as many-body interactions or nucleon correlations. This approach allows an analytic expression of the cross section. Additionally, the Fermi-surface momentum (which defines the momentum distribution of the nucleons) and the binding energy can be extracted from data.

The authors first consider the general process of neutrino scattering shown in Figure 3.3. They express the differential cross section as:

$$d^2\sigma = \frac{G^2}{2}\frac{1}{(2\pi)^2}\frac{1}{k_1.p}\frac{dk_2}{2\epsilon_2}\eta_{\mu\nu}W^{\mu\nu} \tag{3.10}$$

where $k_{1,2}$ are the initial and final-state lepton momenta, p is the initial state nucleon momentum, ϵ_2 is the energy of the final-state lepton, and $\eta_{\mu\nu}$ and $W^{\mu\nu}$ are the leptonic and hadronic tensors. They state the hadronic tensor as:

$$W_{\mu\nu} = (2\pi)^3\Omega\bar{\sum_i}\sum_f \delta^{(4)}(p-p'-q)\left\langle p\right|J_\nu^{(-)}(0)\left|p'\right\rangle\left\langle p'\right|J_\mu^{(+)}(0)\left|p\right\rangle E \tag{3.11}$$

where $J_\mu^{\pm}$ is the isospin component of the nuclear weak current, Ω is the quantisation volume, E is the target energy, p and p' are the energies of the initial and final-state nucleons, $q = p - p'$, i and f denote initial and final-states. If all nucleons are considered as independent, the nuclear weak-currents are expressed as:

$$J_\mu^{(\pm)}(0) = \sum_{k,k',\lambda,\lambda'} a^\dagger_{k',\lambda'}\left\langle k'\lambda'\right|j_\mu^{(\pm)}(0)\left|k\lambda\right\rangle a_{k,\lambda} \tag{3.12}$$

where the sum is over all initial and final-state nucleon momenta and energies, $a_\dagger$ is the free-nucleon creation operator, and the elementary current $j_\mu^{+(-)}$ connects a neutron (proton) to a proton (neutron). Since the target state is a collection of independent nucleons, the hadronic tensor is expressed in terms of single-nucleon matrix elements:

$$(W_{\mu\nu})_{\text{lab}} = \int dk f(k,q,\omega)T_{\mu\nu}, \tag{3.13}$$

where $T_{\mu\nu}$ is the single nucleon matrix element, and

$$f(k,q,\omega) = \frac{m_T \Omega}{(2\pi)^3} \frac{\delta(\epsilon_k - \epsilon_{k-q} + \omega) n_i(k) \left(1 - n_f\left(|k-q|\right)\right)}{\epsilon_k \epsilon_{k-q}} \tag{3.14}$$

where m_T is the nucleon mass, $\epsilon_{k,k-q}$ are the lab-frame energies of the initial and final-state leptons, and $n_{i,f}$ are the momentum distributions of the initial and final-state nucleons. The $(1 - n_f\left(|k-q|\right))$ term is the Pauli-exclusion factor: for the Fermi-gas model, $n_i(k) = \theta\left(k_f - |k|\right)$ where θ is a step function, k_f is the momentum level of the Fermi-surface, which ensures the final-state nucleon momentum is outside the Fermi-sea.

k_f and ϵ_1 (the Fermi-surface momentum and nuclear binding energy respectively) can be fit to electron-scattering data for various elements [41]: k_f defines the width and ϵ_1 the position of the quasi-elastic peak, seen as the lower momentum peak in Figure 3.4.

Figure 3.4 shows the model prediction compared to data for electron scattering experiments, and Figure 3.5 shows the model prediction for neutrino scattering.

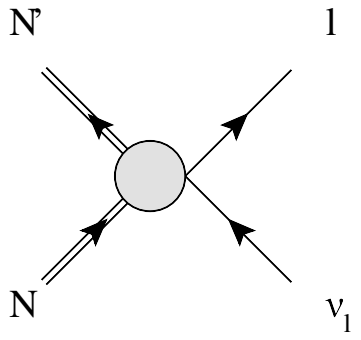

Figure 3.3.: General neutrino scattering diagram considered by Smith and Moniz. N and N' are the initial and final-state nucleons, ν_l and l are the initial and final-state leptons.

There are a number of limitations of this model. On the leptonic side, the model violates conservation of the vector current, though corrections due to this are small. On the hadronic side, short-range nucleon correlations are neglected, as are two-body effects: there is no description of multi-particle interactions which are though to populate the 'dip region' between the quasi-elastic and delta peaks. Data in the dip region is underestimated by the model predictions, as in Figure 3.4.

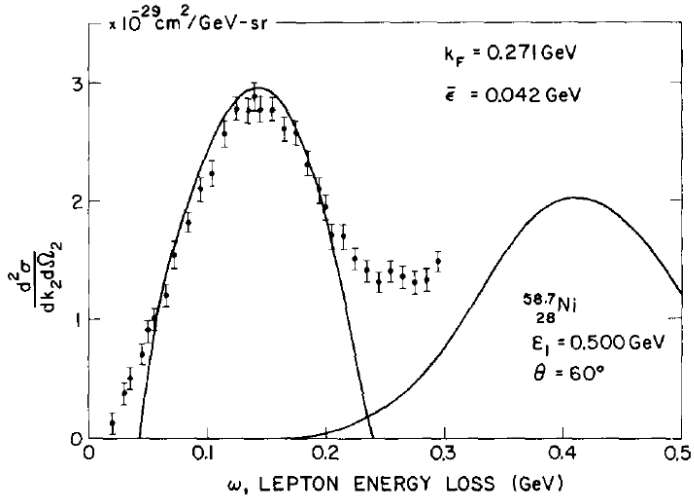

Figure 3.4.: Plot from [33]. Predictions for the quasi-elastic (left line) and delta resonance (right line) cross sections for electron scattering as a function of lepton energy loss from the Smith-Moniz Fermi-gas model compared with data from the Stanford Mark III Linear Accelerator [41]. The cross section is computed on Ni with an incident neutrino energy of 0.5 GeV with scattering angle 60°

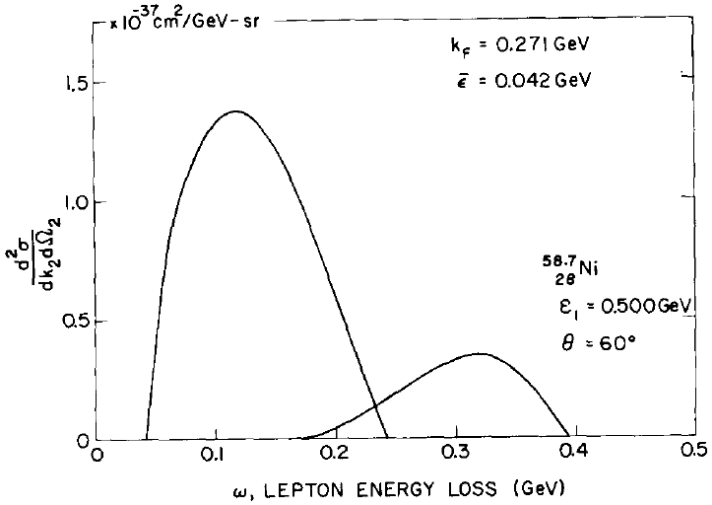

Figure 3.5.: Plot from [33]. Predictions for the quasi-elastic (left line) and delta resonance (right line) cross sections for neutrino scattering as a function of lepton energy loss from the Smith-Moniz Fermi-gas model. Cross section is computed on Ni with an incident neutrino energy of 0.5 GeV with scattering angle 60°

3.3. Multi-nucleon interactions

A multinucleon neutrino interaction is one in which the hadronic current contains two nucleons, so that two nucleons participate in the primary neutrino interaction. In the literature they are also referred to as 'twp particle, two hole' (2p2h) interactions, or meson exchange currents (MEC). This terminology is used particularly when discussing the calculation of cross sections for these interactions, since some formulations involve the excitation of a pair of particles and holes, which are connected by a meson propagator. The generalisation to n nucleons is called npnh.

The model of Nieves *et al.* [42] is of particular interest to experimentalists interested in modelling multinucleon neutrino interactions, as it predicts the total charged-current neutrino scattering cross-section in the few-GeVregion including quasi-elastic interactions, resonant and non-resonant pion production, and multinucleon neutrino interactions.

In this section, evidence for multinucleon neutrino interactions is surveyed, and an overview is given of the calculation of the multinucleon neutrino cross section in the Nieves model. Some alternative approaches to the multinucleon neutrino cross section calculation are described.

3.3.1. Evidence for a multi-nucleon interaction component of the neutrino and anti-neutrino charged-current cross section

Multinucleon neutrino interactions have not been observed experimentally, though there are hints from a number of observations that they may contribute to the total neutrino scattering cross section.

In 2010, the MiniBooNE collaboration released a measurement of the neutrino CCQE cross section [43]. When the M_{A} parameter is fit to this data using the NUANCE generator prediction, the best-fit value of the was found to be $M_{\mathrm{A}} = 1.35 \pm 0.17$ GeV. Subsequent analyses of the data found similar values [44]. This value is significantly higher than the world-average values from from neutrino scattering on deuterium ($M_{\mathrm{A}} = 1.026 \pm 0.0021$ GeV) [45] or from pion electro-production ($M_{\mathrm{A}} = 1.014 \pm 0.016$ GeV) [40]. Figure 3.6 shows the results of many experiments to establish these world-averages for the two channels. Further, the NOMAD experiment, which measured the CCQE cross section and extracted an axial mass from a higher-energy neutrino beam, found a best-fit

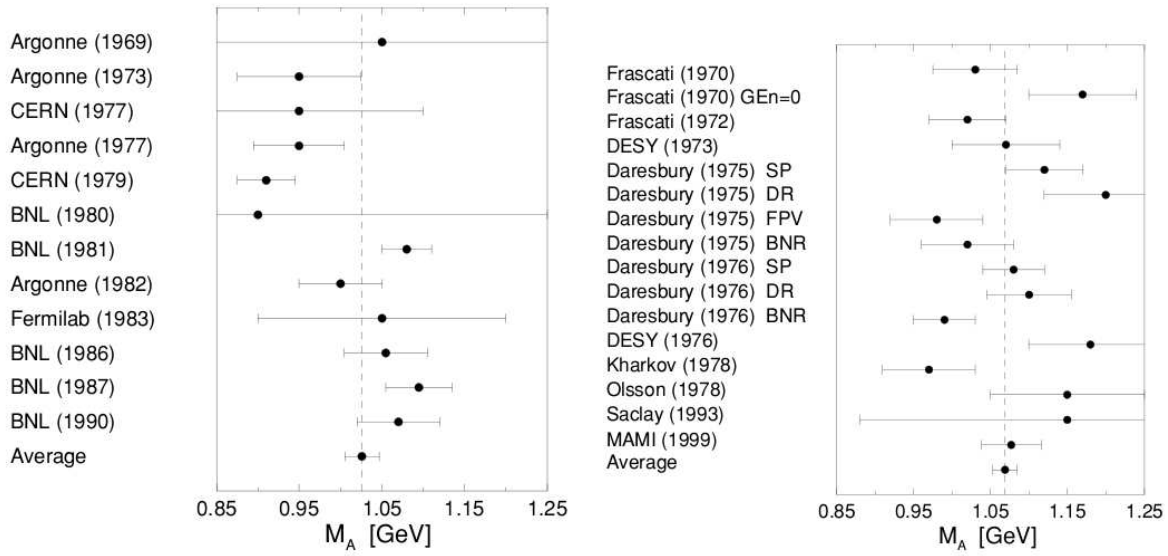

Figure 3.6.: Figure taken from [45] showing the values of axial mass fits using a number of datasets. Left panel: CCQE neutrino and anti-neutrino scattering experiments. The right panel: pion electroproduction experiments.

axial mass of $M_{\mathrm{A}} = 1.05 \pm 0.02(\mathrm{stat}) \pm 0.06(\mathrm{syst})$ GeV [46], consistent with the world average values.

The difference between the MiniBooNE and the other best-fit values may be due to the presence of multinucleon neutrino interactions in the signal, which were not corrected for as they are not included in the NUANCE generator prediction (the generator used for MiniBooNE analysis). Recent theoretical work has indicated that it is possible to describe the MiniBooNE data with a value of the axial mass close to the world-average, by including multinucleon neutrino interactions into the model (and including a number of other nuclear effects). Figure 3.7 (taken from [47]) shows the MiniBooNE data compared to a number of CCQE models from different generators and predictions. Predictions which use a value of M_{A} of around one generally underestimate the data. The two predictions which best represent the data are the NUANCE prediction with a high axial mass, and the Martini model which contains a multinucleon neutrino interaction mode.

Another hint of the existence of multinucleon neutrino interactions appears in measurements from the MINERνA collaboration. They report an excess(deficit) of energy deposited around the vertex in a selection of CCQE-like interactions with (anti)neutrinos [49, 50], consistent with an excess(deficit) of protons in the final state. This is qualitatively consistent with the multinucleon neutrino models of Nieves, which predicts higher $pp(nn)$ final-states in (anti)neutrino interactions. Further, the differential

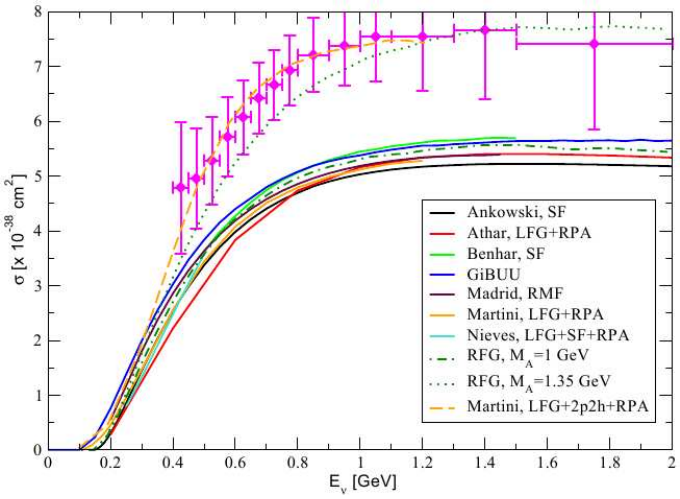

Figure 3.7.: Comparison of the MiniBooNE CCQE-corrected data with a number of CCQE models. X-axis shows reconstructed neutrino energy from muon kinematics assuming a true CCQE interaction. Plot from [48] with model predictions from [47].

cross sections are well described by the transverse enhancement model [51], which is a modification of form-factors which mimics the affect of multinucleon neutrino interactions.

3.3.2. Multinucleon model of Nieves et al.

Nieves *et al.* use a many-body approach to calculate the total lepton scattering cross section in the few-GeVregion. The method has been applied to electrons [52] and neutrinos [53, 42].

Many-body approach to cross section predictions

The basic method is best described in [52] for the case of electron scattering. The procedure is largely the same for neutrino scattering, with the photon exchanged for the W-boson.

For electrons, the object of interest is the self-energy of a photon in nuclear matter. The optical theorem then relates the self-energy to the forward-scattering cross section. A diagrammatic representation of the self-energy is shown in Figure 3.8.

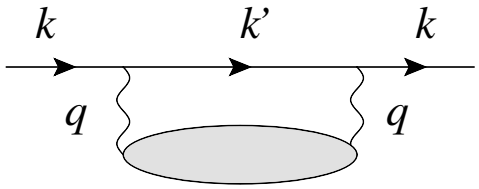

Figure 3.8.: Diagram of the photon self-energy (from [52]). k (k') is the electron momentum before (after) emission of the photon, q is the virtual photon momentum. The gray oval represents all processes in the photon self-energy.

The self-energy can be expressed as:

$$\Sigma(k) = \frac{ie}{2m_e} \int \frac{d^4q}{(2\pi)^4} \frac{L_{\mu\nu}\Pi_\gamma^{\mu\nu}(q)}{q^4} \frac{1}{k^2 + m_e^2 + i\epsilon} \tag{3.15}$$

where e is the electron charge, m_e is the electron mass, q is the momentum of the virtual photon, $L_{\mu\nu}$ is the leptonic tensor, $\Pi_\gamma^{\mu\nu}$ is the virtual photon self-energy tensor, and k is the momentum of the electron. The optical theorem relates this to the total cross-section, which is obtained using the Cutkosky rules [54]. Cutting the electron line after the emission of the photon and expanding the photon self-energy diagrams, this is expressed as:

$$\mathrm{Im}\,\Sigma(k) = \frac{2\pi\alpha}{m_e} \int \frac{d^3q}{(2\pi)^3} \left(\mathrm{Im}\,\Pi_\gamma^{\mu\nu} L_{\mu\nu}(k,k')\right) \frac{1}{q^4} \frac{1}{2E_e(k')} \Theta(q^0) \tag{3.16}$$

where α is the fine-structure constant, E_e is the electron energy, Θ is the heavyside function, and q^0 is the energy of the virtual photon. This is related to the total cross section as:

$$d\sigma = -\frac{2m}{|\mathbf{k}|}\,\mathrm{Im}\,\Sigma d^3r \tag{3.17}$$

where dr is an element of distance inside the nuclear target. We then have an expression for the differential cross section in terms of the photon self-energy as:

$$\frac{d^2\sigma}{d\Omega_e' dE_e'} = -\frac{\alpha}{q^4} \frac{|\mathbf{k}|}{|\mathbf{k'}|} \frac{1}{(2\pi)^2} \int d^3r\,\mathrm{Im}\,\Pi_\gamma^{\mu\nu} L_{\mu\nu} \tag{3.18}$$

where $d\Omega_e'$ is an element of solid angle in which the final-state electron is scattered, and E_e' is the energy of the final-state electron. The general form of this differential cross

section is:

$$\frac{d^2\sigma}{d\Omega'_e dE'_e} = \frac{\alpha}{q^4}\frac{|\mathbf{k}|}{|\mathbf{k'}|}L_{\mu\nu}W^{\mu\nu} \tag{3.19}$$

where $W^{\mu\nu}$ is the hadronic tensor. This allows us to relate the photon self-energy to the hadronic tensor.

Application to neutrino scattering

We are now concerned with computation of the neutrino charged-current inclusive cross section, as described in References [53, 42] The general form of the of the cross section is written:

$$\frac{d^2\sigma}{d\Omega dE} = \frac{|\mathbf{k}|}{|\mathbf{k'}|}\frac{G^2}{4\pi^2}L_{\mu\nu}W^{\mu\nu} \tag{3.20}$$

where k and k' are the initial and final lepton momenta, G is the Fermi constant, and L and W are the leptonic and hadronic tensors. The hadronic tensor corresponds to the charged electroweak transitions of the nucleus:

$$W^{\mu\sigma} = \frac{1}{2M}\bar{\sum_f}(2\pi)^3\delta^4\left(P'_f - P - q\right)\langle f \,|\, j^\mu(0) \,|\, i\rangle \langle f \,|\, j^\sigma(0) \,|\, i\rangle^* \tag{3.21}$$

where M is the mass of the nucleus, P is the 4-momentum of the nucleus, P'_f is the 4-momentum of the final hadronic state, $q = k - k'$ is the 4-momentum transfer to the nucleus, $\bar{\Sigma}$ is the sum and average over initial spins, and j^μ is the hadronic charged current, given by

$$j_\mu = \bar{\Psi}_u\gamma_\mu\left(1 - \gamma^5\right)\left(\cos\theta_c\Psi_d + \sin\theta_c\Psi_s\right) \tag{3.22}$$

where $\Psi_{u,d,s}$ are the quark fields and θ_c is the Cabbibo angle. In a similar way to Equation 3.18, the neutrino charged-current differential cross section is expressed in terms of the W-boson self-energy:

$$\frac{d^2\sigma}{d\Omega dk} = -\frac{|\mathbf{k'}|}{|\mathbf{k}|}\frac{G^2}{4\pi^2}\left(\frac{2\sqrt{2}}{g}\right)^2\int\frac{d^3r}{2\pi}\left\{L^s_{\mu\eta}\,\mathrm{Im}\left[\Pi^{\mu\eta}_w + \Pi^{\eta\nu}_w\right] - L^a_{\mu\eta}\,\mathrm{Re}\left[\Pi^{\nu\eta}_2 - \Pi^{\eta\mu}_w\right]\right\}\Theta(q_0) \tag{3.23}$$

where k and k' are the momenta of the neutrino and final-state charged lepton, g is the weak coupling constant, $L^{s(a)}$ is the symmetric (antisymmetric) part of the leptonic tensor, and $\Pi_w^{\mu\eta}$ is the W-boson self-energy.

To obtain the cross section in Equation 3.23, Nieves *et al.* use a many-body expansion of Π_w [42], including first, second and some third order diagrams. Some of the processes taken into account are shown in Figure 3.9. The diagrams of Figure 3.9 contain placeholders for the possible vertices, for example there are seven possible $WN\pi N'$ vertices as shown in Figure 3.10. When calculating the contribution from the diagrams in Figure 3.9 the contribution from all combinations of possible vertices must be considered.

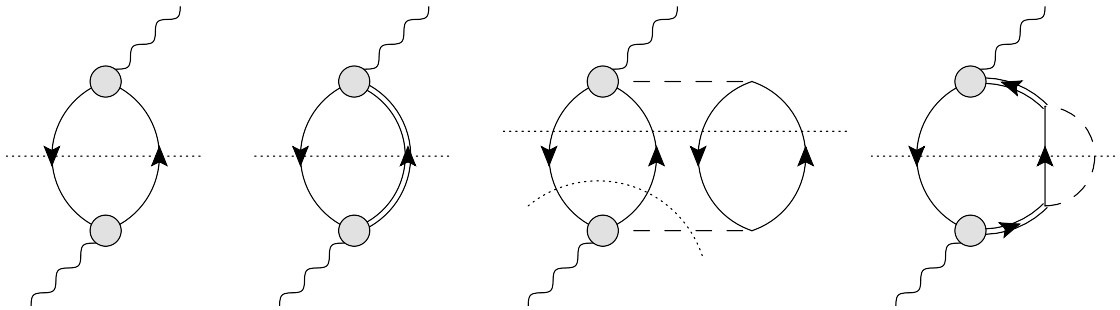

(a) Quasi-elastic **(b)** Δ resonance **(c)** 2p2h or π production **(d)** 1p1h1π

Figure 3.9.: Some W-boson self-energy diagrams. Solid lines represent particles or holes, double lines represent nucleon resonances (Δ), dashes lines represent mesons, wavy lines represent the incoming or outgoing W. The dotted line represents the Cutkosky cut. Gray circles represent any possible vertex.

Contribution of multinucleon excitation

The multinucleon neutrino process is the one in which the W excites a pair of particle-hole (ph) loops, as in Figure 3.9c. This is actually 49 different diagrams from all combinations of vertices shown in Figure 3.10.

The first step to calculating the 2p2h term is to calculate a similar diagram: that of single pion production shown in Figure 3.11. This diagram also contains two $WN\pi N'$ vertices so also contains contributions from the 49 combinations of vertices in figure 3.10. The self-energy term for this contribution is:

$$\begin{aligned} i\Pi^{\mu\nu}_{w;1p1h1\pi}(q) = &- i\left(\frac{g}{2\sqrt{2}}\right)^2 \sum_{N,N',\lambda} \int \frac{d^4q}{(2\pi)^4} \int \frac{d^4p}{(2\pi)^4} G(p;\rho_N) G(p';\rho_{N'}) D_\pi(k_\pi) \\ &\times \mathrm{Tr}\left[(\not{p}+M)\gamma^0 j_A^{\mu\dagger}\gamma^0(\not{p}'+M) j_A^\nu\right] \end{aligned} \tag{3.24}$$

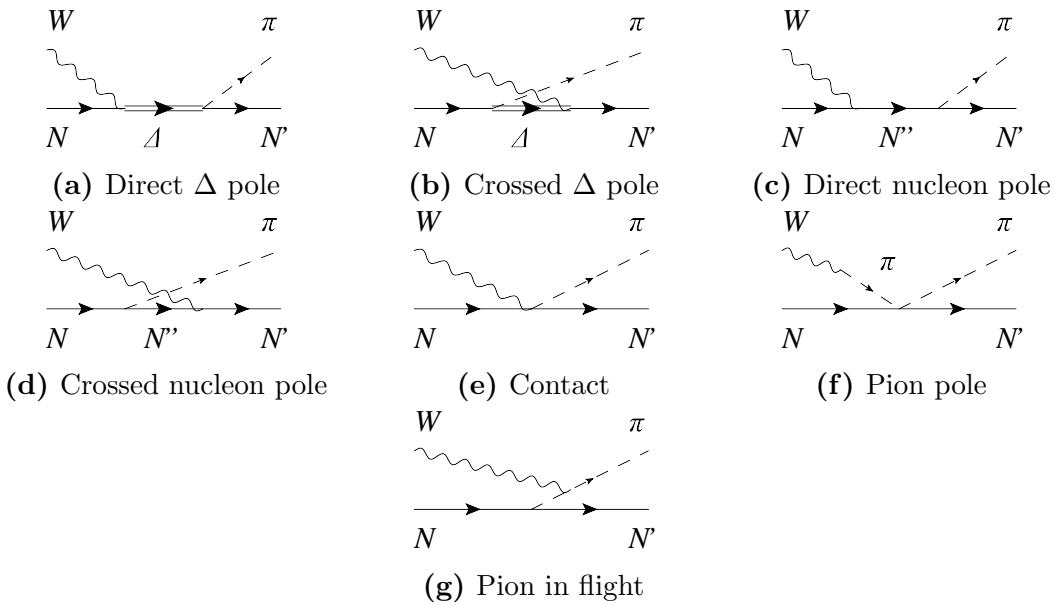

(a) Direct Δ pole **(b)** Crossed Δ pole **(c)** Direct nucleon pole

(d) Crossed nucleon pole **(e)** Contact **(f)** Pion pole

(g) Pion in flight

Figure 3.10.: Possible $WN\pi N'$ vertices.

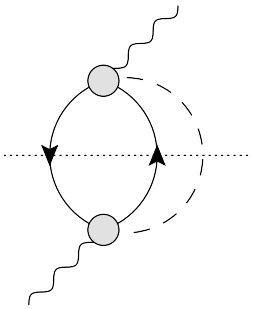

Figure 3.11.: Single pion production term

where the sum runs over all initial and final nucleons (N,N') and pion charges (λ), q, p, k_π are the W, nucleon and pion momenta, $p' = p + q - k_\pi$, D_π is the pion propagator, $G(p;\rho)$ is the nucleon propagator multiplied by a Pauli-blocking factor, and j_A^μ is the amputated amplitude for the process $WN \to N'\pi^\lambda$ obtained by summing the contributions from all vertices in Figure 3.10. By evaluating at the average nuclear density, this can be simplified to

$$-i\Pi^{\mu\nu}_{w;1p1h1\pi}(q) = \left(\frac{g}{2\sqrt{(2)}}\right)^2 \frac{1}{4M^2} \sum_{N,N',\lambda} \int \frac{d^4k_\pi}{(2\pi)^4} D_\pi(k_\pi) \bar{U}_R(q-k_\pi, k_F^N, k_F^{N'}) A^{\mu\nu} \quad (3.25)$$

where

$$A_{\mu\nu} = \frac{1}{2}\mathrm{Tr}\left[(\langle p\rangle + M)\gamma^0 \langle j_A^{\mu\dagger}\rangle \gamma^0 (\langle \not{p}\rangle + \not{q} - \not{k}_\pi + M) \langle j_A^\nu\rangle\right] \quad (3.26)$$

is related to the contributions from all possible vertices evaluated at the mean nuclear density, and $\bar{U}_R(q-k_\pi, k_F^N, k_F^{N'})$ is a Lindhard function which appears from the integral over the nucleon momentum. Applying the Cutkosky rules the final expression for the hadronic tensor for the $1p1h1\pi$ contribution is:

$$W^{\mu\nu}_{W;1p1h1\pi} = -\Theta(q^0)\frac{1}{2M^2}\int \frac{d^3r}{2\pi} \sum_{N,N',\lambda} \int \frac{d^3k_\pi}{(2\pi)^3} \frac{\Theta(q^0 - k_\pi^0)}{2w(k_\pi)} \,\mathrm{Im}\,\bar{U}_R A^{\mu\nu} \quad (3.27)$$

where $w(k_\pi)$ is the pion on-shell energy and q^0 is the energy component of q (the four-momentum of the W, which is the energy transferred from the leptonic to the hadronic systems).

From this, the contribution of the 2p2h diagram in Figure 3.9c can be obtained by adding the affect of an additional on-shell ph loop, and by substituting the single on-shell pion propagator for two off-shell terms:

$$D_\pi(k_\pi) \to D_\pi^2(k_\pi) F_\pi^2 \frac{f^2_{\pi NN}}{m_\pi^2} \mathbf{k}_\pi^2 U_\lambda(k_\pi), \quad (3.28)$$

where F_π is the pion form-factor and $f_{\pi NN}$ is a vertex coupling constant. This yields an expression for the 2p2h contribution to the hadronic tensor as

$$\begin{aligned} W^{\mu\nu}_{2p2h}(q) =& \Theta(q^0)\frac{1}{M^2}\int\frac{d^3r}{2\pi}\sum_{N,N',\lambda}\int\frac{d^4k_\pi}{(2\pi)^4}\Theta(q^0-k^0_\pi)F^2_\pi(k_\pi)\,\mathrm{Im}\,\bar{U}_R A_{\mu\nu} \\ &\times D^2_\pi F^2_\pi(k_\pi)\frac{f^2_{\pi NN}}{m^2_\pi}\mathbf{k}^2_\pi\Theta(k^0_\pi)\,\mathrm{Im}\,U_\lambda(k_\pi) \end{aligned} \tag{3.29}$$

In practice, this expression is modified slightly since some of the vertex combinations are included in other parts of the calculation, so double-counting must be avoided.

The equivalent expression for antineutrinos is obtained by changing the sign of the anti-symmetric part of the lepton tensor and using the equivalent $W^- N \to N'\pi^\lambda$ amplitudes at the vertices.

Figure 3.12 shows the predictions of the three main components of Nieves' model—QE, pion production and multinucleon neutrino interactions—as a function of energy transfer. The multinucleon contribution is non-negligible, and is relatively insensitive to momentum transfer. The multinucleon fraction is largest between the QE and Δ peaks, and increases at larger scattering angles.

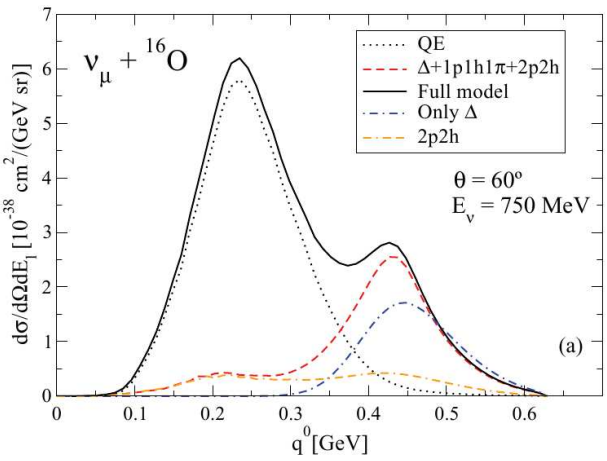

Figure 3.12.: Muon neutrino differential cross sections on oxygen of the three major components of Nieves' inclusive model, presented as a function of energy transfer from the neutrino to the hadronic system (q^0). Plot taken from [42].

An important final detail of the multinucleon neutrino interaction model in Nieves' model is that it includes events in which a pion is produced from the decay of a delta resonance, which is then absorbed by another nucleus. These types of events, referred

to as pionless delta decay events, are already included in the NEUT simulation, so care must be taken to avoid double-counting these events.

Extension to high energy

Nieves *et al.* state that their model is valid up to E_ν = 1–1.5 GeV. The reason is that at higher neutrino energies, additional unsimulated processes and resonances would contribute to the cross-section. The T2K beam contains significant flux above 1 GeV, so it is important to simulate events above the authors' proposed energy cut-off.

Recent work has been done to extend the validity of the model to higher neutrino energy. The authors of [55] found that the model is limited in three-momentum transfer to the hadronic system rather than neutrino energy, and state that the limit should be a maximum three-momentum transfer of 1.2 GeV. The threshold value comes from the approximate momentum transfer at which contributions from unsimulated diagrams would become non-negligible. The limit on the neutrino energy can therefore be lifted if a limit on the three-momentum is imposed.

Alternative multinucleon models

The prediction of Nieves *et al.* [42] was chosen as the model to be implemented into NEUT, however there are a number of independent calculations which predict the cross section of equivalent or similar interaction modes.

The model of Martini *et al.* [56] uses a similar many-body expansion as [42], and is limited to a similar range of momentum transfers. There are some diagrams present in Nieves' model which are omitted in Martini's, and there are some approximations and calculations which are treated differently between the models. These differences result in predictions which differ by up to a factor of two in some parts of the cross section.

A different approach was taken by Bodek *et al.* in the transverse enhancement model [51]. This model parameterises an observed enhancement in the transverse cross section in electron scattering experiments in terms of a modification to the magnetic form-factor as

$$G_{M_{p,n}}(Q^2) \rightarrow G_{M_{p,n}}(Q^2) \times \sqrt{1 + AQ^2 e^{-Q^2/B}} \tag{3.30}$$

where A and B are free parameters fit to data. The interpretation of the model is that the enhancement is caused by unmodelled components of the total cross section, often thought to be multinucleon neutrino interactions. This approach does not model the kinematics of multinucleon neutrino interactions which are important in T2K analyses.

Chapter 4.

The T2K experiment

The T2K (Tokai to Kamioka) experiment uses neutrinos from an accelerator source to measure neutrino oscillation parameters and neutrino interaction cross sections. The measurements are performed by producing a beam of (primarily) muon neutrinos and characterising the difference in the flux of neutrinos between the near and the far detectors. At leading order, the change in the ν_μ flux allows measurement of θ_{23} and Δm^2_{23}, and the change in the ν_e flux allows measurement of θ_{13} and to some extent δ.

The main goals of T2K are:

- measurement of $\sin^2 2\theta_{13}$ with a precision of 0.002
- measurement of Δm^2_{23} with a precision of 10^{-4} eV^2
- measurement of $\sin^2 2\theta_{23}$ with a precision of 0.01
- measurement of neutrino cross sections of use to present and future neutrino experiments

The T2K neutrino beam is produced at the Japan Proton Accelerator Research Complex (J-PARC) in Tokai-Mura, Ibaraki, Japan. A proton synchrotron in J-PARC is used to accelerate a beam of protons to 30 GeV. The protons are incident on a carbon target which produces a flux of particles, most of which are pions, and some of which are kaons and other particles. The charged particles are focussed and sign-selected using a series of three magnetic horns. The positive (negative) pions decay into muons (antimuons) and anti-muon neutrinos (muon neutrinos), which is the main source of the T2K beam. The near detector suite is located approximately 280 m from the beam source and contains one on- and one off-axis detector. The on-axis detector measures beam stability and interaction rates. The off-axis detector characterises the beam before

oscillation probabilities become appreciable. The off-axis detector also performs cross section measurements. The far-detector is located 295 km from the beam source at the same angle to the beam as the off-axis near-detector. The far-detector characterises the energy and flavour profile of the neutrino beam after the effects of the neutrino oscillations have become appreciable.

T2K uses the off-axis beam technique [57]: the neutrino beam is directed such that the far-detector and off-axis near-detector are away from the beam axis by 2.5°. This reduces the high-energy neutrino flux, lowers the energy of the flux peak, and reduces the width of the flux peak. The off-axis angle is tuned to optimise sensitivity to the oscillation parameters of interest, and to minimise the effect of background interactions from non-oscillated parts of the neutrino flux (e.g. from non-elastic events in the harder part of the spectrum). As the peak narrows, the flux also decreases, so the gains from increasing the off-axis angle are limited by the need for a high flux.

Each component of the T2K detectors are now discussed. Much of the information is taken from the reference [58] and further details should be sought there. The near-detector data collection and Monte Carlo simulation is described, and a discussion of the use of near-detector data in the oscillation analysis is given subsequently.

4.1. Neutrino beam

In this section, the general procedure of the production of the neutrino beam is described, with some attention paid to the ways in which the beam is characterised as it is produced.

4.1.1. Proton acceleration

The source of the T2K neutrino beam is the decay of the products of the interaction of a 30 GeV proton with a carbon target. The first stage in the production of the neutrino beam is therefore the production of the proton beam.

A linear accelerator is used to accelerate H^-, and is designed to provide the H^- with 400 MeV of kinetic energy after accelleration. The H^- are passed through charge-stripping foils to ionise them to H^+, and they are injected into a rapid-cycling proton synchrotron in which they are accelerated to 3 GeV. 5% of these are injected into the J-PARC main ring which accelerates them to 30 GeV in a structure of eight bunches

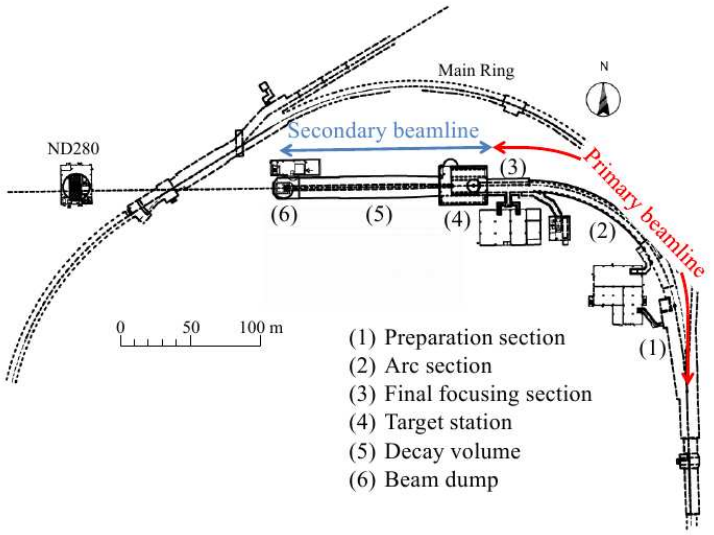

Figure 4.1.: Schematic diagram of the neutrino beamline.

(the other 95% are used for other experiments). The neutrino beamline is separated into a primary and a secondary part: the division is the point at which the protons hit the target. A schematic of the neutrino beamline is shown in Figure 4.1

4.1.2. Primary neutrino beamline

The main purpose of the primary beamline is to steer the protons from the main ring towards the fixed target, and focus them for acceptance into the target area.

Throughout the primary beamline, the beam is monitored for intensity, spatial profile, position and loss. Five current transformers measure beam intensity and timing at different points. These consist of toroidal wire coils which use induction to measure the beam charge. They are calibrated to an energy scale of 2%, with 10 ns timing resolution. The beam position and stability is measured with 21 electrostatic monitors. These are sets of four electrodes placed around the beamline which measure the top-bottom and left-right position by the asymmetry of the induced current. They have a precision of 450 μm. Beam loss is measured by 50 wire proportional counters filled with Argon and CO_2. These are sensitive up to 16 mW of beam loss. The final monitoring system is a series of 19 segmented secondary emission monitors. These are sets of horizontally and vertically aligned metal strips placed either side of an anode foil. Electrons are produced as the beam passes through the foil. The electrons induce a current in the strips and

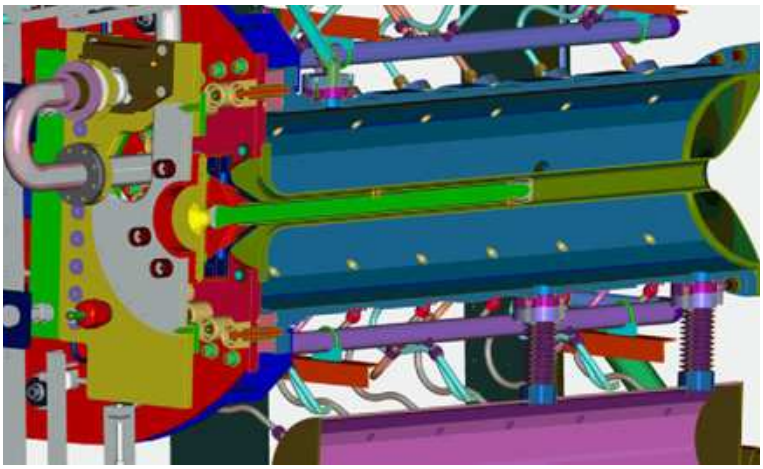

Figure 4.2.: Schematic diagram of the graphite target and the first horn.

allow the beam profile to be measured. This results in some loss of the beam so is not used during normal running.

4.1.3. Secondary neutrino beamline

The secondary beamline focuses the secondary particles from the interaction of the proton beam with the target. The decay products of these secondary particles become the neutrino beam. The secondary beamline must dissipate the large amount of energy that the proton beam and decay products deposit in the target area.

The target station consists of the target, an optical transition monitor, and three focussing horns, all contained inside a vessel which is filled with helium. The helium reduces absorption of secondary pions, and reduces the tritium and NO_x produced by the beam. Before collision with the target, the beam passes through the optical transition monitor. Protons passing though the material produce photons which allow the final beam profile to be imaged. The beam then impacts on the target. The target is a graphite rod, 91.4 cm in length and 2.6 cm in diameter. The material was chosen to have good thermal conductivity properties, but still requires significant cooling. This is done via gaseous helium, which must be passed over the target at approximately 250 m/s. Three electromagnetic horns are used to focus the charged particles from the interactions of the beam with the target. The target is inside the first horn, with the second and third located downstream. A schematic diagram of the target and the first horn is shown in Figure 4.2. The horns increase the flux of neutrinos at the far detector by a factor of 16. The horn polarities can be switched to produce a predominantly ν_μ or $\overline{\nu}_\mu$ beam.

The secondary particles, mostly charged pions, enter into a decay tunnel where they decay to muons and neutrinos which make up the majority of the T2K beam. The tunnel is 96 m long and is surrounded by 6 m of concrete shielding. The concrete is water-cooled so that its temperature remains below 100°C. At the end of the decay tunnel is the beam dump which allows the neutrinos to pass through but absorbs most other particles. The beam dump is a 75 t block of graphite which is water-cooled to a temperature below 150°C. Muons with energies greater than 5 GeV pass through the beam-dump into the muon monitor which monitors the beam center and stability.

4.2. Near detector suite

The near detector suite is located 280 m from the target station. The purposes of the near detectors are threefold:

1. measurement of the neutrino energy spectrum before oscillation
2. measurement of the flavour contents of the beam before oscillation
3. measurement of neutrino interaction cross sections.

The near-detector suite contains an on-axis and an off-axis detector. The on-axis detector monitors the neutrino beam stability, and the off-axis detector characterises the unoscillated beam and measures interaction cross sections.

4.2.1. Interactive neutrino grid

The on-axis detector is the Interactive Neutrino Grid (INGRID). INGRID monitors the beam direction and intensity by measuring inelastic interactions of the beam neutrinos with iron. A daily measurement of these beam parameters is provided. The beam center is measured to a precision of less than 10 cm, corresponding to an angular precision of 0.4 mrad.

INGRID is comprised of two sets of 14 identical modules, the arrangement of which is shown in Figure 4.3 (two modules overlap in the central position). An additional module, the proton module, is situated between the two central modules. The proton module measures protons in order to identify quasi-elastic neutrino interactions, which are of particular importance for T2K.

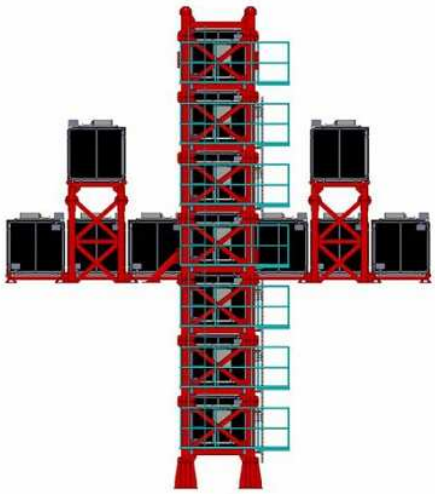

Figure 4.3.: Module arrangement in the INGRID detector with supporting framework.

Each INGRID module is made of nine iron planes sandwiched between 11 planes of scintillator bars, all surrounded by scintillator planes. Each iron plane is $124 \times 124 \times 6.5$ cm. The scintillator layers are made of 24 horizontal and 24 vertical bars of dimension $1.0 \times 1.5 \times 120.3$ cm.

4.2.2. Off-axis near detector

The off-axis near detector, ND280, characterises the beam at the same off-axis angle as the far-detector. The specific aims of ND280 are:

- characterisation of the signal ν_μ flux,
- characterisation of the background ν_e flux,
- measurement of the cross sections of neutrino interaction processes, especially those of the important backgrounds in the far-detector. To this end the detector must be capable of measuring
  - charged-current quasi-elastic interactions induced by both ν_μ and ν_e
  - charged-current interactions involving a Δ-resonance
  - neutral current interactions, especially those with a neutral pion in the final state.

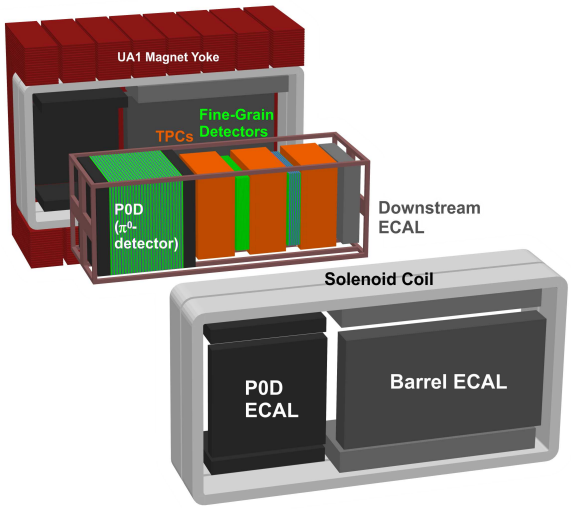

Figure 4.4.: Exploded-view schematic diagram of the ND280 detector.

An exploded-view schematic diagram of ND280 is shown in Figure 4.4. The detector is comprised of a number of sub-detectors, all inside a solenoid magnet. The air-cavities in the magnet are instrumented with scintillator bars, which are collectively known as the Side Muon Range Detector (SMRD). Inside the magnet is the Electromagnetic Calorimeter (ECal). This surrounds the inner detectors on all but the upstream face. Inside the the ECal, from upstream to downstream, are the pizero detector (PØD), three time projection chambers (TPCs) and two Fine-Grained Detectors (FGDs).

Magnet

The near-detector solenoid magnet was previously used for the UA1 and NOMAD experiments. It provides a mean magnetic field of 0.2 T over an internal volume of $7.0 \times 3.5 \times 3.6$ m. The magnetic field is known to an accuracy of 2 G. The coil itself is made from aluminium bars with a cross section of 5.45×5.45 cm. The return yoke is made from low-carbon steel plates. The coil is oriented with the central axis in the horizontal plane and perpendicular to the beam direction. This provides momentum in the vertical direction to charged particles travelling along its axis.

Pi-zero Detector

The most upstream sub-detector in ND280 is the pizero detector [59] (PØD, pronounced 'pod'). The main purpose of the PØD is to measure the inclusive neutral current pizero

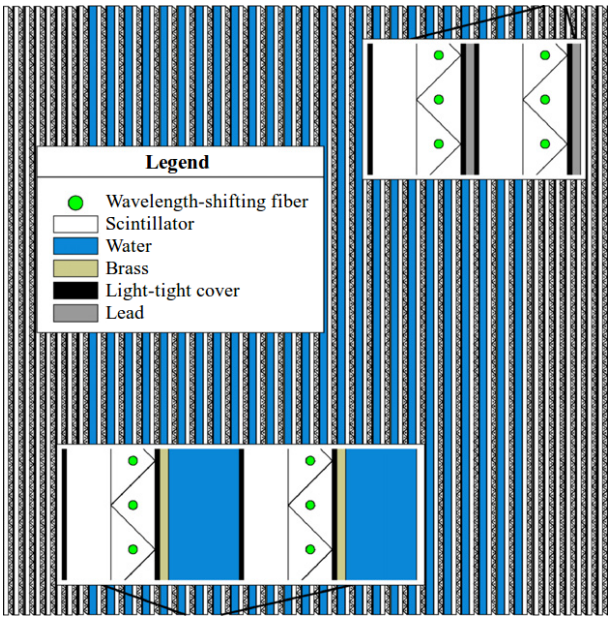

Figure 4.5.: Schematic diagram of the PØD.

cross section on water ($\nu_\mu + N \rightarrow \nu_\mu + N + \pi^0 + X$). This is an important background to the ν_e appearance measurement: pizeros decay to two photons which are identical to electrons in the far detector, and it is possible that one of the rings is missed in the reconstruction of the event.

A diagram of the PØD is shown in Figure 4.5. It is separated into modules, each comprised of 132 vertical and 126 horizontal polystyrene bars sandwiched between target material. The modules are grouped into two main sections: 14 ECal sections (not related to the ND280 ECal) and 25 water target sections. In the ECal sections the modules are layered with sheets of lead, 4 mm in thickness. In the water target sections, scintillator is layered with bags of water and sheets of brass 1.5 mm in thickness. The total mass of water in the PØD was measured to be 1902 ± 16 kg.

The scintillator bars enable reconstruction of electromagnetic showers from interactions with a pizero in the final state, as well as from electrons and other interactions with a γ in the final state. The water targets enable cross section measurements on the same target material as comprises the far detector.

Time Projection Chambers

Downstream from the PØD are three Time Projection Chambers (TPCs) [60], arranged alternately with the two Fine Grained Detectors. The TPCs determine the number and orientation of particles which traverse their volume, and can identify particles by measurements of curvature and dE/dx.

The principle of TPC technology is that charged particles travelling through a gas ionise the gas atoms, and the electrons and ions are then accelerated by an applied electric field and measured at a segmented anode. Both timing and spatial distribution of ions is measured, allowing 3D reconstruction of tracks.

The ND280 TPCs are comprised of a gaseous mix inside a copper box. The copper box is in turn contained inside an aluminium box, with carbon dioxide between them as an insulating material. The gas in the inner box is Ar:CF_4:C_4H_{10} in a 95:3:2 mixture. This mixture was chosen for its high drift speed and low diffusion rate.

The energy resolution of the TPCs is approximately 7.8% for minimally ionising particles, better than the design requirement of 10%. The spatial resolution of tracks is approximately 0.7 mm. The two sources of measurement for the PID, curvature and dE/dx, allow good separation between particles, with simulation indicating less than 1% mis-identification of electrons and minimally ionising particles.

Fine Grained Detectors

Situated between the three TPCs are two Fine Grained Detectors (FGDs) [61]. These provide most of the target mass for the TPCs, and also provide particle tracking. They each have 30 layers of polystyrene scintillator bars, orientated in alternate horizontal and vertical layers, with each layer being made of 192 bars. Each bar has the dimensions $9.61 \times 9.61 \times 1864.3$ mm. The total mass of each FGD is 1.1 t.

The downstream FGD contains layers of water totaling 15 cm in thickness. Comparison of the interaction rates from the two FGDs enables a measurement of neutrino cross sections on water in a similar way to the PØD water-in and water-our comparisons.

Electromagnetic Calorimeter

The Electromagnetic Calorimeter [62] (ECal) surrounds the PØD, FGDs and TPCs on all but the upstream side of the group of detectors. Its main purpose is to measure the energy and direction of photons from pizero decays in order to enhance pizero cross section measurements. It can also be used as a veto for the inner detectors, and can be used to perform stand-alone cross section measurements on lead [63]. The ECal modules which surround the PØD can help separate muons from photons, enhancing PID in PØD analyses.

The ECal is separated into 13 modules. Six barrel-ECal modules surround the FGDs and TPCs: two on the sides, two on top and two on the bottom. The top and bottom pairs are separated in the middle to enable access to the inner detectors when the magnet is opened. A similar arrangement of six PØD-ECal modules surrounds the top, bottom and sides of the PØD. The final module, the downstream ECal (Ds-ECal), is the most downstream sub-detector of ND280, perpendicular to the beam direction.

The ECal is a sampling electromagnetic calorimeter. The modules are constructed from layers of lead sheets and scintillator bars. There are 34 layers in the Ds-ECal, 31 in the barrel and six in the PØD ECals. Each bar has a cross section of 4×1 cm with varying lengths depending on the module. These dimensions were chosen to ensure sufficient granularity to resolve the position and direction of electromagnetic showers, and minimise the thickness of the ECal modules. The lead sheets are each 1.75 mm (4 mm) thick in the tracker (PØD) ECal. This thickness of lead was required to ensure the total thickness of lead in the ECal was at least 10 radiation lengths of the photons from pizero decays in order to contain at least 50% of their energy.

Side Muon Range Detector

The SMRD [64] is made up of scintillator modules installed in the air-gaps in the return yoke of the magnet. It measures the momentum of muon tracks at high angles to the neutrino direction, allowing access to events with higher momentum transfer. It can also act as a veto for the inner detectors.

The magnet yoke has 16 'C'-shaped layers, grouped into pairs axially around the ND280 detector. The pairs are labelled from 1 to 8 upstream to downstream. Each layer made of 16 steel plates. The SMRD is installed in the gaps between these layers.

Modules are installed in the three innermost gaps in the top and bottom of the magnet. In magnet yoke pairs 1-5, modules are installed in the three innermost gaps. In pair 6, modules are installed in the four innermost gaps, and in pairs 7 and 8, modules are installed in the five innermost gaps.

Modules consist of sets of scintillation counters. There are five in the side modules and four in the top and bottom modules. The modules must fit into the gaps in the magnet yoke, so those on the top and bottom are $875 \times 167 \times 7$ mm, and those in the side are $875 \times 175 \times 7$ mm.

4.3. Super Kamiokande

The Super Kamiokande (SK) detector [65] is located approximately 295 km from the T2K beam source, and is the far-detector of the T2K experiment. The purpose of the far-detector is to sample the flavour contents of the T2K beam after they have travelled from the beam source to SK.

SK is a 50 kt cylindrical water Cherenkov detector in the Mozumi mine of the Kamioka Mining and Smelting Company, 1 km under Mt. Ikeno in Gifu Prefecture, Japan. It is 42 m in height and 39 m in diameter. It is divided into two sections, an inner detector and outed detector, separated by a steel optically insulating structure.

The outer detector is 2 m in depth around the circumference of the cylinder, and on the top and bottom. It is instrumented with 1,185 outward-facing 20 cm photomultiplier tubes (PMTs). Its main purpose is to act as a veto for incoming cosmic rays in other (non-T2K) SK analyses, but it can also count incoming particles to help reject partially contained T2K events.

Inside the outer detector is a 50 cm thick steel structure which houses the phototubes for the inner and outer detectors. The outside of the structure is clad with Tyvek which allows reflection of light to maximise light collection by the outer PMTs. The inside is clad with a black plastic to minimise reflection, increasing the accuracy of vertex finding in the main detector volume.

The inner detector volume is 33.8 m in diameter and 36.2 m in height. It is instrumented with 11,129 50 cm PMTs, with 40% PMT coverage. The energy scale is calibrated using a number of sources, including a calibrated laser source and cosmic ray events. The scale is known to the %-level over a number of orders of magnitude.

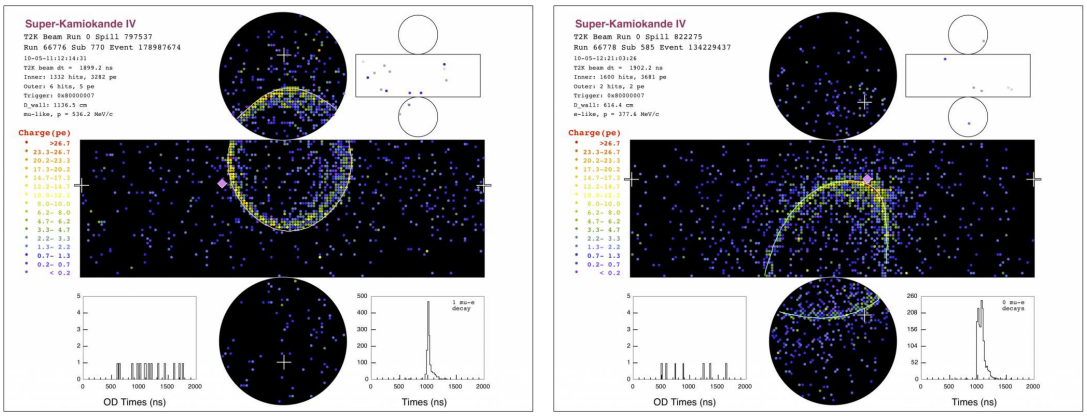

Figure 4.6.: Event displays of μ-like (left) and e-like (right) rings in SK.

The far-detector measures the flavour and energy of charged particles above Cherenkov threshold which traverse its volume. By selecting samples of events with a known mode composition, the true energy spectra of the different neutrino flavours can be reconstructed.

Events in SK are reconstructed by first finding the initial vertex and particle direction using PMT hit timing. A Hough transform is then performed on the PMT charge distribution to look for well-defined ring candidates. Next rings are classified as muon-like or electron-like. The different types of ring are distinguished by the clarity of the rings: muons from T2K beam events undergo little rescattering in the water which gives their Cherenkov rings sharply defined edges. Electrons from T2K beam events typically shower very soon after production, so the hit pattern of rings is less sharply defined. Finally, the particle momentum is reconstructed from the total measured PMT charge. Figure 4.6 shows event displays for muon- and electron-like rings in SK.

4.4. Neutrino beam simulation

A significant source of uncertainty in the T2K oscillation analyses comes from uncertainty in the neutrino flux. This arises from uncertainty in the products of the interaction of the beam with the target, and in the re-interaction of these products with the target. A dedicated experiment at CERN, NA61/SHINE, was performed in order to tune the T2K flux model to data [66]. In this experiment, a 30 GeV proton beam was incident on a thin graphite target and a replica T2K target, and the outgoing particles were measured [67].

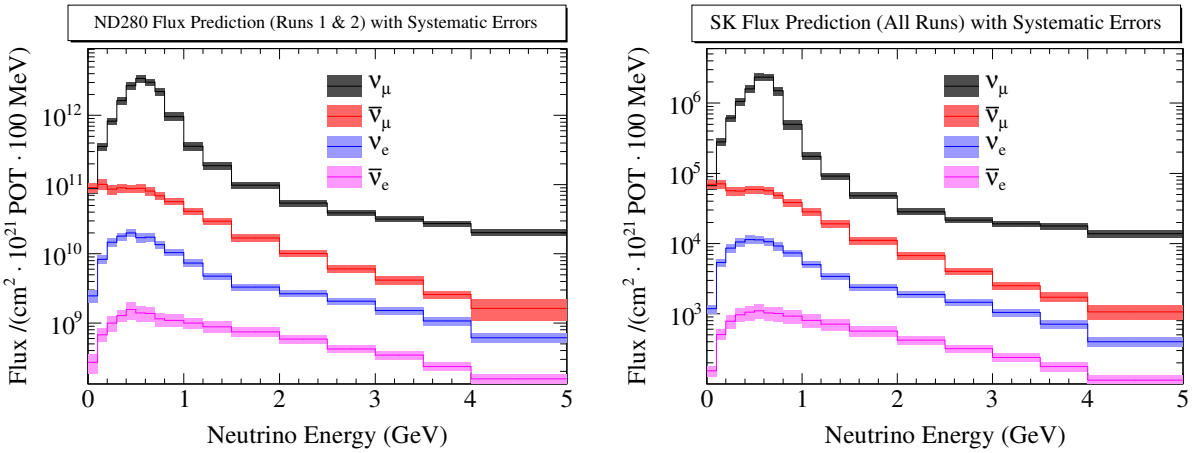

Figure 4.7.: Predicted flux with diagonal errors for all neutrino flavours at ND280 (left) and SK (right). Prediction shown for runs 1 and 2 for ND280, and 1-3c for SK. Both are normalised to 10^{21} POT.

Uncertainties in the NA61/SHINE data are typically 5-10% in the important regions of phase-space for T2K.

The predicted flux for all neutrinos from the beam at ND280 and SK are shown in Figure 4.7.

4.5. Data collection and simulation in ND280

ND280 produces data at a rate of a few MB per second, with files written to disk every few minutes. A robust hardware and software infrastructure is required to store, process, and analyse this data.

The software relies on standard particle physics libraries where possible. ROOT [68] is used for the event framework and storage, and GEANT is used as the basis for the simulation of particles propagating through the detector.

ND280 data is recorded in the MIDAS format, then converted for offline use into the bespoke T2K oaEvent format. The geometry of the ND280 detector is constructed in Geant4 [69] and converted to the ROOT TGeoManager format. Information from ND280 passes through the calibration chain using the bespoke oaCalib package. Once the calibrated hit-level information is available, physics objects—tracks, showers, PIDs *etc.*—can be reconstructed.

The most useful information for analysers is distilled and saved in the oaAnalysis file format. These are designed to contain relevant information for analysis, and be small enough to not require special storage arrangements.

Monte Carlo simulation is used to produce simulated oaAnalysis files which can then be used in analyses and compared to the ND280 data. This requires input from a physics model, simulated beam conditions, and a detector simulation. The beam conditions are simulated using information from the T2K beam monitors, and tuning from the NA61/SHINE experiments. Separate simulations are performed for periods in which the water bags in the PØD contain water or air, and separate simulations are performed for each horn configuration. The physics model can be input from either the NEUT or GENIE generators, though NEUT is used for all official oscillation analyses. Geant4 is used to simulate energy deposits from particles which pass through the detector, and the bespoke T2K package elecSim is used to simulate the response of the ND280 electronics to these energy deposits. MC events pass through a calibration chain similar to the data, and can then be reconstructed. From reconstruction onwards treatment of the MC is the same as treatment of the data.

4.6. Use of near-detector data to constrain far-detector expectations

A brief description of the use of near-detector data is necessary to provide background to later chapters. Specifically, it is necessary to focus on the role of cross section parameter errors in the oscillation analysis. This description is of the method used in the 2012 T2K oscillation analyses, and is largely the same in the 2013 analyses [70, 20].

In T2K analyses, oscillation parameters are obtained from measurements of interaction rates and energies in SK. Expected distributions are affected by parameters relating to the flux, and to the interaction cross sections. These can be constrained using near-detector data.

The basic statistical object which is minimised to obtain the oscillation parameters is the following log-likelihood function:

$$\begin{aligned}\ln\left[L(\vec{b},\vec{x},\vec{o},\vec{s}|d_{\mathrm{ND280}},d_{\mathrm{SK}})\right] = &\ln\left[P(d_{\mathrm{ND280}}|\vec{b},\vec{x},\vec{s})\right] + \ln\left[P(d_{\mathrm{SK}}|\vec{b},\vec{x},\vec{o})\right] \\ &+ \ln\pi(\vec{b}) + \ln\pi(\vec{x}) + \ln\pi(\vec{s})\end{aligned} \tag{4.1}$$

where $\vec{b}$, $\vec{x}$, $\vec{s}$, and $\vec{o}$ are vectors of the parameters which affect the far-detector prediction, relating respectively to beam, cross section, detector systematic errors and oscillation. L is a likelihood of parameters given some data, d are the data, and the π parameters are multivariate Gaussian distributions describing the prior uncertainty and covariance of the flux or cross section parameters:

$$\ln \pi(\vec{x}) = -\frac{1}{2}(\Delta x)(V_x^{-1})(\Delta x)^T \tag{4.2}$$

where Δx is a vector containing the deviation of each parameter from the nominal value, and V is the covariance matrix of prior uncertainties.

In practice, simultaneous fitting of near and far detector data is unnecessary, and the fit can be done in two steps. First the best-fit flux and cross section parameters are obtained by minimising a likelihood associated with just ND280 data:

$$\begin{aligned} \ln\left[L(\vec{b},\vec{x},\vec{s}|d_{\mathrm{ND280}})\right] = &\ln\left[P(d_{\mathrm{ND280}}|\vec{b},\vec{x},\vec{s})\right] \\ &+ \ln\pi(\vec{b}) + \ln\pi(\vec{x}) + \ln\pi(\vec{s}) \end{aligned} \tag{4.3}$$

Second, the fitted central values and covariances for the flux and cross section parameters are used as priors in the fit to the far-detector data to obtain the oscillation parameters:

$$\ln\left[L(\vec{f},\vec{o}|d_{\mathrm{SK}})\right] = \ln\left[P(d_{\mathrm{SK}}|\vec{f},\vec{o})\right] + \ln\pi(\vec{f}) \tag{4.4}$$

where $\vec{f} = (\vec{b},\vec{x})$ is a vector containing the flux and cross section parameters, which may be correlated after the ND280 data fit.

4.7. Status of T2K

Prior to the start of the T2K experiment, the far-detector was already in operation as a stand-alone experiment. Construction of the neutrino beamline began in April 2004 and was completed in 2009. Construction of the PØD, FGDs, TPCs, SMRD and Ds-ECal was completed in 2009, and the other ECal modules were completed in 2010.

T2K began accumulating data in January 2010. In March 2011, the detector was shut down following the 2011 Tōhoku earthquake and tsunami. The detector was brought back online in March 2012. As of July 2013, T2K had accumulated data corresponding to 6.63×10^{20} protons on target (POT) in the far-detector, and 5.90×10^{20} POT in the

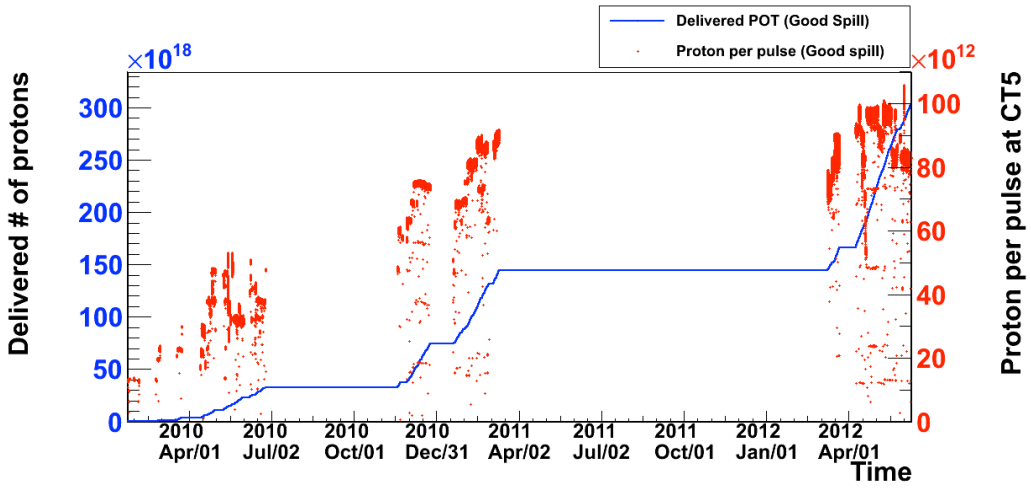

Figure 4.8.: Accumulation of protons on target from the start of T2K to May 2013.

near-detector as of November 2013. Figure 4.8 shows the accumulation of POT at SK from the start of the experiment in 2010 to May 2013.

The first T2K result was an indication of electron neutrino appearance, published in 2011 [19]. The result was updated in 2012 [20] and 2013 [21], showing exclusion of zero θ_{13} at the level of 7.3σ, and sensitivity to δ when including the reactor constraints on θ_{13}. The first muon neutrino disappearance results were released in 2012 [15] and updated in 2013 [16]. The latest result in disappearance channel is shown in Figure 2.1, showing the world-leading limits on oscillation parameters. T2K has also published a measurement of the flux-integrated charged-current muon-neutrino cross section on carbon [71] and has several additional cross section measurements planned for release in 2014.

Chapter 5.

Pre-constraint of CCQE parameters for the 2012 oscillation analysis

In the T2K experiment, neutrino oscillation parameters are extracted from far-detector data by comparing the expected rate and shape of observables to that measured. The oscillation parameters change the flux of neutrinos arriving at the far detector, but the rate depends on both the flux received and the cross sections of interaction processes. To obtain the oscillation parameters we therefore need predictions for the expected flux (in the absence of neutrino oscillation) and for the interaction cross sections, as well as known uncertainties on all parameters which could affect the observed interaction rate.

The general structure of the T2K 2012a oscillation analysis was described in Section 4.6. The problem which this chapter addresses is how to set prior uncertainties on the CCQE interaction mode as an input to the T2K near-detector fit. In other words, how to obtain the prior covariance matrix V_x in Equation 4.2.

The prior is obtained by choosing a physics model, fitting the model to external data, and using the fits to inform the tuning of the model and the prior uncertainty to apply to the T2K fits. This process is described in Section 5.2 for parameters related to the CCQE interaction mode.

Closely related to the task of model fitting is the task of generating predictions for a model given different input parameters. For some parameters this poses a significant technical challenge due to the time taken to generate new sets of MC with different parameter values. This process can be made much faster, and thus the fitting of parameters be made possible, using the technique of Monte Carlo reweighting. In

Section 5.1, the creation and implementation of MC reweighting functions for parameters affecting the CCQE cross section is described.

5.1. Creation and validation of MC reweighting functions for changes in Fermi-gas parameters

For the 2012a T2K analyses, nuclear Fermi-momentum, p_F, and binding energy, E_b, are treated as nuisance parameters: they are varied in the fit to the ND280 data and the best-fit value is found (though their best-fit values are not propagated to the far detector fit as the near and far detectors have different target nuclei). In order for these parameters to be integrated into the ND280 fit with the other parameters in a unified way, they must have associated reweighting functions. This section describes the creation and validation of reweighting functions for p_F and E_b.

5.1.1. Principles of MC reweighting

In order to extract best-fit parameters from data, we need to predict event distributions with different values of the model parameters. The simplest way of doing this is to run the full MC simulation of the chosen model with different input parameters, however this can be prohibitively time-consuming. A more efficient method is to use the technique of MC reweighting. This involves calculating a weight for each event given a change in an underlying parameter from a nominal value. The weight is the relative probability of this event given the new parameter set compared to the nominal set. Weights for all events can often be calculated much faster than the time taken to produce a new set of MC.

There are a variety of methods of calculating weights for events. For some parameters there are analytical functions which can be computed to calculate probability ratios. For others, notably the FSI parameters, calculating the probability analytically can be CPU intensive. The strategy for these cases is to produce a number of MC sets with different values of the parameter, bin events by the value of some kinematic variable and calculate weights in each of these bins as a function of this parameter.

There are limitations to MC reweighting which must be considered when creating a reweighting function:

1. If there are areas of phase-space which are unpopulated given the nominal parameter value but populated given a different value, reweighting from the nominal MC will leave these areas unpopulated.

2. If a reweighting function increases the probability of a particular area of phase-space, the statistical error of the MC becomes amplified.

5.1.2. Creation and implementation of reweighting functions for p_F and E_b

The Fermi-gas and binding energy parameters affect the allowed range of momentum transfer from the nucleon to the nucleus. Higher p_F allows for more energy in the initial state, and requires more energy in the final state nucleons due to the Pauli-blocking effect. Higher E_b requires more energy transfer to overcome the binding potential.

The method employed to produce reweighting functions for these variables was to use NEUT to generate events with the nominal parameters and with various different values of the Fermi-gas parameters. Events are then binned by a kinematic variable which is sensitive to changes in the Fermi-gas parameters, and weights are calculated based on the populations of these bins as a function of p_F and E_b.

The reweighting functions are applied in bins of the magnitude of the 3-momentum of the muon, $|\mathbf{p}_\mu|$, and the angle between the initial state neutrino and the final-state muon, $\cos\theta_\mu$. These variables were chosen because they are directly measurable by the T2K detectors, and for CCQE interactions are generally the only source of information about the interaction. They are affected by the energy and momentum transfer in the event, so are sensitive to changes in the Fermi-gas parameters. The bin boundaries are shown in Table 5.1. This binning scheme was chosen to ensure high MC statistics in all relevant bins, and to have increased detail in the most populated region for CCQE events from the T2K beam.

The Fermi-gas reweighting functions were only to be applied to CCQE interactions, since CCQE interactions are particularly sensitive to the values of p_F and E_b. p_F limits the phase-space of the final-state nucleon, and E_b is not negligible compared to the typical energy transfer in CCQE interactions, so can also increase the likelihood of an event being Pauli-blocked. Other interaction modes, for example resonant Δ production, are

Reweighting function argument	Bin boundaries				
True $\|\mathbf{p}_\mu\|$ (MeV)	0	100	200	250	300
	350	400	450	500	550
	600	650	700	750	800
	900	1000	1100	1200	1300
	1400	1500	1600	1700	1800
	1900	2000	2500	3000	4000
	5000				
True $\cos\theta_\mu$	-1.000	-0.900	-0.800	-0.700	-0.600
	-0.500	-0.400	-0.300	-0.200	-0.100
	0.000	0.100	0.200	0.250	0.300
	0.350	0.400	0.450	0.500	0.550
	0.600	0.650	0.700	0.725	0.750
	0.775	0.800	0.825	0.850	0.875
	0.900	0.925	0.950	0.975	1.000

Table 5.1.: Bin boundaries for $|\mathbf{p}_\mu|$ and $\cos\theta_\mu$ which are used as arguments in the p_F and E_b reweighting functions.

not so affected due to typically higher energy and momentum transfers, or the production of final-state particles which are not Pauli-blocked.

Only changes in the shape of the $|\mathbf{p}_\mu|$–$\cos\theta_\mu$ distribution is encoded in the reweighting functions, not the normalisation. This is because the normalisation for CCQE interactions are encoded in a separate uncertainty, so a shape-only reweighting function was designed to reduce the correlation between these parameters, ensuring a better constraint on both.

Using NEUT version 5.1.4.2 (the default version for the 2012a analysis), a number of MC files were created, each containing 1.5×10^6 CCQE events. All parameters were set to the the NEUT default values, except p_F, E_b and the target atom. MC files were created with various values of p_F with E_b set to the nominal value for the given target (25 MeV for C^{12}, 27 MeV for O^{16}). The MC was created using each value of p_F in the set:

$$p_F = \{205, 210, 215, 217, 220, 225, 230, 235, 240, 245, 250, 255, 260, 265, 270\} \text{ MeV}. \quad (5.1)$$

Analogously, MC files were created with various values of E_b with p_F set to the nominal value for the given target (217 MeV for C^{12}, 225 MeV for O^{16}). The MC was created at all integer values of E_b in the range $15 \leq E_b \leq 45$.

MC files with these values of p_F and E_b were created for both C^{12} and O^{16} targets. For the response function on O^{16}, the input neutrino energy distribution was the ν_μ flux expected at the T2K far-detector assuming no neutrino oscillation. For the response function on C^{12}, the input neutrino energy distribution was the ν_μ flux expected at the T2K near-detector. These flux choices were made because the reweighting function on C^{12} is most important in the near detector which has a high fraction of carbon in the tracker section, and the reweighting function on O^{16} is most important at the far-detector, which is mostly water. The neutrino energy distributions are not expected to have a large effect on the reweighting functions.

For each MC file, a histogram of $|\mathbf{p}_\mu|$–$\cos\theta_\mu$ was filled. Figure 5.1 shows the $|\mathbf{p}_\mu|$–$\cos\theta_\mu$ distribution for the MC file with nominal values of E_b and p_F, and Figure 5.2 shows the ratio of the bin content of the histograms made using MC with high and low values of E_b and p_F to that of the nominal.

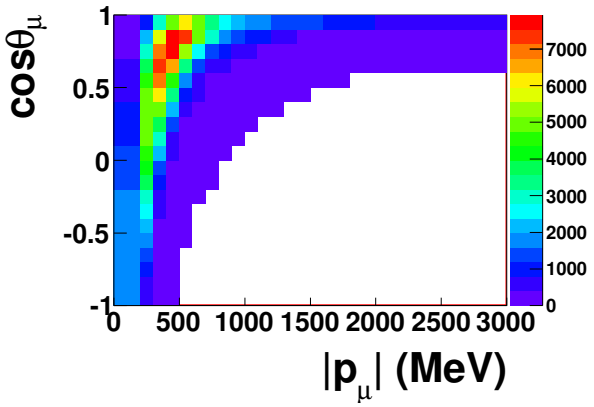

Figure 5.1.: $|\mathbf{p}_\mu|$–$\cos\theta_\mu$ distribution of events in a MC sample of ν_μ interactions on C^{12} with nominal p_F and E_b. Bins are shown with raw event numbers (no normalisation by bin width).

In each $|\mathbf{p}_\mu|$–$\cos\theta_\mu$ bin for all MC sets with the same target, the ratio of the bin entry to the nominal MC bin entry was calculated. A quadratic function was fit to the ratios in each bin as a function of p_F (E_b) with E_b (p_F) fixed to the nominal value, and this quadratic function is the reweighting function for p_F (E_b). Figures 5.3 and 5.4 show the

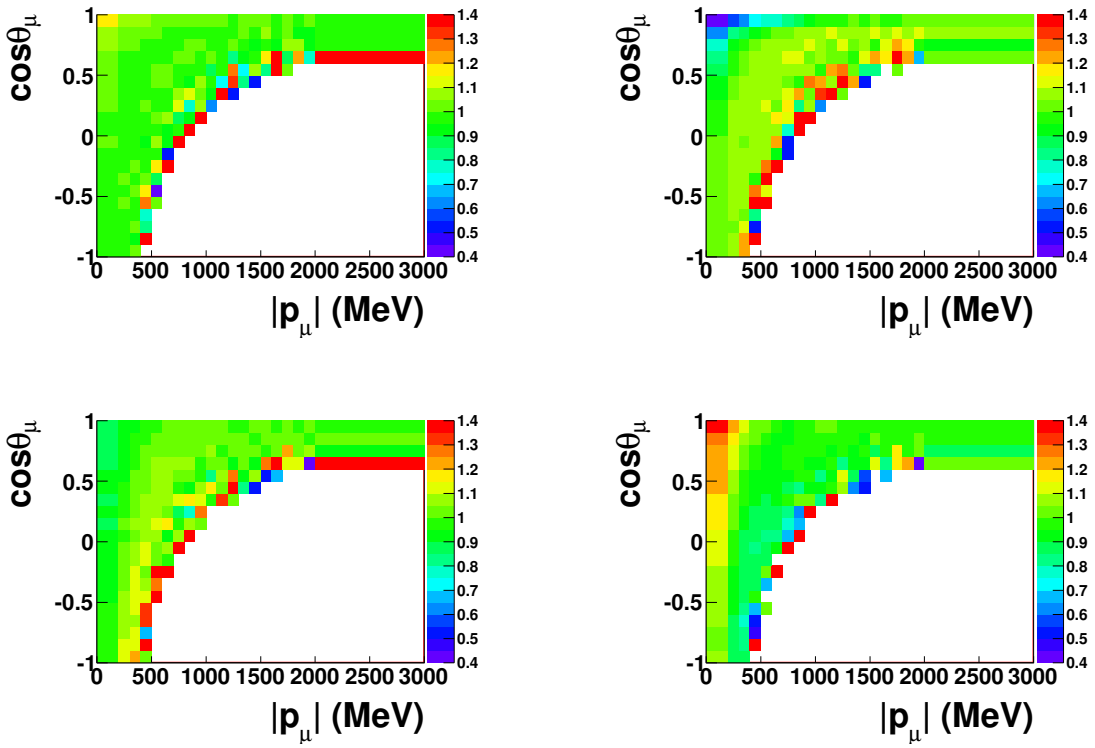

Figure 5.2.: Ratio of bin entries to that of nominal MC for MC with $\{E_b, p_F\} = \{25,205\}$ (top left), {25,270} (top right), {18,217} (bottom left) and {36,217} (bottom right).

ratio to nominal of selected bin entries for changes in p_F and E_b respectively, together with the quadratic fit.

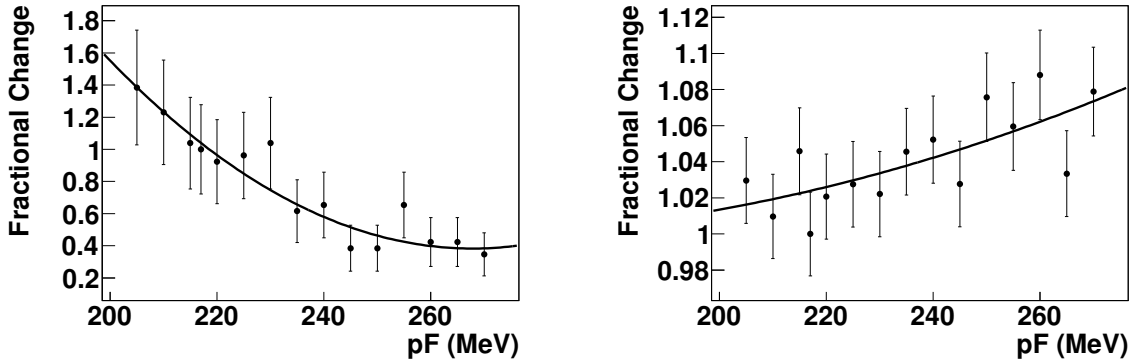

Figure 5.3.: Reweighting function for p_F in two $|\mathbf{p}_\mu|$–$\cos\theta_\mu$ bins. The ratio of bin content of this bin for each value of p_F is calculated with respect to bin content of the MC with nominal p_F, and a quadratic function is fit as a function of p_F. Ratios and fits shown for two bins: $0 \leq |\mathbf{p}_\mu| \leq$100 GeV and $0.97 \leq \cos\theta_\mu \leq 1.00$ (left) and $600 \leq |\mathbf{p}_\mu| \leq$650 GeV and $0.45 \leq \cos\theta_\mu \leq 0.50$ (right). Error bars are due to MC statistics

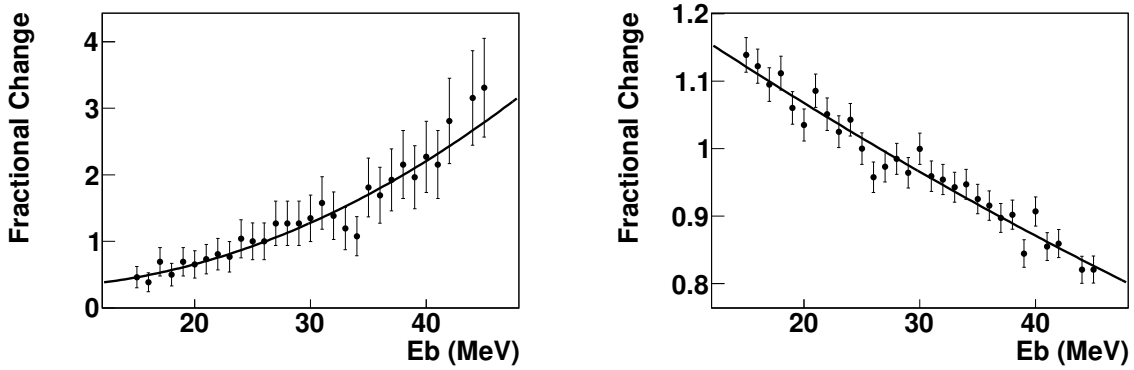

Figure 5.4.: Reweighting function for E_b in two $|\mathbf{p}_\mu|$–$\cos\theta_\mu$ bins. The ratio of bin content of this bin for each value of E_b is calculated with respect to bin content of the MC with nominal E_b, and a quadratic function is fit as a function of E_b. Ratios and fits shown for two bins: $0 \leq |\mathbf{p}_\mu| \leq$100 GeV and $0.97 \leq \cos\theta_\mu \leq 1.00$ (left) and $600 \leq |\mathbf{p}_\mu| \leq$650 GeV and $0.45 \leq \cos\theta_\mu \leq 0.50$ (right). Error bars are due to MC statistics

The event distributions change most at low Q^2 because Pauli-blocking affects the cross section more when the final-state nucleon momentum is low (which occurs most often when Q^2 is low).

The statistics of some bins are too small to reliably compute a response function using this method. This does not significantly affect the validity of the reweighting functions, since bins with very low statistics when producing these MC samples will also have low statistics in the official T2K MC (on which these reweighting functions are to be used in the oscillation analysis). Fitted reweighting functions for all bins were hand-scanned, and bins in which a fit was unreliable due to low statistics were recorded. In all such bins, the reweighting function was implemented to return unit weight. An example of a bin with low statistics and a fitted quadratic is shown in Figure 5.5. The reweighting function in this bin was rejected due to the size of the error bars in each point, and because some of the bins have no events. The result is a fit which is below unity for the entire range of the parameter.

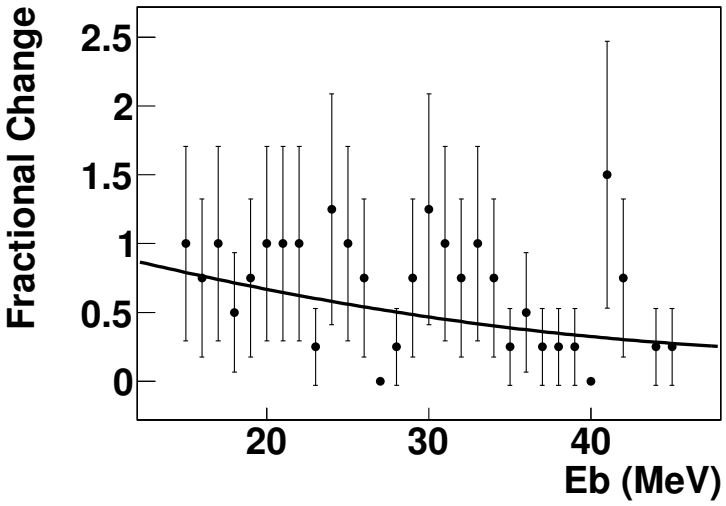

Figure 5.5.: Calculated reweighting function for E_b in the bin $750 \leq |\mathbf{p}_\mu| \leq 800$ GeV and $-0.2 < \cos\theta_\mu < -0.1$. In this bin, the statistics of the MC samples are too low to reliably compute a reweighting function.

The coefficients of the fitted quadratic polynomials were saved into histograms which can be accessed by the bespoke T2K reweighting library, T2KReWeight. Weights are calculated for CCQE events by first obtaining the values of $|\mathbf{p}_\mu|$ and $\cos\theta_\mu$ for that event, then obtaining the quadratic coefficients from the corresponding bins of the histograms, and finally evaluating the quadratic using those coefficients at the desired value of p_F or E_b.

5.1.3. Validation of p_F and E_b reweighting functions

A validation test was performed in order to test the implementation of the p_F and E_b reweighting functions. The purpose of the test was to ensure that histograms filled with nominal MC then weighted using the p_F and E_b reweighting functions were statistically consistent with histograms filled with MC produced at those values of p_F and E_b. In other words, to confirm that reweighted and regenerated MC were the same.

The procedure was as follows:

1. MC files were produced using NEUT 5.1.4.2 to generate 1.5×10^6 CCQE events of ν_μ on C^{12} (O^{16}), with E_ν picked according to the ND280 (unoscillated SK) ν_μ flux. One file was produced at each value of p_F from 5.1 with nominal E_b, and with each integer value of E_b in the range $15 \leq E_b \leq 45$ with nominal p_F. This set of MC is hereafter referred to as *regenerated* MC.

2. Two further MC files were produced in the same way as in the previous step, using the nominal values for p_F and E_b for each target.

3. For each event in the MC files with nominal p_F and E_b, weights were calculated using the p_F and E_b reweighting functions for the values of p_F in Equation 5.1, and for each integer E_b in the aforementioned range. The nominal MC together with the weights are referred to as *reweighted* MC.

4. For each reweighted and regenerated MC file, histograms of true T_μ–$\cos\theta_\mu$, Q^2–E_ν, T_μ, $\cos\theta_\mu$, Q^2 and E_ν were filled. For the reweighted MC, each event was entered into the histogram with a weight calculated in T2KReWeight.

5. The residual for each pair of regenerated/reweighted MC files with the same value of p_F (E_b) is defined in each bin as:

$$R_i = \frac{x_i^{\mathrm{rw}} - x_i^{\mathrm{rg}}}{\sqrt{\sigma_i^{\mathrm{rw}^2}\sigma_i^{\mathrm{rg}^2}}}, \tag{5.2}$$

where x_i is the content of bin i, σ_i is the statistical uncertainty in bin i and the 'rw' and 'rg' superscripts label reweighted and regenerated MC respectively. For each histogram and each value of p_F (E_b), the residual mean and standard deviation were calculated.

6. Residual means and widths for each pair of histograms were plotted as a function of p_F (E_b) for constant nominal E_b (p_F).

Residual means and widths as a function of p_F are shown in Figure 5.6, and as a function of E_b in Figure 5.7. If the reweighted and regenerated MC are consistent with being drawn from the same distribution, one would expect a residual mean of zero and a width of unity.

We see that the deviation from the ideal behavior is small when calculated from the T_μ–$\cos\theta_\mu$ distributions. When calculated from the 1D T_μ or $\cos\theta_\mu$ distributions, the residuals appear also to exhibit the ideal behavior, however the statistical errors are large due to the low number of bins in these histograms. The residuals calculated from the other distributions do not exhibit the ideal behavior, indicating that the reweighting functions for the Fermi-gas parameters are not able to reliably calculate weights which allow the E_ν or Q^2 distributions to be calculated. This is an acceptable limitation because the fit to ND280 data is performed on T_μ–$\cos\theta_\mu$ data so proper performance in other variables is not essential for the integrity of the ND280 or SK data fits.

5.2. Pre-constraint of CCQE parameters using MiniBooNE data

Before calculating expectations for observable distributions in the T2K far detector, the flux and cross section models are tuned and constrained by fitting near-detector data. To perform the fit to the near-detector data, we must have prior uncertainties on the systematic parameters. The priors are obtained by taking into account previous knowledge of these parameters from other sources. The MiniBooNE experiment performed a number of cross section measurements which are relevant for neutrino energies near the T2K flux peak and these measurements were used to tune the interaction model in NEUT.

This section describes the use of the MiniBooNE CCQE cross section measurements to constrain parameters related to the CCQE interaction in NEUT. First, the cross section uncertainties in T2K analyses are discussed generally, with emphasis on the procedure by which the parameterisation of the systematic errors is defined. Next, the MiniBooNE dataset is described, and the procedure for simulating the MiniBooNE data in NEUT is explained. A procedure for fitting the MiniBooNE data is then defined. A study is performed to validate the fitting procedure. Finally, a NEUT MC sample is fit to the

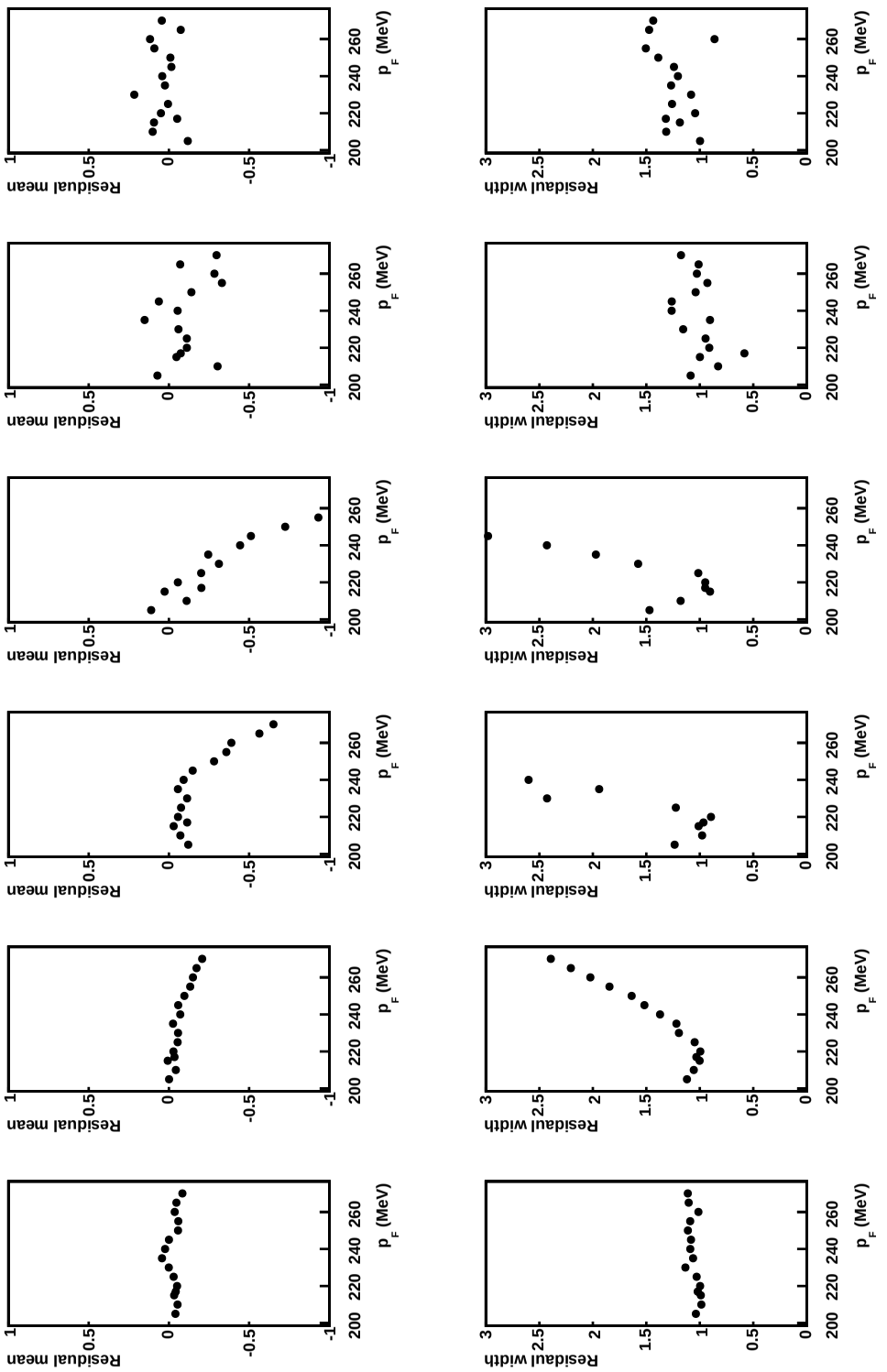

Figure 5.6.: Residual means (left) and widths (right) as a function of p_F at constant (nominal) E_b. Residuals were calculated from the following histograms (top to bottom): $\cos\theta_\mu$, T_μ, E_ν, Q^2, Q^2–E_ν, T_μ–$\cos\theta_\mu$.

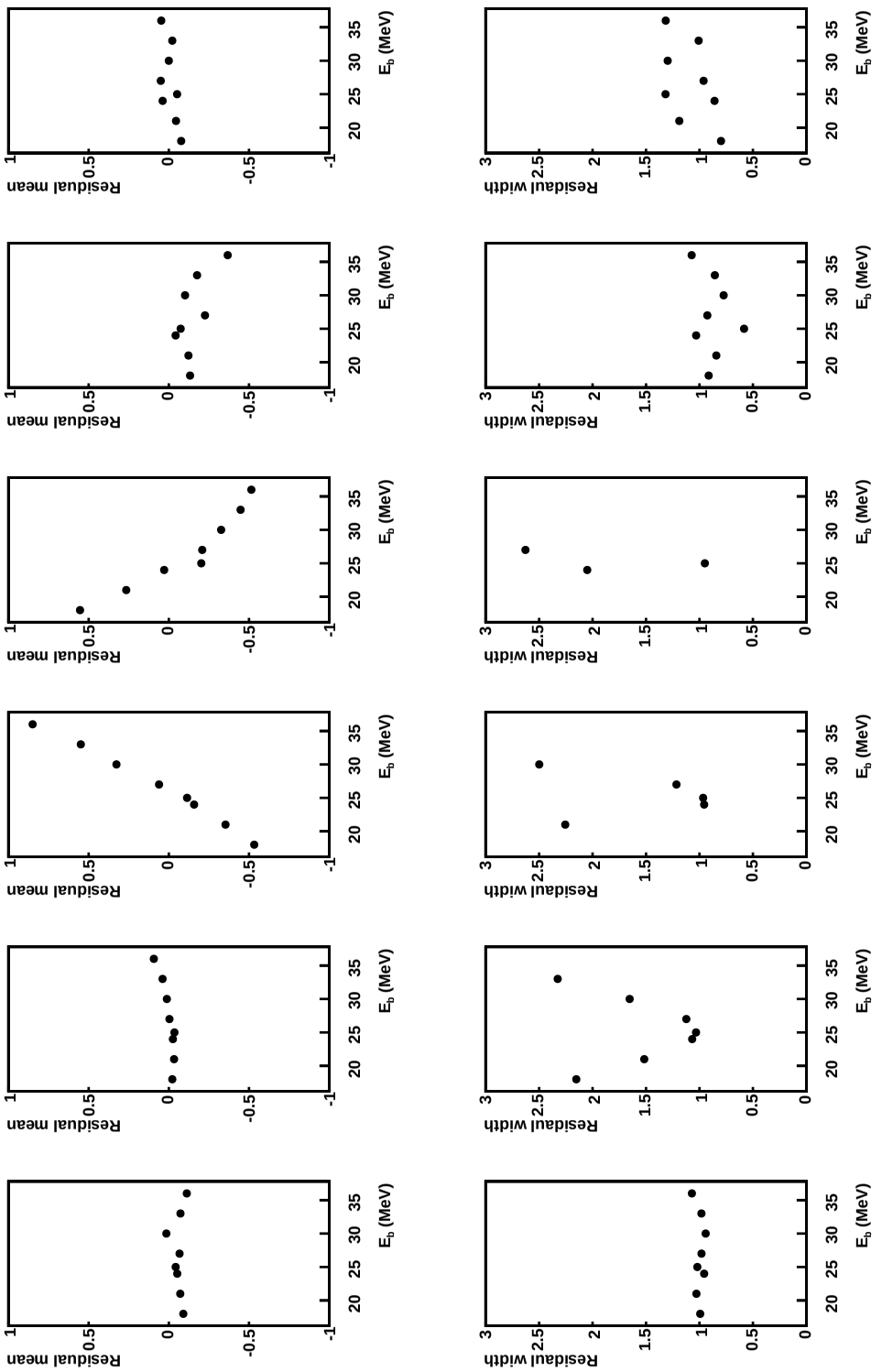

Figure 5.7.: Residual means (left) and widths (right) as a function of E_b at constant (nominal) p_F. Residuals were calculated from the following histograms (top to bottom): $\cos\theta_\mu$, T_μ, E_ν, Q^2, Q^2–E_ν, T_μ–$\cos\theta_\mu$.

MiniBooNE data, followed by a discussion on the use of the fits in the constraint of the cross section systematic parameters in the near-detector fit.

5.2.1. Overview of systematic uncertainties on neutrino interactions in the T2K 2012a oscillation analysis

Many neutrino interaction models contain parameters which are not fixed by the theory, and are free to be fit to data in order to produce better agreement. This is the case with many of the models in NEUT. However, even after free parameters are tuned, models often do not predict data with sufficient accuracy. On this point there is a methodological divide: is it better to adhere strictly to the predictions of the models and accept some deviation from data, or is it better to further tune the model by introducing additional, ad hoc parameters? For the purpose of the T2K near-detector fits, it was judged more important to reproduce existing cross section data, so that deviations from expectations can be more confidently attributed to the effects of neutrino oscillations. To this end, the second approach was taken, and additional parameters were introduced to allow the model more flexibility to reproduce cross section data.

The complete list of neutrino interaction cross section parameters which are included in the near-detector data fit is shown in Table 5.2, and is taken from [72]. These parameters can be tuned to make the prediction of the model look more like available data, and to inform the prior uncertainty to assign to each.

5.2.2. MiniBooNE CCQE-corrected data

The data that was used to tune the parameters of the CCQE model was the MiniBooNE CCQE-corrected measurement [43]. The data are of the true (nucleon-level) CCQE events with ν_μ on CH_2. The 'corrected' term refers to the process of correcting the cross section to true-CCQE from an original sample of CCQE-like events, which were selected based on track topology. The data are presented as a total cross section as a function of reconstructed neutrino energy E^{ν}_{QE}, and as flux integrated differential cross sections $d\sigma/dQ^2_{\mathrm{QE}}$ (where Q^2_{QE} is reconstructed momentum exchange) and $d^2\sigma/dT_\mu d\cos\theta_\mu$ (where T_μ is the kinetic energy of the final-state muon, and $\cos\theta_\mu$ is the angle between the

Parameter	Description
$M_{\mathrm{A}}^{\mathrm{QE}}$	Axial mass in the form-factor governing shape and normalisation of CCQE cross section
p_F	Maximum momentum of bound nucleons due to Fermi-motion. Separate nominal values for p_F in oxygen and carbon
E_b	Binding energy of bound nucleons. Separate uncertainties for E_b in oxygen and carbon
Spectral function	Uncertainty parameterising the difference between predictions made assuming Fermi-gas model for nuclear motion compared to the more rigorous spectral-function model
M_A^{res}	Axial mass in the form-factor governing shape and normalisation of resonant mode cross sections (i.e. those involving the excitation of the target nucleon)
CCQE normalisation	Three empirical parameters governing absolute normalisation of CCQE cross section at different neutrino energies
CC1π^0 normalisation	Two empirical parameters governing absolute normalisation of CC1π^0 cross section at different neutrino energies
NC1π^0 normalisation	Empirical parameter governing absolute normalisation of NC1π^0 cross section for all neutrino energies
Charged-current coherent normalisation	Empirical parameter governing absolute normalisation of charged-current coherent cross section for all neutrino energies
W shape	Empirical parameter which affects the shape of the NC1π^0 spectrum
CC other shape	Empirical parameter which affects the shape of the inclusive charged current cross section
Other NC normalisation	Absolute normalisation of all NC modes not considered in any previous category

Table 5.2.: List and description of all neutrino interaction parameters with associated uncertainties in the fit to T2K near-detector data.

incoming and outgoing leptons). Q^2_{QE} is defined as:

$$Q^2_{QE} = -m^2_\mu + 2E^{QE}_\nu(E_\mu - \sqrt{E^2_\mu - m^2_\mu}\cos\theta_\mu), \tag{5.3}$$

and E^ν_{QE} is defined as

$$E^{QE}_\nu = \frac{2M'_n E_\mu - (M'^2_n + m^2_\mu - M^2_p)}{2(M'_n - E_\mu + \sqrt{E^2_\mu - m^2_\mu}\cos\theta_\mu)}, \tag{5.4}$$

where E_μ is the muon energy, M_n, M_p and m_μ are the neutron, proton and muon masses, and $M' = M_n - V$ where $V = 34$ MeV is the binding energy of carbon assumed in the MiniBooNE analysis. Histograms of the MiniBooNE CCQE-corrected data from [43] are shown in Figure 5.8.

The MiniBooNE CCQE-corrected measurement is performed by selecting CCQE-like events (defined by event topology), then using a combination of MC and data to subtract non-CCQE backgrounds and compensate for detector efficiency, such that the final CCQE-corrected measurement is the cross section of only nucleon-level CCQE. The backgrounds which were subtracted were those in the NUANCE generator. The significance of this is that modes not included in the NUANCE model, such as multinucleon neutrino interactions, were not corrected, so are included in the CCQE-corrected dataset if present in nature.

The data are presented as central values and uncertainties in each bin, along with a 10.7% normalisation uncertainty. The binned uncertainties are a combination of the statistical and systematic uncertainties in the analysis and as such are probably correlated, however bin correlations were not included in the MiniBooNE data release. All bins are assumed to be uncorrelated in the fit, though this has a significant impact on the use of this data and on the interpretation of the fits: assuming all bins are uncorrelated presumes more information is in the dataset than there is in reality (to see this, consider the following example. Two measurements are uncorrelated, each with unit uncertainty. The correlation matrix is a 2×2 unit matrix. Rotating this matrix by $\pi/4$ and discarding the off-diagonal elements, we obtain $\mathrm{Diag}(1/\sqrt{(}2), 1/\sqrt{(}2))$, which has smaller normalisation than the original).

compare the amount of information in two uncorrelated measurements of the same parameter to two correlated measurements).

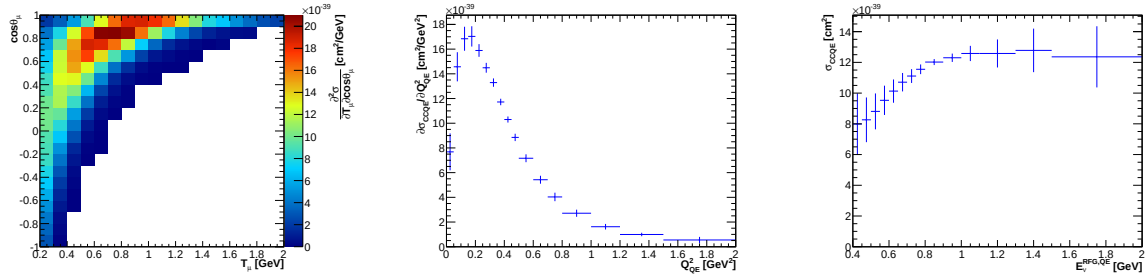

Figure 5.8.: MiniBooNE CCQE-corrected data. (T_μ–$\cos\theta_\mu$) (left), Q^2_{QE} (middle), E^ν_{QE} (right). Error bars show uncorrelated uncertainties only (a fully correlated 10.7% normalisation uncertainty not shown).

5.2.3. Simulating the MiniBooNE CCQE-corrected dataset in NEUT

An MC sample was produced containing 1.5×10^6 events of ν_μ on CH_2 (the MiniBooNE mineral oil target) with the MiniBooNE ν_μ energy spectrum [73]. All NEUT interaction modes were included in the simulation, but only true CCQE interactions were selected. The main parameters affecting the CCQE cross-section were set as follows:

$$M_{\mathrm{A}}^{\mathrm{QE}} = 1.21\ \mathrm{GeV}/c^2 \quad (5.5)$$

$$\text{CCQE Normalization} = 1.0 \quad (5.6)$$

$$p_F = 217\ \mathrm{MeV}/c \quad (5.7)$$

$$E_b = 25\ \mathrm{MeV}. \quad (5.8)$$

The other parameters were set as the NEUT default values.

To compare to the MiniBooNE data, histograms corresponding to the three MiniBooNE CCQE cross section measurements were filled. The T_μ–$\cos\theta_\mu$ histogram was filled using the true kinematic variables from the MC file, and histograms of Q^2_{QE} and E^ν_{QE} were filled by calculating these quantities according to Equations 5.3 and 5.4 respectively. The histograms were normalised to make them directly comparable to the equivalent data histograms. Each bin in the total cross section histogram was normalised using the following equation:

$$x' = \frac{x}{N_{MC} N_{\mathrm{nucl}} \int_{\mathrm{bin}} \Phi dE} \quad (5.9)$$

where x' is the normalised bin content (equivalent to the MiniBooNE data), x is the original bin content, N_{MC} is the total number of events in the MC file, $N_{\text{nucl}} = 14.08$ is the average number of nucleons in CH_2, Φ is the MiniBooNE flux, and the integral is performed over the width of the individual energy bin. The differential cross sections were normalised using a similar equation:

$$x' = \frac{x}{N_{MC} N_{\text{nucl}}} \frac{\int R dE}{\int \Phi dE} \tag{5.10}$$

where R is the interaction rate (flux×cross section) provided by NEUT, and both integrals are performed over the whole range of the MiniBooNE flux.

5.2.4. Definition of the χ^2 statistic

The χ^2 statistic that was used to compare the NEUT prediction to the MiniBooNE (spectral function)data was taken from the reference [44], in which a similar fit was performed using MC from the NuWro generator. The χ^2 is defined as:

$$\chi^2(\mathbf{x}) = \sum_{i=0}^{n} \left\{ \frac{\left(\frac{d^2\sigma}{dT_\mu d\cos\theta_\mu}\right)_i^{\text{data}} - \left(\frac{d^2\sigma}{dT_\mu d\cos\theta_\mu}(\mathbf{x})\right)_i^{\text{mc}}}{\Delta\left(\frac{d^2\sigma}{dT_\mu d\cos\theta_\mu}\right)_i} \right\}^2 + \left(\frac{\lambda^{-1} - 1}{\Delta\lambda}\right)^2 \tag{5.11}$$

where the index i runs over the n bins of the (T_μ–$\cos\theta_\mu$) distribution, $\left(\frac{d^2\sigma}{dT_\mu d\cos\theta_\mu}\right)_i^{\text{data (mc)}}$ is the measured (predicted) differential cross section in the i^{th} T_μ–$\cos\theta_\mu$ bin, $\Delta\left(\frac{d^2\sigma}{dT_\mu d\cos\theta_\mu}\right)_i$ is the uncertainty in the i^{th} T_μ–$\cos\theta_\mu$ bin, λ is the overall normalisation of the MC (i.e. $\lambda = 2$ would mean each MC event is filled with a weight of 2), $\Delta\lambda$ is the normalization uncertainty, set at 10.7% by MiniBooNE measurements, and $\mathbf{x}$ is a vector of parameters which are varied in each fit. The definition separates contributions to the χ^2 due to shape differences and due to normalisation differences. This is important when fitting a data-set in which the total normalisation uncertainty is large compared to the shape or statistical uncertainties. Including the normalisation as a fully-correlated error between bins can cause a systematic bias in the fit [74].

5.2.5. Validation of parameter fitter

The behavior of the χ^2 statistic defined in Equation 5.11 was investigated with a fake data study to confirm that the statistic was an unbiased estimator of the central value in a fit of NEUT to MiniBooNE data

The overall structure of the study was to produce a large number of fake-datasets with NEUT using known CCQE parameters, then fit MC to these datasets and compare the best-fit parameters to the known parameters in the fake-data.

Two sets of fake-data histograms were produced. The purpose of the first, hereafter referred to as Set A, was to check for bias in the fitted value of $M_{\mathrm{A}}^{\mathrm{QE}}$ when different values were used in the fake-data. The purpose of the second, hereafter referred to as Set B, was to check that the fitted error performed as expected when the fits were performed with different sized errors in the fake-data.

Set A was created according to the following procedure:

1. Produce 250 MC samples as described in Section 5.2.3
2. Reweight each histogram to 21 different values of $M_{\mathrm{A}}^{\mathrm{QE}}$ (yielding 250×21 sets of histograms. $M_{\mathrm{A}}^{\mathrm{QE}}$ was reweighted fractionally to values in the range [-0.4,0.4] at intervals of 0.04, with a nominal value of 1.21 GeV (i.e. $M_{\mathrm{A}}^{\mathrm{QE}} = \{1.21 \times (1 - 0.4), 1.21 \times (1 - 0.36), \ldots\}$).
3. For each histogram, choose a new value for the bin content by a random draw from a Gaussian with a mean set to the MC bin content, and a width set by the MC statistical error in that bin. 250 fake datasets were created for each value of $M_{\mathrm{A}}^{\mathrm{QE}}$.

Set B was created according to the following procedure:

1. Produce 250 MC samples as described in Section 5.2.3
2. Set the uncertainty on each bin to the uncertainty in the corresponding MiniBooNE data bin.
3. Scale the bin uncertainty in each bin by some factor to simulate lower statistics. Five different scale factors were chosen. Scale factors were set to simulate a reduction in statistics of 10^x where x is an integer between zero and five (i.e. the error bars in each bin are multiplied by $10^{x/2}$).

4. For each bin, draw a new central value by a random thrown from a Gaussian with a mean of the bin content and a width of the current bin error (after scaling in the previous step). Set all negative bin contents to zero.

A separate sample of NEUT MC was produced according to the procedure in Section 5.2.3 with nominal Fermi-gas parameters. This was fit to all fake datasets in Sets A and B by varying the $M_{\mathrm{A}}^{\mathrm{QE}}$ parameter and reweighting the MC until the value was found which minimises the χ^2 defined in Equation 5.11. The fit was performed using the Migrad ROOT fitter, and the uncertainty on the parameter was found by the fitter by estimating the curvature of the χ^2 surface at the minimum. This is a good approximation if the bin errors are Gaussian.

The bias on the best-fit $M_{\mathrm{A}}^{\mathrm{QE}}$ is evaluated by inspecting the residual (also known as the pull), which is defined as:

$$R = \frac{x^{\mathrm{fd}} - x^{\mathrm{fit}}}{\sigma^{\mathrm{fit}}} \tag{5.12}$$

where $x^{\mathrm{fd\ (fit)}}$ is the true (best-fit) value of the parameter (i.e. if $M_{\mathrm{A}}^{\mathrm{QE}}$ is fractionally increased by 0.2 for a particular fake-data set, $x^{\mathrm{fd}} = M_A^{QE,nominal} \times (1 + 0.2)$), and σ^{fit} is the uncertainty on the parameter found by the fitter. If values of the parameters at the minimum of the χ^2 statistic defined in Equation 5.11 are unbiased estimators of the true value, one would expect that the distribution of the residuals for many fits would be Gaussian with a mean of zero and a width of one. The width is expected to deviate from unity for fits in which the MC uncertainty in each bin is on the order of the fake data uncertainty, since the χ^2 function in Equation 5.11 does not take into account MC statistics. The assumption of negligible MC statistical errors is reasonable for fits to the real data since MC statistical errors will be much smaller than the data uncertainties.

Fits to all fake datasets in Sets A and B were performed. For each fit, the residual in Equation 5.12 was calculated. For Set A, the residuals of all 250 fits to each value of $M_{\mathrm{A}}^{\mathrm{QE}}$ in fake-data were binned into histograms. For Set B, the residuals of all 250 fits to each level of simulated statistics were binned into histograms. Gaussians were fit to all residual histograms. Two examples of these residual distributions with Gaussian fits are shown in Figures 5.9 (for a fit to Set A) and 5.10 (for a fit to Set B).

For Set A, the means and widths of all Gaussians which were fit to the residuals were plotted as a function of the fractional deviation from nominal $M_{\mathrm{A}}^{\mathrm{QE}}$. This shows whether there is any bias in the fitted parameters at different values of $M_{\mathrm{A}}^{\mathrm{QE}}$ (e.g. if there

was some slope in the residual means or widths as a function of $M_{\mathrm{A}}^{\mathrm{QE}}$). The residual means are shown in Figure 5.11 and the residual widths are shown in Figure 5.12. The behaviour of the residual means and widths is stable as a function of $M_{\mathrm{A}}^{\mathrm{QE}}$; there is no evidence of slope in either parameter as a function of $M_{\mathrm{A}}^{\mathrm{QE}}$ given the statistical errors of the fits. The mean tends by be greater than zero by approximately 0.15 over the whole $M_{\mathrm{A}}^{\mathrm{QE}}$ range. This is not consistent with zero, though it is small compared to the widths of the residual distributions which is approximately 0.7. The residual widths shown in Figure 5.12 are generally less than one, showing that σ^{fit} tends to overestimate the uncertainty on the measurement. Deviations from the ideal Gaussian behaviour may be caused by neglecting the MC statistical error in the χ^2 definition: exclusion of the statistical error from the χ^2 in each bin will result in a larger contribution from each bin. Taken together, this will cause the minimum χ^2 to be higher, and the χ^2 shape to be steeper away from the minimum than the curvature at the minimum would suggest (the fitted uncertainty is calculated from the curvature at the minimum). The effect of this on the fitted central value is unknown, and would depend on the details of the minimisation method.

For Set B, the means and widths of all Gaussians which were fitted to the residuals were plotted as a function of the fake-data statistics. The means are shown in Figure 5.13 and the widths are shown in Figure 5.14. The means exhibit a linear increase, with the means of the residuals for the lower-statistics fits being approximately zero, and the means of the highest-statistics residual being approximately 0.2. This increase is again relatively small compared to the width of the residual distributions, which is around 0.9. The statisitical significance of the trend is uncertain as there are few datapoints and large error bars: a change in the highest-statistics datapoint downwards by one sigma would make the trend much less striking. The widths of the residual distributions tend to be less than unity, meaning the uncertainty output by the fitter tends to overestimate the parameter error, possibly also due to the exclusion of the MC statistical error from the χ^2 definition. The exibited bias at higher statistics is not expected to contribute significantly to the fit to the MiniBooNE data, since the MiniBooNE data uncertainties are dominated by systematic errors which are much larger than the statistical errors, and very much larger that the MC statistical errors.

The conclusions of the fake data study are as follows:

- There is a small bias in the fitted uncertainty, resulting in a quoted uncertainty from the fit which is larger than the statistical spread of the results (i.e. the quoted uncertainty is conservative).

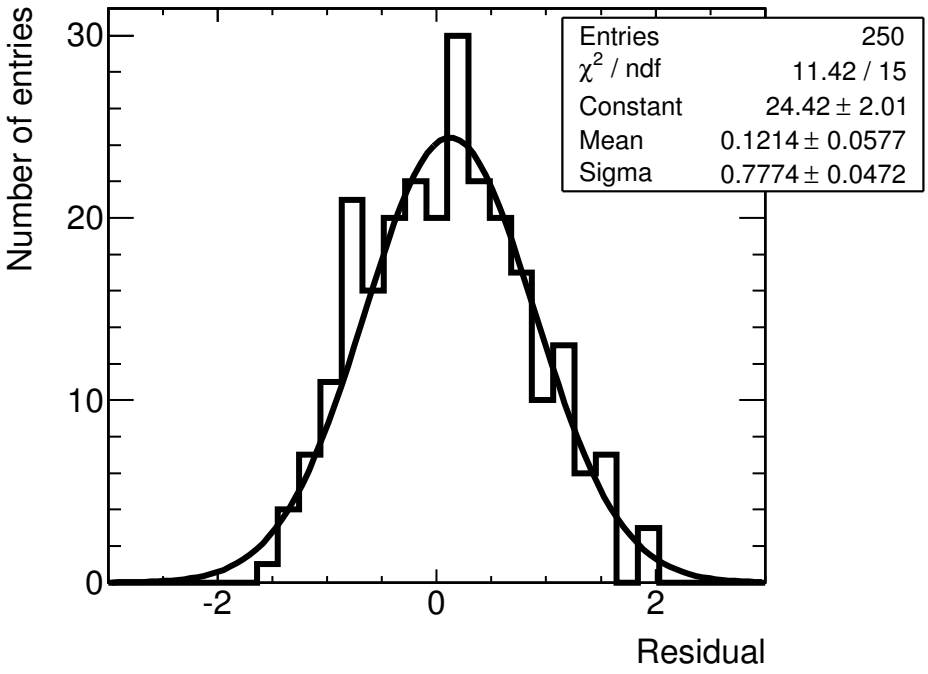

Figure 5.9.: Residual distribution and fitted Gaussian for 250 fits to fake data sets with $M_{\mathrm{A}}^{\mathrm{QE}} = 0.87$ GeV (fractional scaling of -0.28) with statistical errors equivalent to 1.5m events.

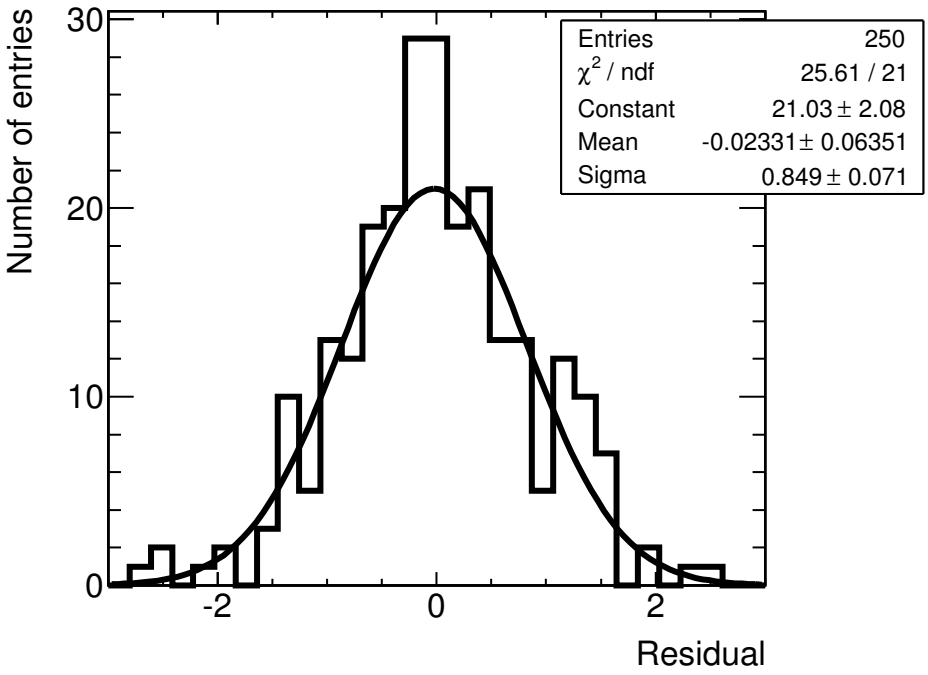

Figure 5.10.: Residual distribution and fitted Gaussian for 250 fits to fake data sets with $M_{\mathrm{A}}^{\mathrm{QE}} = 1.21$ GeV with statistical errors equivalent to 1.5k events.

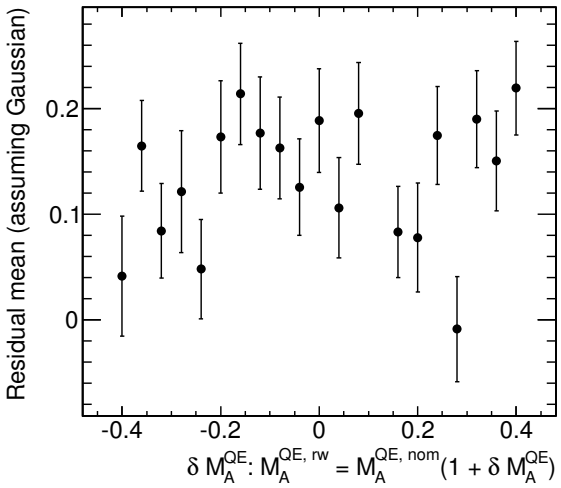

Figure 5.11.: Means of the residual Gaussians as a function of fake-data $M_{\mathrm{A}}^{\mathrm{QE}}$ (in terms of fractional reweighting from nominal). Error bars are uncertainties on the mean, not the width of the Gaussian.

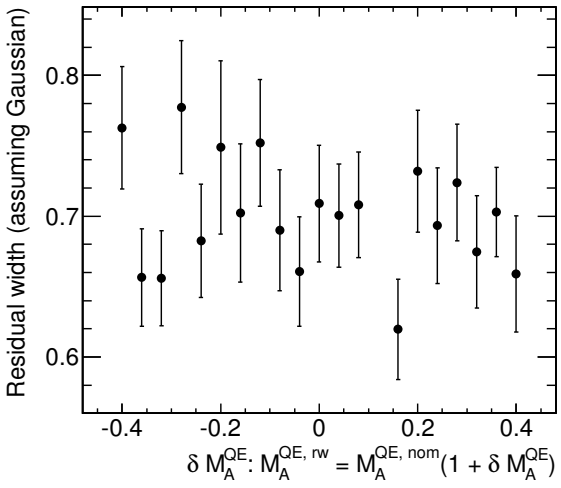

Figure 5.12.: Widths of the residual Gaussians as a function of fake data $M_{\mathrm{A}}^{\mathrm{QE}}$ (in terms of fractional reweighting from nominal). Error bars are uncertainties on fit widths.

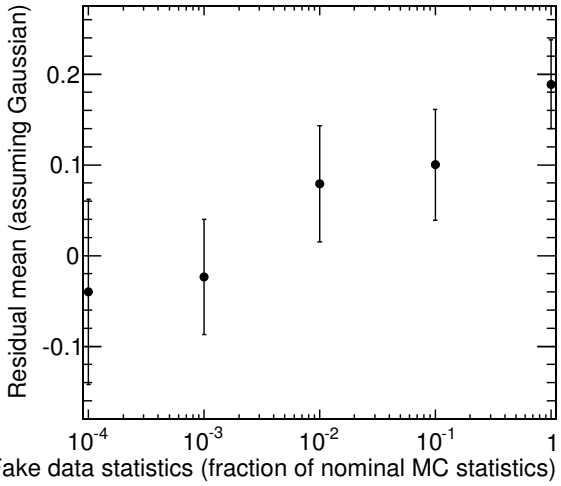

Figure 5.13.: Means of the residual Gaussians as a function of fake data statistics. The equivalent number of events in the fake-data samples is shown on the x-axis (i.e. the fake data corresponding to the data-point at 10^{-4} has a statistical error equivalent to 150 events ($1.5 \times 10^6 \times 10^{-4}$). Lowest statistics fake data sets produced too few good fits to fit a Gaussian, so that data point is not shown here. Error bars shown here are the uncertainties on the fitted means, not the width of the fitted Gaussian.

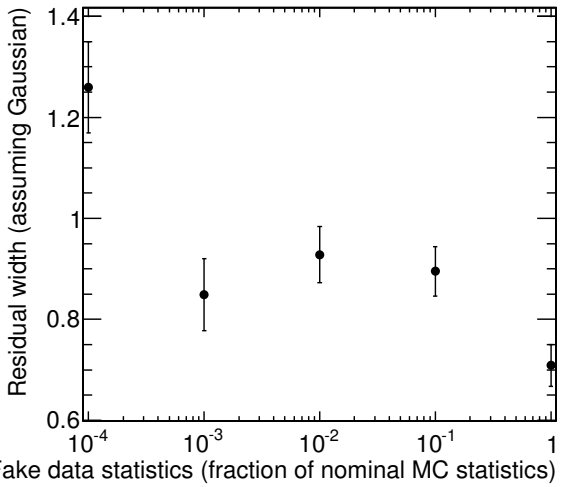

Figure 5.14.: Widths of the residual Gaussians as a function of fake data statistics. Lowest statistics fake data sets produced too few good fits to fit a Gaussian, so that data point is not shown here. Error bars shown here are the uncertainties on the fitted widths.

- There is a small bias in the fitted central value, favouring larger values of $M_{\mathrm{A}}^{\mathrm{QE}}$. The size of the bias is small compared to the statistical spread of the fitted values. This is something which could be quantified and corrected for in the future, but the effect is suitably small that this is not done in the present analysis.

5.2.6. Fitting NEUT MC to MiniBooNE data

Fits to the MiniBooNE data were performed with several different sets of variable parameters. The quality of a parameterisation was judged by the improvement in the agreement between the MC and the data after the fit, and how well the parameters were constrained by the data. The two best parameter sets are referred to as the *minimal* and *extended* parameterisations. The minimal parameterisation included only $M_{\mathrm{A}}^{\mathrm{QE}}$ and the CCQE mode normalization. The CCQE normalization is necessary in the minimal parameterisation due to the 10.7% uncertainty on the MiniBooNE flux. The extended parameterisation included $M_{\mathrm{A}}^{\mathrm{QE}}$, the CCQE mode normalisation, and the Fermi-gas parameters E_b and p_F. This allowed the fit greater flexibility at low Q^2.

Fits were performed using the MiniBooNE CCQE-corrected T_μ–$\cos\theta_\mu$ data, by minimising the χ^2 in Equation 5.11.

The output of the fit with the minimal parameterisation was:

$$M_A^{QE} = 1.64 \pm 0.03 \text{ GeV} \quad (5.13)$$

$$\text{CCQE Normalization} = 0.88 \pm 0.02 \quad (5.14)$$

$$\chi^2_{\mathrm{min}}/\mathrm{DOF} = 26.9/137 \quad (5.15)$$

Comparison of the MC prediction with the data as a function of (T_μ–$\cos\theta_\mu$), Q^2_{QE} and E^{ν}_{QE} is shown in Figure 5.15. Ratios of MC/data are shown in Figure 5.16.

The $\chi^2_{\mathrm{min}}/DOF$ for the fit is well below unity. This is because the errors in all bins are assumed uncorrelated, though it is likely that correlations between the data-points are non-negligible. The low $\chi^2_{\mathrm{min}}/DOF$ therefore does not necessarily indicate a good fit. It can be seen in Figures 5.15 and 5.16 that both the nominal MC and the best fit MC overestimate the data at low Q^2_{QE} and underestimate at high Q^2_{QE}. This occurs because of the large discrepancy between the data and the nominal MC at low Q^2_{QE}: the value of $M_{\mathrm{A}}^{\mathrm{QE}}$ is driven upwards and the CCQE normalization driven downwards to try to make the low Q^2_{QE} region in MC agree with data.

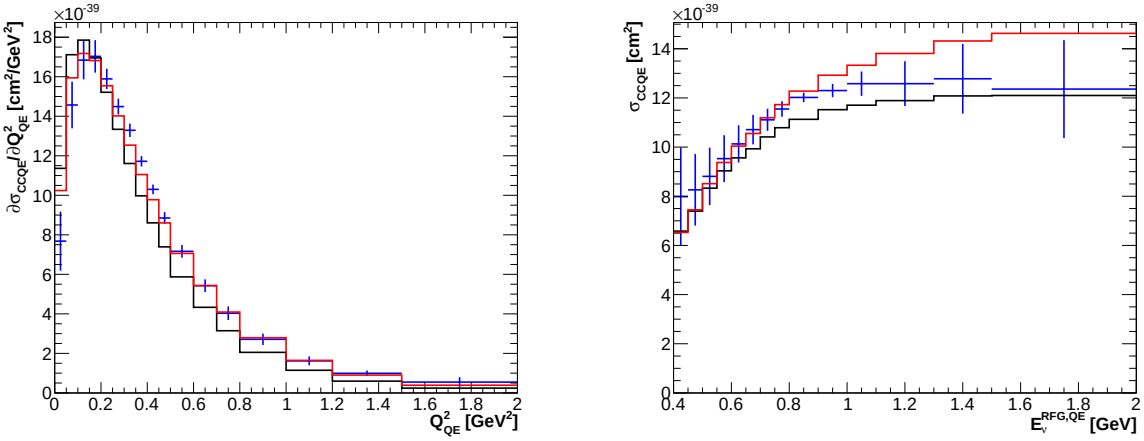

Figure 5.15.: Comparison of data with nominal and fit MC for the minimal parameterisation. Left: Q^2_{QE} distribution for data (blue crosses), nominal MC (black) and best fit MC (red). Right: E^{ν}_{QE} distribution for data (blue crosses), nominal MC (black) and best fit MC (red).

From the fits with the minimal parameterisation it was observed that the fit required greater flexibility at low Q^2. This was the reason for the inclusion of the Fermi-gas parameters in the fit in the extended parameterisation.

A fit was performed using the same MC and the same dataset while floating all parameters in the extended parameterisation. The output of the fit was as follows:

$$M_A^{QE} = 1.45 \pm 0.05 \text{ GeV} \quad (5.16)$$

$$\text{CCQE Normalization} = 0.97 \pm 0.09 \quad (5.17)$$

$$p_F = 231 \pm 3 \text{ MeV} \quad (5.18)$$

$$E_b = 27 \pm 4 \text{ MeV} \quad (5.19)$$

$$\chi^2_{\mathrm{min}}/\mathrm{DOF} = 21.6/135 \quad (5.20)$$

Comparison of the MC prediction with the data as a function of (T_μ–$\cos\theta_\mu$), Q^2_{QE} and E^{ν}_{QE} is shown in Figure 5.17. Ratios of MC/data are shown in Figure 5.18. As well as having a lower χ^2_{min}/DOF, these fits show improved agreement at low Q^2_{QE} compared to the best fit with the minimal parameterisation. Aside from the first two bins, the Q^2_{QE} ratio is approximately flat for the best fit MC up to high Q^2_{QE}, where the data statistics become small. The ratio of the best fit MC to data increases as a function of E^{ν}_{QE}, which is characteristic of a large $M^{\mathrm{QE}}_{\mathrm{A}}$. This suggests a breakdown of this effective $M^{\mathrm{QE}}_{\mathrm{A}}$ parameter in the dipole approximation of the form factor—drastically inflating

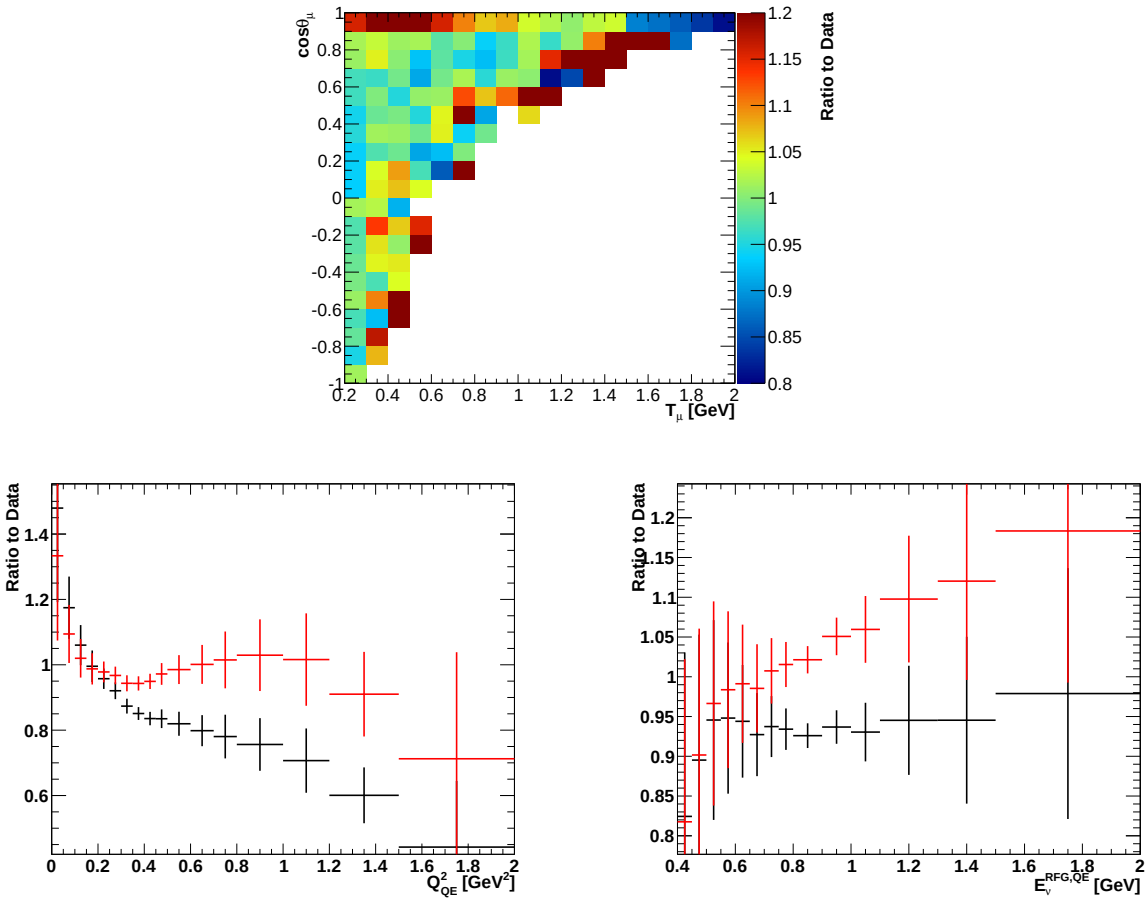

Figure 5.16.: Ratio of nominal and fit MC to data for the minimal parameterisation. Top: (T_μ–$\cos\theta_\mu$) ratio of best fit MC to data. Left: Nominal MC (black) and best for MC (red) ratio of Q^2_{QE} distribution to data. Right: Nominal MC (black) and best for MC (red) ratio of E^ν_{QE} distribution to data.

$M_{\mathrm{A}}^{\mathrm{QE}}$ from the nominal value makes the prediction agree better in Q^2_{QE} but not in E^ν_{QE}, showing that the value of this parameter is probably not the fundamental problem with the model. However the bins in this distribution are certainly correlated so it is difficult to gauge the true significance of this pathology. The excess of MC over data in the high $\cos\theta_\mu$ and low T_μ region of the T_μ–$\cos\theta_\mu$ distribution in the minimal parameterisation is no longer present with the extended parameterisation.

The extended parameterisation allows for more flexibility at low Q^2_{QE}, resulting in improved MC-data agreement in this region, though the price of this is a very large best-fit p_F, which is far from the nominal value of 217 MeV (in C^{12}). Inconsistency of the best-fit value with these measurements is not unexpected: the fit here uses p_F as a

proxy for describing MC-data disagreements, and the large best-fit value is a statement of the inconsistency of the MiniBooNE data with the NEUT QE model.

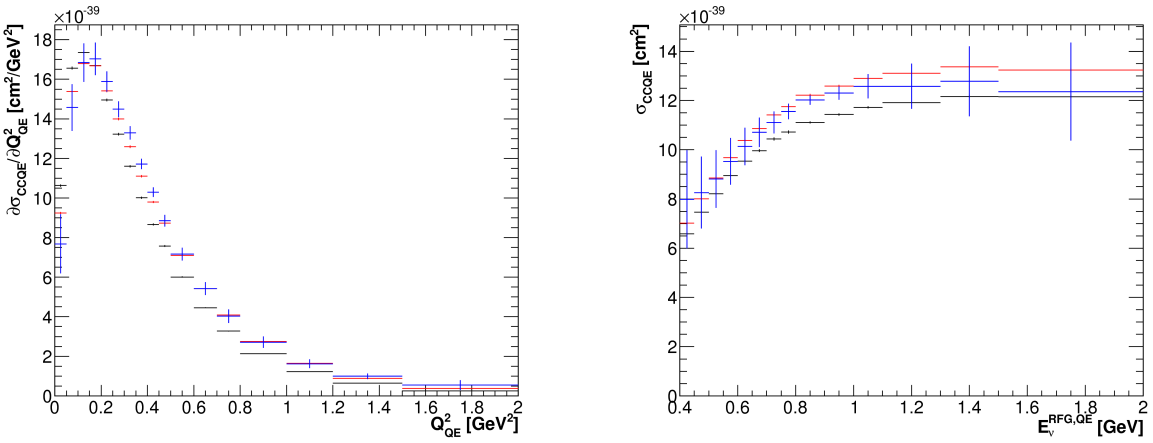

Figure 5.17.: Comparison of data with nominal and fit MC for extended parameterisation. Left: Q^2_{QE} distribution for data (blue crosses), nominal MC (black) and best fit MC (red). Right: E^{ν}_{QE} distribution for data (blue crosses), nominal MC (black) and best fit MC (red).

The values of the Fermi-gas parameters in the T2K near-detector data fits were set to the nominal values from external literature data. In order to maintain consistency with the T2K near-detector fits, it was decided to use the results of the fit to MiniBooNE data with the minimal parameterisation, despite the large difference between the best-fit $M_{\mathrm{A}}^{\mathrm{QE}}$ and the NEUT nominal value.

Since the bin correlations were not provided with the MiniBooNE data, the covariance from the fit was not used as an input into the T2K near-detector fit. The absence of correlations causes the parameters to be over-constrained, and the uncertainties to be artificially small. Use of the central value of the $M_{\mathrm{A}}^{\mathrm{QE}}$ parameter as the nominal value in the T2K near-detector fits was also problematic, since the value was so far from the nominal, caused by deficiencies in the model particularly at low Q^2. Instead, it was decided to set the nominal value of $M_{\mathrm{A}}^{\mathrm{QE}}$ and the CCQE normalisation in the near-detector fit to the nominal values of these parameters in NEUT (i.e. their untuned values), and to use the difference between the NEUT nominal and MiniBooNE fitted values as the prior uncertainty. This difference is very large, so the prior constraint on these parameters is very weak—certainly much weaker than the expected power of the T2K near-detector data fits to constrain them—so effectively all of the constraint on these parameters in the near-detector fits comes from near-detector data itself. The consequence is that the constraint on oscillation parameters is weaker, since some of the

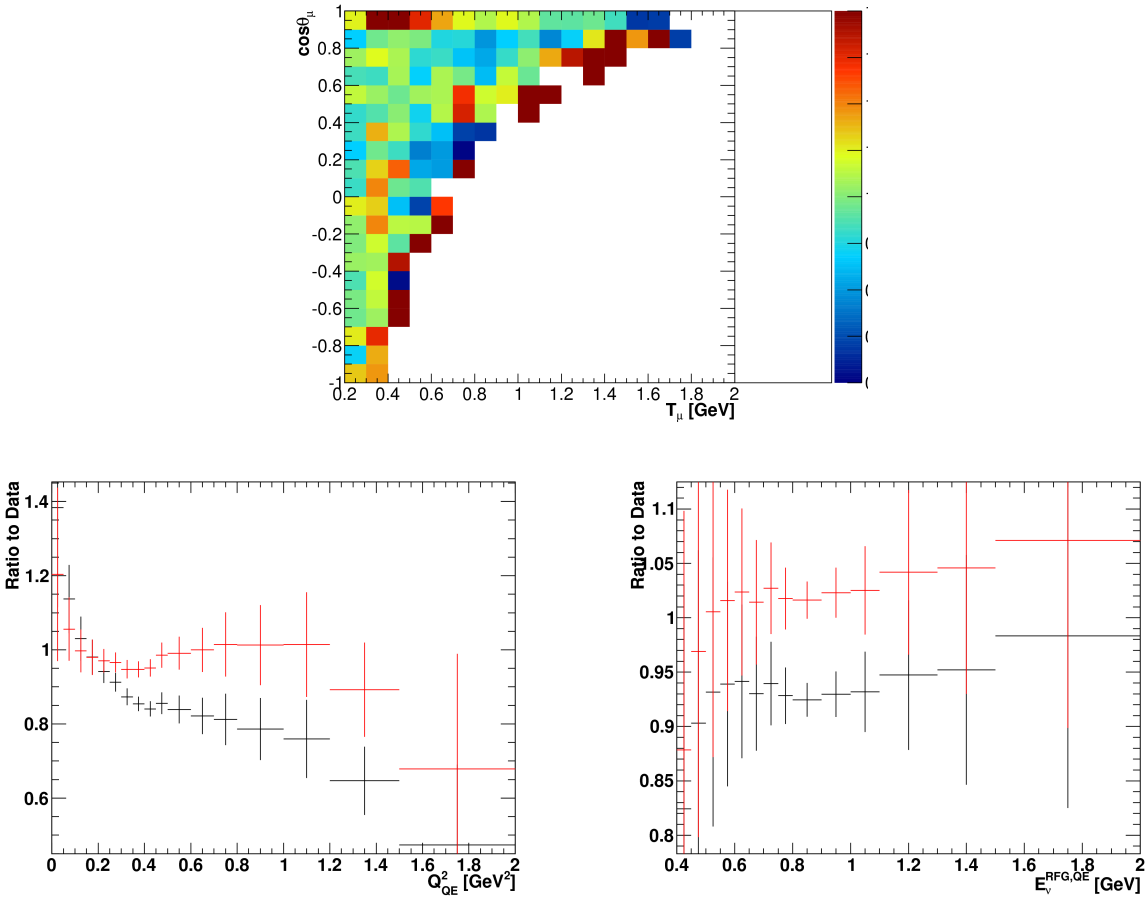

Figure 5.18.: Ratio of nominal and fit MC to data for extended parameterisation. Top: (T_μ–$\cos\theta_\mu$) ratio of best fit MC to data. Left: Nominal MC (black) and best for MC (red) ratio of Q^2_{QE} distribution to data. Right: Nominal MC (black) and best for MC (red) ratio of E^{ν}_{QE} distribution to data.

power of the near-detector data is used constraining cross section parameters, but it was judged safer to apply a conservative prior error on this parameter given the observed deficiencies in the model.

Comparison with published fits

The best-fit value of $M_{\mathrm{A}}^{\mathrm{QE}}$ found in the present fits, $M_{\mathrm{A}}^{\mathrm{QE}} \approx 1.6$ GeV, is significantly larger than three other published fits to the same dataset, which find a value of $M_{\mathrm{A}}^{\mathrm{QE}} \approx 1.35$ GeV. Table 5.3 shows best fit values extracted in these published analyses.

The main source of difference is the technique that is employed by each analysis to take into account the low-Q^2 behavior. This kinematic region is difficult since the

quasi-free model for the nucleons (the approximation that the bound nucleons can be considered as a collection of free nucleons with some momentum and a constant potential) becomes increasingly invalid towards low Q^2: as the spatial size of the probe becomes larger, the effects of nucleon correlations begin to contribute to the cross section.

In the fits performed by the MiniBooNE collaboration, the low-Q^2 behaviour was modelled by an effective parameter, κ, the effect of which was to increase the Pauli-blocking at low Q^2. In separate analysis performed by Juszczak *et al.* [44], bins which contained a large fraction of low-Q^2 events in MC were excluded from the fit entirely. In the present analysis, all bins were included in the χ^2 and no additional flexibility was added to the MC to model the low Q^2 behaviour. The fit found a relatively larger best-fit $M_{\mathrm{A}}^{\mathrm{QE}}$ in order to increase the cross section at higher Q^2, and a low value of the total CCQE normalisation in order to convert a higher cross section at high Q^2 to a lower cross section at low Q^2.

This idea is corroborated by comparing the best-fit $M_{\mathrm{A}}^{\mathrm{QE}}$ between the fits with the minimal and extended parameterisations, described in Section 5.2.6. When additional parameters are added to the fit which allow the cross section at low Q^2 to be scaled independently from $M_{\mathrm{A}}^{\mathrm{QE}}$, the best-fit $M_{\mathrm{A}}^{\mathrm{QE}}$ is more in-line with the other published fits.

An additional difference between the analyses is the generator used to make the predictions. The NUANCE generator is used for the MiniBooNE analysis, the NuWro generator in the analysis of Juszczak *et al.*, and NEUT in the present analysis. Differences in the nuclear models, CCQE interaction models, and default model parameters will all result in different predictions and ultimately different best-fit values. Additionally, different form factor models were used in the MiniBooNE and the present analysis. MiniBooNE used the BBA03 [75] model in NUANCE when generating MC whereas the dipole form-factor model was used in NEUT in the present fit. A similar model to BBA03, namely BBBA05 [76], was used to generate MC in NEUT and the fits found that the best-fit value of $M_{\mathrm{A}}^{\mathrm{QE}}$ was lowered by approximately 0.05 GeV.

The final difference between the analyses was in the MiniBooNE CCQE-corrected data itself. Although all analyses used the same bin central values, diagonal uncertainties and normalisation uncertainty, the MiniBooNE analysis had access to the full covariance matrix, whereas the Juszczak *et al.* analysis and the present analysis did not. In both of these analyses, the diagonal uncertainties were assumed to be uncorrelated. The effect of this can be clearly seen by comparing the size of the uncertainty on the best-fit $M_{\mathrm{A}}^{\mathrm{QE}}$ between the three fits: the uncertainty on the MiniBooNE fit is significantly larger

Analysis	Fit parameters	χ^2_{min}/ (DOF)
Juszczak *et al.* (Fermi gas) [44]	$M_{\text{A}}^{\text{QE}} = 1.350 \pm 0.066$ GeV	14.45 / 119
	λ=1.063	
Juszczak *et al.* (spectral function) [44]	$M_{\text{A}}^{\text{QE}} = 1.343 \pm 0.060$ GeV	23.2 / 119
	λ=1.23	
MiniBooNE [43]	$M_{\text{A}}^{\text{eff}} = 1.35 \pm 0.17$ GeV	47.0 / 38
	$\kappa = 1.007 \pm 0.012$	
present analysis (T2K 2012a)	$M_{\text{A}}^{\text{QE}} = 1.64 \pm 0.03$ GeV	26.9 / 135
	CCQE norm.$= 0.88 \pm 0.02$	

Table 5.3.: Summary of the best fit parameters for several fits using the MiniBooNE CCQE-corrected dataset

than the other two which appear to be over-constrained due to the lack of correlation information.

Chapter 6.

Implementation of a multinucleon interaction model into NEUT

It is vital for the integrity of the T2K oscillation analysis that the fits to both near and far-detector data be based on an accurate description of neutrino interactions. There is a growing body of evidence suggesting the nuclear and interaction models currently employed in most neutrino generators, including NEUT, are too simplistic to accurately describe certain features of quasi-elastic scattering and similar modes. In past experiments, these inaccuracies were unimportant due to large statistical errors, however in the current and future generations of experiments with large detectors and high intensity beams, the statistics are large enough that detailed understanding of systematics and interaction modelling is important. Sensitivity projections indicate that T2K measurements will become systematics limited within the next few years, and improving confidence in our interaction model is an important precursor to reducing systematic uncertainties associated with interaction modelling. This chapter describes work to improve the interaction model through the implementation of a multinucleon neutrino interaction mode (npnh) into NEUT.

6.1. Effect of multinucleon neutrino interactions in T2K

As described in Section 3.3.2, predictions for the multinucleon neutrino contribution to the total charged-current cross section are computed by a multi-body expansion of the W boson propagator in a nuclear medium. The first-order expansion gives a prediction for

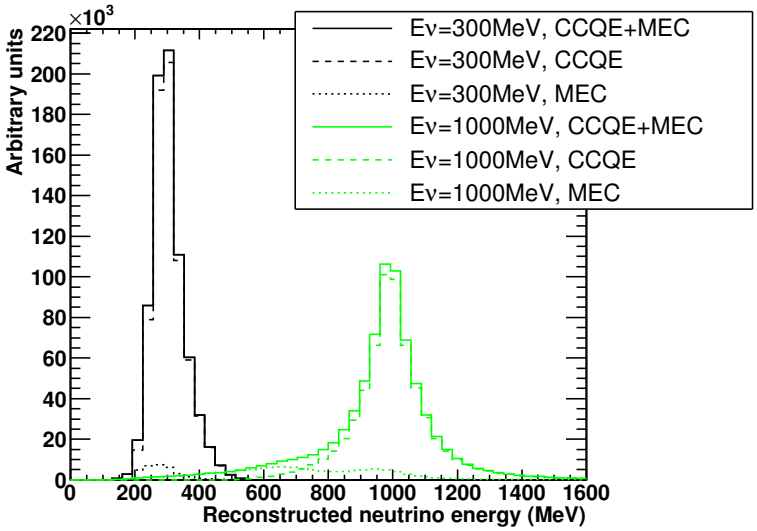

Figure 6.1.: Neutrino energy reconstructed from final-state lepton, assuming stationary target nucleon. Shown here are two neutrino energies, with sample of CCQE and npnh interactions (also known as MEC interactions).

the standard CCQE interaction, where the hadronic vertex involves a single nucleon-hole pair. The second-order terms in the expansion predict interactions involving additional nucleons or Δ resonances in the hadronic current.

In versions of NEUT up to and including 5.1.4.5, npnh interactions are not modelled so their effects have not directly been considered in T2K analyses. The effects are indirectly considered by applying a large prior uncertainty on parameters which affect the CCQE cross section in the near-detector data fit. This is justified because npnh events are likely to produce a very similar signal to CCQE events in the T2K detectors. This effectively allows npnh events to be mistaken for CCQE with little bias to the total normalisation.

Mistakenly identifying an npnh interaction as CCQE does result in a bias when reconstructing the neutrino energy from the final-state lepton, since on average more energy than expected is transferred to the hadronic system (compared to a CCQE interaction with the same muon energy). Figure 6.1 shows the neutrino energy reconstructed from the muon kinematics for CCQE and for npnh events assuming the target was a single stationary nucleon.

The measurements of neutrino oscillation parameters are largely determined by the difference between the expected and the reconstructed neutrino flux at the far detector, so a bias in the reconstructed energy can bias the determination of the values of these parameters. In the study described in Reference [77], the size of this bias on θ_{23} in

the disappearance analysis was estimated, and was found to be negligible compared to the current statistical and systematic errors. However, as the uncertainties reduce it is important to include the affects of npnh interactions in the oscillation analyses before the potential bias becomes non-negligible.

The multinucleon neutrino model which was selected for implementation into NEUT was that of Nieves *et al.* [42]. Code was made available to T2K which provided a calculation of the predicted double-differential cross-section for the npnh part of the model (the full model included other interaction modes). The required inputs are the neutrino energy and flavour, the target nucleus, and specific muon kinematics. Kinematics of the final-state hadrons are not predicted by the model, and not provided by the code.

This section describes the use of this code to implement an interaction mode representative of the Nieves multinucleon neutrino model into NEUT.

6.2. An implementation into NEUT of the multinucleon neutrino interaction model of Nieves et al.

In order to include the affects of npnh into the T2K analyses, it is necessary to implement this mode into the main T2K neutrino interaction generator, NEUT. This will enable simulation of npnh events in the detectors, so that the distribution of these interactions amongst the near-detector data samples can be studied and the energy reconstruction corrected. For this task it is necessary to simulate these events with a realistic total cross section, as well as realistic kinematics for all final-state particles.

The multinucleon neutrino interaction mode of Nieves *et al.* was implemented into NEUT, using NEUT 5.1.4.5 as a base version. The mode was implemented using pre-calculated look-up tables. Tables of the muon double-differential cross section in terms of T_μ and $\cos\theta_\mu$ were produced using code provided by the authors of the model. The double-differential cross sections were integrated to obtain the total cross section, which was also stored in a table. For each NEUT event, the mode is chosen from the branching fraction of all modes given the neutrino energy. For each simulated multinucleon neutrino event, the muon kinematics were chosen from the double-differential cross section tables.

The nucleon kinematics are not simulated in the actual multinucleon neutrino interaction model, so a separate model to simulate the nucleon kinematics was implemented.

Before discussing the implementation, this section begins with a discussion of a modification to the multinucleon neutrino model of Nieves *et al.* from Reference [55] which allows the model to be extended to high energy. This modification significantly affects the implementation so must be discussed before the implementation itself. Next, the full implementation is described, with separate discussions of the total cross section, double-differential muon cross section, and simulation of the final-state nucleons. Validation studies are shown for a number of parts of the implementation. For clarity, validation studies are shown separately from the description of the implementation and reference is made to the relevant validation study for each part of the implementation.

6.2.1. Extension of Nieves model to high energy

The cross section prediction of Nieves [42] is limited to a maximum neutrino energy of $E_\nu = 1.5$ GeV due to unmodelled channels which are expected to contribute to the total cross section. However, it can be extended to higher energy by limiting the 3-momentum transfer of the interaction as in [55] and as described in Section 3.3.2.

The 3-momentum transfer of an interaction is defined as

$$\vec{q} = \vec{p}_\mu - \vec{p}_\nu, \tag{6.1}$$

where $\vec{p}_\mu$ is the 3-momentum of the final state lepton, and $\vec{p}_\nu$ is the 3-momentum of the neutrino. The magnitude of $\vec{q}$ can also be expressed as

$$|\vec{q}| = \sqrt{|\vec{p}_\mu|^2 + E_\nu^2 - 2|\vec{p}_\mu| E_\nu \cos\theta_\mu}, \tag{6.2}$$

where $\cos\theta_\mu$ is the opening angle between the initial and final state leptons and E_ν is the neutrino energy. Imposing a limit on the three-momentum transfer means a maximum value of the above quantity. The limit is denoted hereafter as α. The limit suggested by the authors of [55] is $\alpha = 1.2$ GeV. Above this point there would be significant contribution from additional unmodelled processes to the multinucleon neutrino cross section. Additionally, numerical inaccuracy of the code meant increasingly unacceptable numerical errors at higher α.

Limiting the 3-momentum transfer limits the possible final-state lepton kinematic space. From Equation 6.2 it can be shown that the minimum lepton kinetic energy (when $\cos\theta_\mu = 1$) is

$$T_\mu \geq \sqrt{m_\mu^2 + (E_\nu - \alpha)^2} - m_\mu, \tag{6.3}$$

where m_μ is the mass of the final-state lepton. From Equation 6.2 it can also be shown that the maximum possible opening angle given the maximum 3-momentum transfer α is

$$\cos\theta_\mu \geq \sqrt{1 - \left(\frac{\alpha}{E_\nu}\right)^2}. \tag{6.4}$$

This limit is valid only for $\alpha \leq E_\nu$, otherwise there is no limit on $\cos\theta_\mu$ (other than the physical limit).

These limits inform the parameter ranges over which the cross section tables must be produced.

6.2.2. Production of look-up tables for the Nieves multinucleon neutrino model

It was necessary to choose ranges for the neutrino energy, muon opening angle and muon kinetic energy in which to produce the look-up tables. The range for the neutrino energy was informed by the T2K flux: the cross section needed to cover the range of neutrino energies present in the beam. This was chosen to be up to 30 GeV.

The range for $\cos\theta_\mu$ was set by the 3-momentum cut, and is expressed in Equation 6.4. There is also the physical limit that $-1 \leq \cos\theta_\mu \leq 1$. The limit from Equation 6.4 only applies when $\alpha \leq E_\nu$.

The lower limit for T_μ was also set by the 3-momentum cut and is expressed in Equation 6.3. This expression can be negative, in which case there is the physical limit of $T_\mu \geq 0$. The upper limit for T_μ is set by energy conservation as

$$T_\mu \leq E_\nu - m_\mu - a \tag{6.5}$$

where a is scalar quantity used in the cross section code to account for the energy of nuclear excitation. There is one value of a for each nucleus.

The number of points in the cross section tables was chosen to balance the amount of detail required to see all relevant features and the time taken to generate the tables. Each point takes several minutes to generate using the version of the code that was available. A study was performed to choose the number of points in each variable, and is described in Section 6.3.1. This study found that acceptable numbers of points to be 92 points in energy, 31 points in T_μ, and 31 points in $\cos\theta_\mu$.

The distribution of points within the allowed ranges was decided by a balance between optimisation for higher point density in areas of rapid change, and the complication of the look-up algorithm. The main features of the cross section were found to vary fastest towards higher T_μ and higher $\cos\theta_\mu$ (though not necessarily at the extrema), so a point distribution with an increasing point density with increasing T_μ and $\cos\theta_\mu$ was chosen. The point density functions were defined to yield an exponentially increasing density with increasing T_μ and $\cos\theta_\mu$, with a specified ratio of point densities between the minimum and maximum parameter ranges. These ratios were optimised in the study described in Section 6.3.1, and chosen to be 25 for $\cos\theta_\mu$ and 10 for T_μ. The function used to define the points in $\cos\theta_\mu$ was

$$\cos\theta_i = \left(\frac{1-\cos\theta_{\min}}{k_\theta}\right)\ln\left[\frac{i(e^{k_\theta}-1)}{N_\theta-1}+1\right]+\cos\theta_{\min} \tag{6.6}$$

where e^{k_θ} is the ratio of the point density at the end to that at the start, N_θ is the number of datapoints in $\cos\theta_\mu$, i is an integer from zero to $N_\theta-1$ inclusive, and $\cos\theta_{\min}$ is

$$\cos\theta_{\min} = \begin{cases} \sqrt{1-\left(\dfrac{\alpha}{E_\nu}\right)^2} & \text{if } E_\nu \geq \alpha, \\ -1 & \text{otherwise.} \end{cases} \tag{6.7}$$

Similarly the function used to define the points in T_μ was

$$T_{\mu i} = \left(\frac{E_\nu - m_l - a - T_{\min}}{k_T}\right)\ln\left[\frac{i(e^{k_T}-1)}{N_T-1}+1\right]+T_{\min} \tag{6.8}$$

where e^{k_T} is the ratio of the point density at the end to that at the start, N_T is the number of datapoints in T_μ, i is an integer from zero to $N_T - 1$ inclusive, a is

$$a = \begin{cases} 16.827 \text{ MeV} & \nu \text{ on } \mathrm{C}^{12} \\ 13.880 \text{ MeV} & \overline{\nu} \text{ on } \mathrm{C}^{12} \\ 14.906 \text{ MeV} & \nu \text{ on } \mathrm{O}^{16} \\ 10.931 \text{ MeV} & \overline{\nu} \text{ on } \mathrm{O}^{16} \end{cases} \tag{6.9}$$

and T_{min} is

$$T_{\text{min}} = \begin{cases} \sqrt{m_l^2 + (E_\nu - \alpha)^2} - m_l & \text{if } E_\nu \geq \alpha \\ 0 & \text{otherwise.} \end{cases} \tag{6.10}$$

The points themselves were produced with a value of $\alpha = 1.5$, which yields a wider range of final-state lepton kinematics to allow for an expansion of the kinematic space if required in the future.

The values of E_ν at which datapoints were produced was chosen by hand, taking into account the required accuracy of interpolation between the different values, the time taken to produce the set of tables, and the behaviour of the $\cos\theta_\mu$ and T_μ point functions. A study of the accuracy of the interpolation between cross section grids was performed, and is described in Section 6.3.2. The energy points at which the cross section is evaluated were chosen to be

$$
\begin{aligned}
E_\nu(\text{GeV}) = \{&0.1000, \quad 0.1025, \; 0.1050, \; 0.1075, \; 0.1100, \; 0.1125, \; 0.1150,\\
&0.1175, \quad 0.1200, \; 0.1225, \; 0.1250, \; 0.1275, \; 0.1300, \; 0.1325,\\
&0.1350, \quad 0.1375, \; 0.1400, \; 0.1425, \; 0.1450, \; 0.1475, \; 0.1500,\\
&0.1525, \quad 0.1550, \; 0.1575, \; 0.1600, \; 0.1625, \; 0.1650, \; 0.1700,\\
&0.1750, \quad 0.1800, \; 0.1850, \; 0.1900, \; 0.2000, \; 0.2050, \; 0.2100,\\
&0.2200, \quad 0.2300, \; 0.2400, \; 0.2500, \; 0.2600, \; 0.2750, \; 0.3000,\\
&0.3250, \quad 0.3500, \; 0.3750, \; 0.4000, \; 0.4250, \; 0.4500, \; 0.4750,\\
&0.5000, \quad 0.5250, \; 0.5500, \; 0.6000, \; 0.6500, \; 0.7000, \; 0.7500,\\
&0.8000, \quad 0.8500, \; 0.9000, \; 0.9500, \; 1.0000, \; 1.0500, \; 1.1000,\\
&1.1500, \quad 1.2000, \; 1.2500, \; 1.3000, \; 1.4000, \; 1.4900, \; 1.4999999,\\
&1.5000001, \; 1.5020, \; 1.5075, \; 1.5130, \; 1.5150, \; 1.5200, \; 1.5250,\\
&1.5500, \quad 1.5750, \; 1.6000, \; 1.6500, \; 1.8000, \; 1.9000, \; 2.0000,\\
&2.5000, \quad 3.0000, \; 4.0000, \; 6.0000, \; 7.5000, \; 10.000, \; 20.000,\\
&30.000 \}.
\end{aligned}
$$

The choice for these values, including the two values close to $E_\nu = 1.5$ GeV is explained in Section 6.3.2. Double-differential cross section tables are shown for three neutrino energies in Figures 6.2 and 6.3. Figure 6.2 shows the three cross sections with the same $\cos\theta_\mu$ and T_μ scale to illustrate how the allowed phase-space scales with neutrino energy. Figure 6.3 shows the three cross sections with the axes scaled such that the axis minima are $\cos\theta_{\text{min}}$ and T_{min} from Equations 6.7 and 6.10 respectively. This is done to illustrate the shape of the cross section within the populated region, which is fairly stable over a wide range of neutrino energy.

6.2.3. Throwing multinucleon neutrino events in NEUT

Using the double-differential cross section tables, the total cross section as a function of neutrino energy was calculated. This was performed by Asmita Redij of the University of Bern. The tables were integrated using a bilinear method (i.e. generalisation of linear integration to 2D). The integral for each 2D T_μ-$\cos\theta_\mu$ grid was calculated and the information was saved as a text file. The total cross section was produced separately for each target and neutrino flavour. The part of the double-differential cross section which

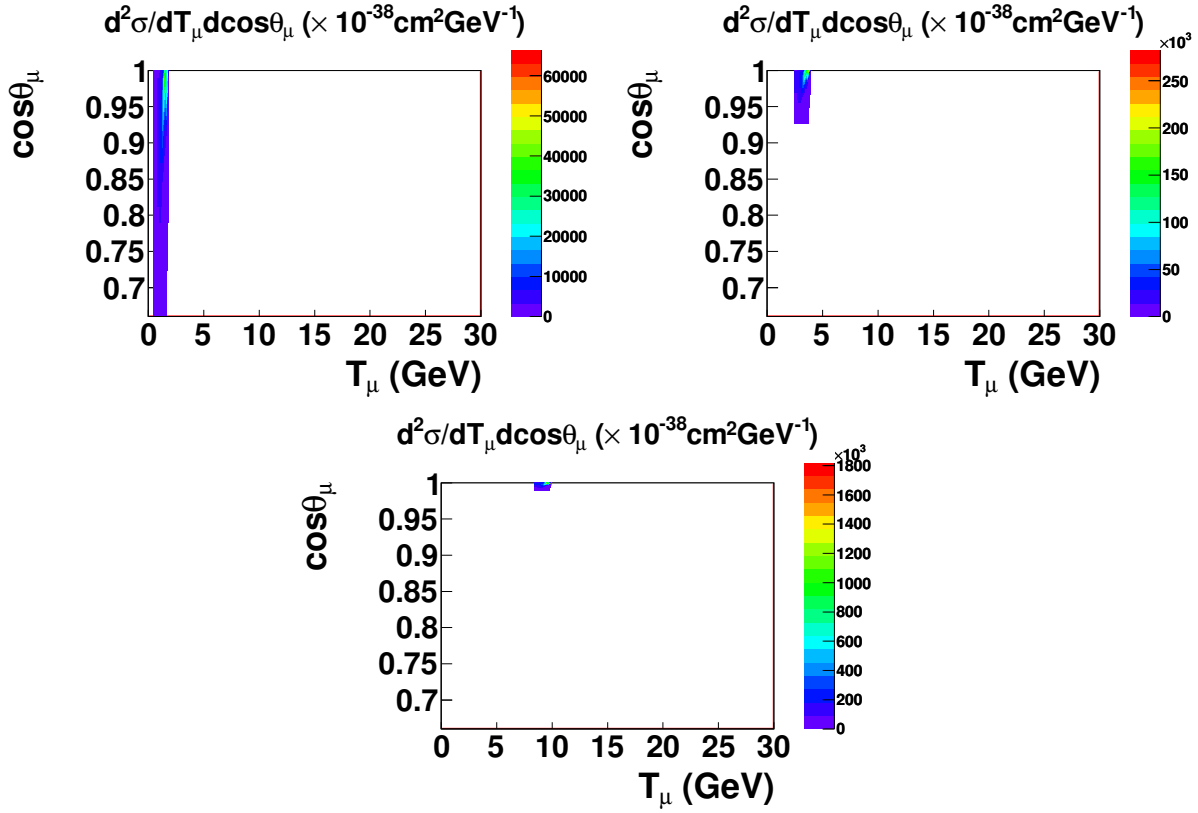

Figure 6.2.: Double-differential cross section of multinucleon neutrino interactions for ν_μ on C^{12}. Evaluated at $E_\nu = 2$ GeV (top left), $E_\nu = 4$ GeV (top right), $E_\nu = 10$ GeV (bottom). All are shown with the same $\cos\theta_\mu$ and T_μ axes. Cross section evaluated at bin corners then linearly interpolated to bin centers.

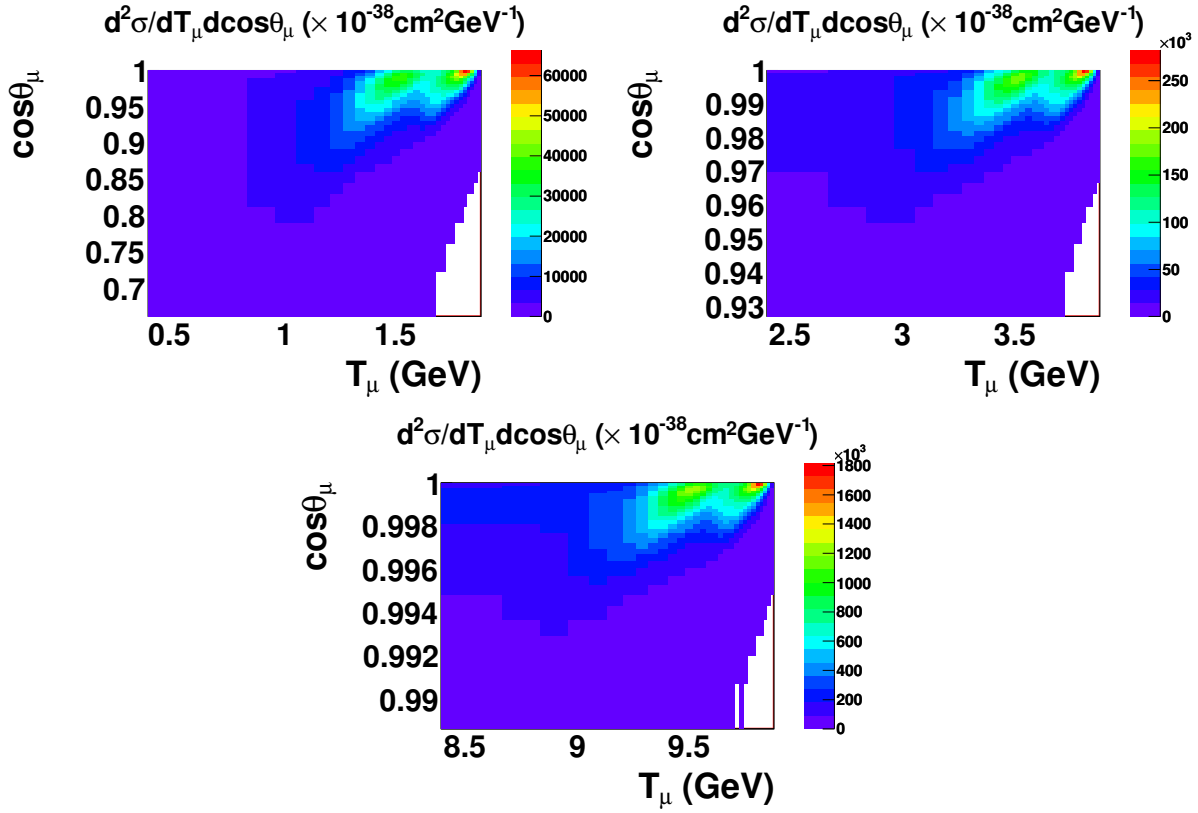

Figure 6.3.: Double-differential cross section of multinucleon neutrino interactions for ν_μ on C^{12}. Evaluated at $E_\nu = 2$ GeV (top left), $E_\nu = 4$ GeV (top right), $E_\nu = 10$ GeV (bottom). $\cos\theta_\mu$ and T_μ axes scaled such that the axis minima are $\cos\theta_{\text{min}}$ and T_{min} from Equations 6.7 and 6.10 respectively. Cross section evaluated at bin corners then linearly interpolated to bin centers.

contributed to the total cross section was only that with a 3-momentum transfer less than the threshold, so the integral was performed only within this region.

Figures 6.4 and 6.5 show the effect of the 3-momentum cut on the differential cross section for different neutrino energies. Figures 6.4b and 6.5b show the fraction of each bin included in the total cross section calculation. Figures 6.6 and 6.7 show the cross sections of the four relevant neutrino flavours on C^{12} and O^{16} targets respectively. The energy threshold for ν_e npnh interactions is smaller than that of ν_μ due to the larger muon mass. This is also manifest in a smaller ν_μ cross section at low E_ν. The cross section for ν is greater than that for $\overline{\nu}$ up to high energy due to a change of sign of one of the terms in the fundamental cross section between ν and $\overline{\nu}$, causing destructive interference in the $\overline{\nu}$ case. Figures 6.8 and 6.9 show the cross section of the multinucleon neutrino process with ν_μ on C^{12}, compared to the CCQE and total CC cross section in NEUT for the same neutrino flavour and target.

The multinucleon neutrino cross section was included into NEUT 5.1.4.5 in the same way as the other NEUT interaction modes. The integration of the npnh code into NEUT was done by Asmita Redij. Section 6.3.3 describes a study to validate the successful inclusion of this mode into NEUT. The study shows that the total cross section from the tables can be reconstructed from the distribution of multinucleon neutrino events in a NEUT MC ROOT file. Figure 6.10 shows the internal NEUT cross sections for the multinucleon neutrino mode compared to that reconstructed from the distributions of muons in a sample of NEUT MC. The NEUT MC cross section is consistent with the internal cross section.

6.2.4. Implementation of double-differential muon cross section given neutrino energy

In the NEUT event simulation, the neutrino energy is the first quantity chosen based on the total cross section and the input flux. Next, the interaction mode is chosen based on the branching fractions of each mode. If a multinucleon neutrino interaction is chosen, the muon kinematics are then chosen from the double-differential cross section tables. The general procedure is to obtain a table for the muon kinematics at the precise neutrino energy which was selected, then to use this as a probability density function to select the T_μ and $\cos\theta_\mu$ of the muon.

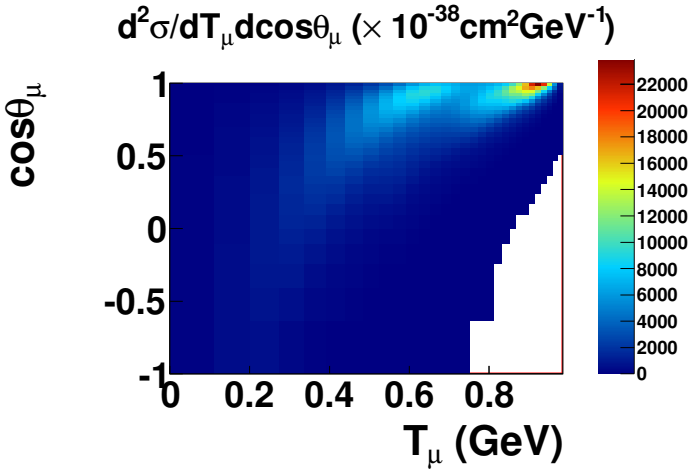

(a) Double-differential cross section without cut

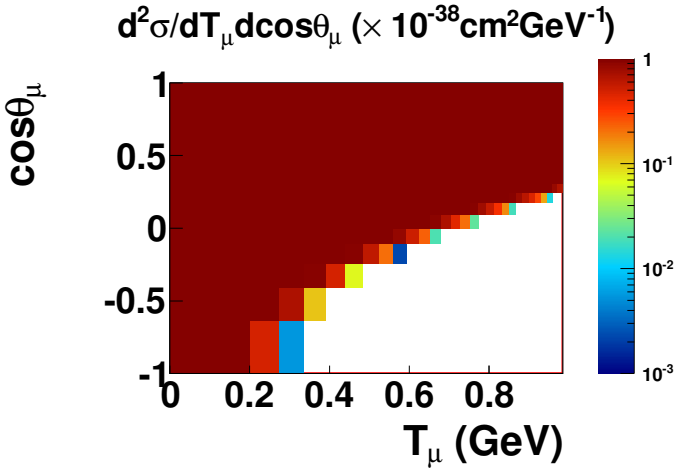

(b) Fraction of each bin within 3-momentum cut

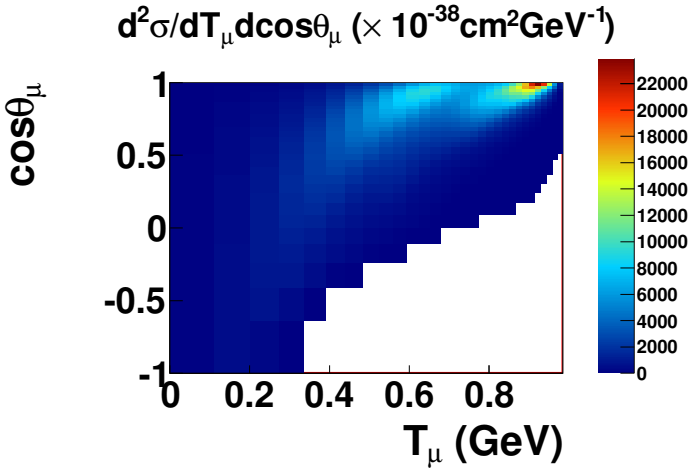

(c) Double-differential cross section after cut

Figure 6.4.: Double-differential cross section for multinucleon neutrino interaction of a 1 GeV ν_μ on C^{12}, showing effect of 3-momentum cut on double-differential cross section. A value of $\alpha = 1.2$GeV is used for the cut.

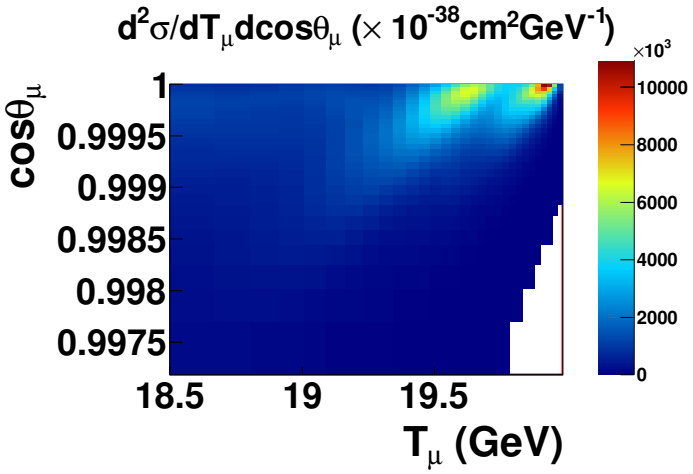

(a) Double-differential cross section without cut

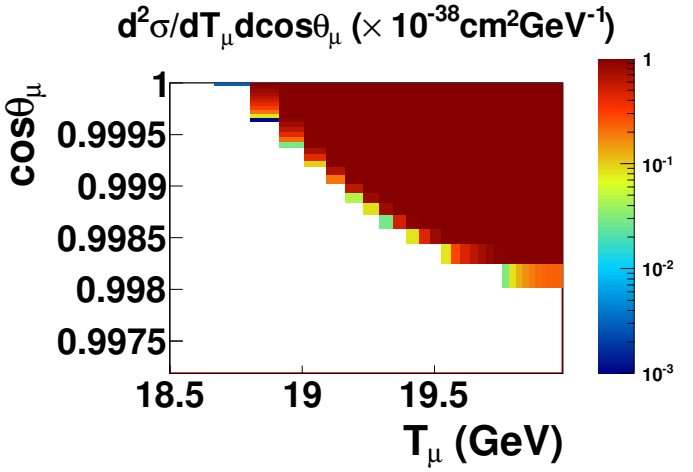

(b) Fraction of each bin within 3-momentum cut

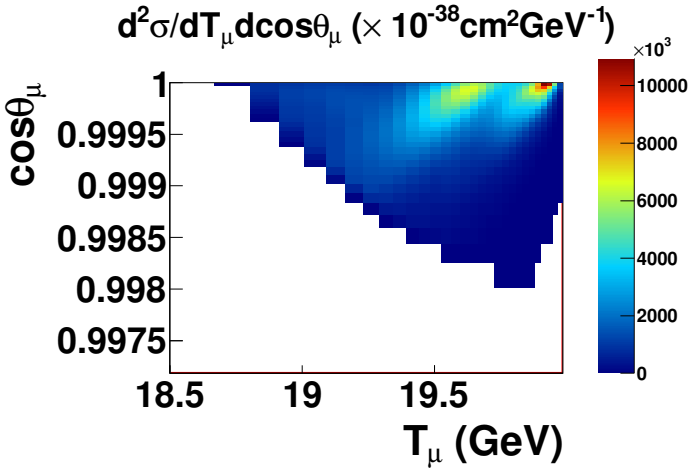

(c) Double-differential cross section after cut

Figure 6.5.: Double-differential cross section for multinucleon neutrino interaction of a 2 GeV ν_μ on C^{12}, showing effect of 3-momentum cut on double-differential cross section. A value of $\alpha = 1.2$GeV is used for the cut.

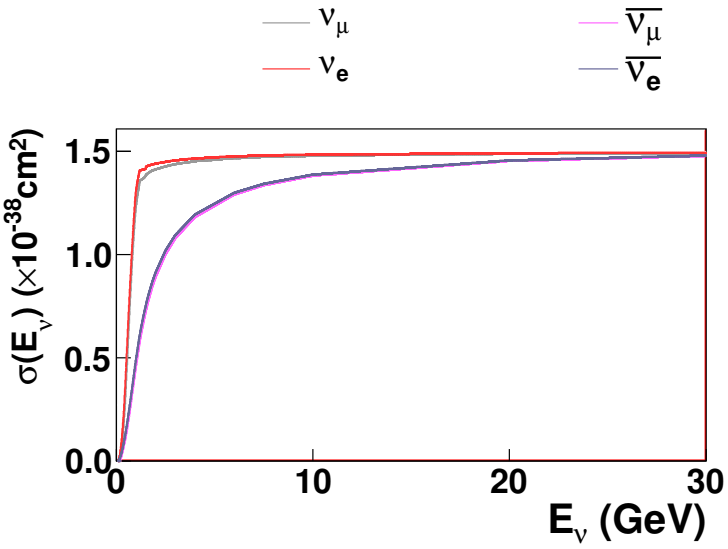

Figure 6.6.: Total cross section for multinucleon neutrino mode with the Nieves model on C^{12} target.

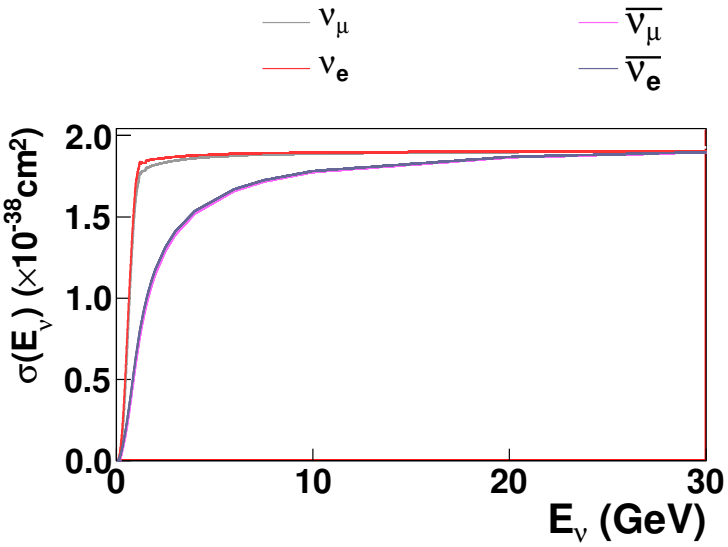

Figure 6.7.: Total cross section for multinucleon neutrino mode with the Nieves model on O^{16} target.

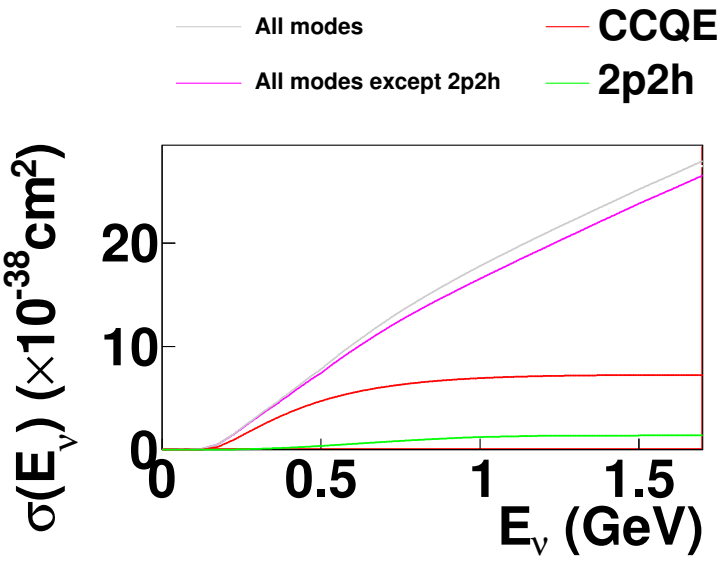

Figure 6.8.: Total cross section for multinucleon neutrino mode compared to the CCQE and total CC (with and without multinucleon neutrino) for ν_μ on C^{12}. Plot shows cross sections for neutrino energies up to 1.5 GeV.

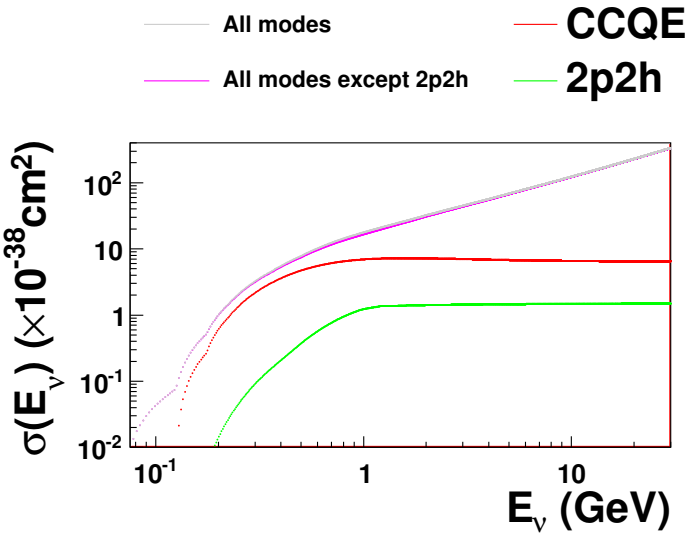

Figure 6.9.: Total cross section for multinucleon neutrino mode compared to the CCQE and total CC (with and without multinucleon neutrino) for ν_μ on C^{12}. Plot shows cross sections for neutrino energies up to 30 GeV.

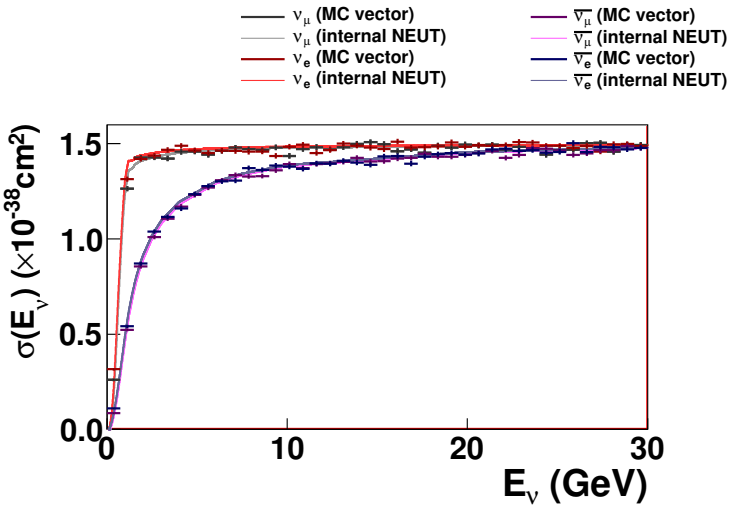

Figure 6.10.: Total cross section for multinucleon neutrino mode with the Nieves model on C^{12} target compared to cross section reconstruction from final NEUT root file.

The method begins by selecting the two tables nearest in neutrino energy to that which was chosen. The chosen neutrino energy is denoted E_ν, the energy of the table evaluated at the next-lowest neutrino energy is $E_<$, and the energy of the table evaluated at the next-highest neutrino energy is $E_>$. The muon double differential cross section tables evaluated at $E_<$ and $E_>$ are used to obtain an estimate of the table which would be evaluated at E_ν.

The most simple way to do this would be to interpolate between points at constant values of T_μ and $\cos\theta_\mu$, however the points at which the cross section is evaluated are distributed according to Equations 6.6 and 6.8, which are not constant in neutrino energy, and which may populate very different areas of the muon phase space. A more robust method is motivated by inspecting Figure 6.3. These 'scaled' plots show that the shape of the differential cross sections are very similar even at very different neutrino energies. Based on this, the method chosen was to interpolate between the points of these scaled grids. In practice, this meant interpolating between points with the same indices in Equations 6.6 and 6.8 (e.g. an interpolation would be done between the n^{th} T_μ point in the $E_<$ and $E_>$ grids to obtain the n^{th} T_μ point in the E_ν grid). A study was performed to investigate the integrity of this method, and it was found to be sufficiently accurate given the energy binning described in Section 6.2.2. This study is described in detail in Section 6.3.2.

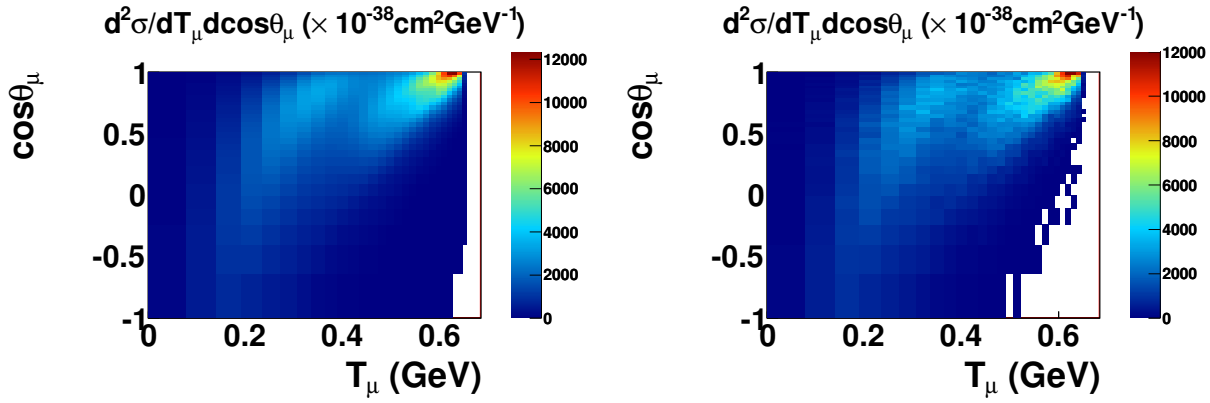

Figure 6.11.: Muon double-differential cross section for 700 MeV ν_μ on C^{12} calculated using Nieves' code (top) compared to the muon kinematic distribution from 1×10^5 NEUT multinucleon neutrino events of the same neutrino energy (middle), neutrino flavour and target.

Using this interpolation method, the muon double-differential cross section at E_ν is calculated. This is then used as a probability density function to choose the lepton kinematics using an accept-reject method. First, the maximum point in the double-differential cross section is found. Next, random values of T_μ and $\cos\theta_\mu$ are chosen within the populated phase-space. A random number is drawn between zero and the double-differential cross section maximum. If the random number is greater than the value of the double-differential at the chosen T_μ and $\cos\theta_\mu$, the point is rejected and new random T_μ and $\cos\theta_\mu$ are chosen. If the random number is less than the value of the double-differential at T_μ and $\cos\theta_\mu$, the point is accepted. To specify the full lab-frame muon kinematics, the muon is then given a random rotation around the axis defined by the neutrino direction.

Figure 6.11 shows a comparison of the muon double-differential cross section calculated from Nieves' code to a histogram of the same muon kinematics obtained from events which were simulated in NEUT using the method as described. The two appear consistent within the statistics of the MC sample. A study was performed to confirm that the muon kinematics from the NEUT simulation were statistically consistent with the muon double-differential cross section tables for a range of neutrino energies, as described in Section 6.3.4.

6.2.5. Nucleon kinematics

The theoretical model used to predict the total and double-differential cross sections for the multinucleon neutrino mode does not predict the distribution of the initial or final state nucleons. The model calculation does employ a well defined nuclear model, but the lepton cross section is provided integrated over all hadronic degrees of freedom. For inclusion into T2K analyses, we require a simulation of the full event including all final-state nucleons since these may affect how the events are reconstructed in the detectors, and which event sample multinucleon neutrino events are included into.

A generic method for simulating hadron kinematics in a multinucleon neutrino interaction is described in the model of Sobczyk [78]. The philosophy of the method is to use minimal assumptions to constrain the possible hadron kinematics. The underlying assumptions are:

1. Energy and momentum conservation
2. Initial-state hadrons have same nuclear model as those in 1p1h interactions
3. Initial-state nucleon momenta are not correlated
4. Momentum shared equally between final-state nucleons in the center-of-mass frame of the final-state hadronic system

The method described in [78] is employed, with small modifications, to choose the initial and final-state nucleon momenta and directions in the implementation of multinucleon neutrino into NEUT. It is implemented as follows:

1. In the lab frame, choose the neutrino energy and muon kinematics. This defines the 4-momentum transfer to the hadronic system.
2. Use Woods-Saxon nuclear density function [79] to choose the interaction position within the nucleus according to the square of the nuclear density (this step is not in the method of [78]).
3. For initial state nucleons, loop over the possible 4-momenta until a viable combination is found (one such that the total energy in the hadronic system will allow two real final-state nucleons to exist outside of the nuclear potential).
4. Boost to the center-of-mass frame of the hadronic system.
5. Divide the available energy between two nucleons.

6. Set the axis of the nucleon momenta in the center-of-mass frame to a random direction.
7. Boost all particles back into lab frame.
8. Check if either nucleon is Pauli-blocked (i.e. momentum less than the Fermi-surface momentum). If either nucleon is Pauli-blocked, re-sample nucleon momenta and iterate (this step is not in the original method).

As a result of the requirements on the hadronic system, the leptonic double-differential cross section is changed slightly from that predicted in the theory. This happens because the nuclear model used in NEUT and that used in the multinucleon neutrino code have small differences. The effect is from the requirement that both nucleons be given sufficient energy to escape the nuclear potential. This lowers the maximum muon kinetic energy from $T_\mu = E_\nu - m_l - a$ to $T_\mu = E_\nu - m_l - a - 2E_b$ where E_b is the binding energy of a single nucleon. It is assumed that the binding energy for two nucleons is twice that for a single nucleon. The fraction of events thrown with $E_\nu - m_l - a < T_\mu < E_\nu - m_l - a - 2E_b$ is approximately 2% at $E_\nu = 400$ MeV, reducing to 0.3% at $E_\nu = 1.5$ GeV. A smaller difference comes from the requirement that both final-state nucleons must be on-shell, which forbids some regions of muon-phase space with small energy transfer and large momentum-transfer (corresponding to high T_μ and high $\cos\theta_\mu$). This affects approximately 0.03% of events, and is roughly constant with energy. The muon kinematics are re-thrown for these events, so the total normalisation does not change.

The two nucleons ejected are designated as *primary* and *spectator*. The primary nucleon is defined as that which changes isospin in the interaction. The initial isospin of the primary nucleon is set by the CP state of the incoming neutrino to ensure charge conservation; if the incoming particle is a neutrino (antineutrino), the primary nucleon is a neutron (proton). In the NEUT implementation, the isospin of the spectator nucleon is thrown from a fixed probability for each target, considering the multiplicity of nn, np and pp pairs in the initial state. There is thus a correlation between the isospin of the nucleons.

Some of the final-state interaction subroutines in NEUT were changed to accommodate the nuclear model employed in the multinucleon neutrino simulation. The multinucleon neutrino code in NEUT uses the local Fermi-gas model for the nuclear density, whereas the global Fermi-gas is assumed in the FSI routines. To be consistent throughout the simulation, the FSI routines were modified to take the nucleon momentum distributions

from the local Fermi-gas for multinucleon neutrino interactions. This was implemented by Asmita Redij of the University of Bern. Aside from this modification, nucleons from the multinucleon neutrino simulation are propagated through the same FSI routines as those from all other interactions.

Section 6.4 describes a study of the implementation of the hadronic part of the multinucleon neutrino simulation. It is confirmed that energy and momentum are properly conserved, and some basic kinematic plots are shown to ensure that distributions do not exhibit any obvious pathologies.

6.2.6. Future improvements

There are a number ways in which the present implementation could be improved.

One possible improvement is the simulation of multinucleon neutrino interactions on additional elements. The simulation described here includes simulation only on C^{12} and O^{16}. As of writing, the latest tagged version includes simulation on Ca^{40} in the same way as C^{12} and O^{16} (i.e. production of a cross section table), as well as a simple linear interpolation of the total and differential cross sections to intermediate elements. This could be improved by calculation of additional cross section tables at intermediate nucleon number, however the code itself can only be used to calculate the cross section on isoscalar nuclei.

An additional improvement can be made to the simulation of the spectator nucleon isospin. In more recent versions of the cross section calculation code, it is possible to extract the predicted fraction of nn, pp and np initial states from the model, which has a dependance on the kinematics of the interaction. This was not implemented into the NEUT simulation at the time of writing, and would be a simple but important upgrade to the simulation. This improvement would remove the need for a systematic on proton multiplicity from multinucleon neutrino interactions.

Simulation of the final state hadrons in multinucleon neutrino interactions could also be improved. The current model assumes the momentum available to the final state nucleons is split equally, however it is likely that there should be a penalty paid for transferring momentum through the pion propagator, making the momentum distribution asymmetric. The precise form of the asymmetry is not obvious, and would have to be carefully formulated. Additionally, the implementation of Pauli-blocking for final-state nucleons strongly affects their kinematics, so should be implemented carefully with

reference to a robust prediction from theory, or else furnished with an appropriately large systematic error.

Finally, the simulation of the nuclear environment could be improved. The current assumption that the binding energy of two nucleons is twice that of a single nucleon is an oversimplification which could possibly be improved with input from data or from a more detailed calculation from theory. The binding energy referred to here is the energy taken to remove a single nucleon from the nucleus: once a single nucleon is removed, the energy taken to remove the second nucleon is the energy of removal of a single nucleon from a different nucleus. Additionally, the current implementation does not take into account possible binding between the two ejected nucleons.

6.3. Validation of leptonic simulation

This section describes the various studies which were performed to optimise and validate the implementation of the multinucleon neutrino mode into NEUT. An optimisation study was performed to choose the number and distribution of points in the cross section tables, and studies were performed to validate the total and differential cross sections.

6.3.1. Optimisation of point number and point distributions of T_μ and $\cos\theta_\mu$ in double-differential cross section tables

The distribution of the points at which the cross section is evaluated must be such that all real structure is mapped with sufficient detail. Further, the binning must be fine enough that the chosen interpolation method, in this case linear interpolation, is a good approximation of the true form of the cross section. Point densities are limited by the computational time taken to generate the points, which is on the order of a few minutes per point.

The point densities for T_μ and $\cos\theta_\mu$ were optimised using a simple by-eye study. A point distribution was chosen for T_μ and $\cos\theta_\mu$, with the initial spacing informed by knowledge of the approximate size of the resonances simulated in the multinucleon neutrino code. Cross section tables were produced for a number of neutrino energies and the grids were inspected. Missing information was identified by the presence of large spikes when looking at 1D slices through the 2D cross section tables. After inspection of

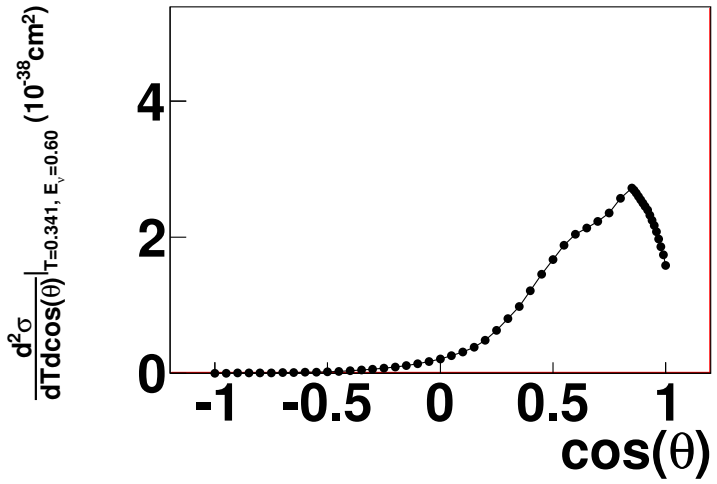

Figure 6.12.: Muon double-differential cross section as a function of $\cos\theta_\mu$ for $E_\nu = 0.60$ GeV and $T_\mu = 0.341$ GeV. Cross section is for ν_μ on C^{12}. Cross section calculated at 53 equally spaced points in $\cos\theta_\mu$.

the 1D slices, the point density was changed, and the process was iterated until acceptable point distributions for T_μ and $\cos\theta_\mu$ were obtained.

The first guess was to use an equally spaced grid of 31 T_μ points between zero and $E_\nu - m_l$, and 53 $\cos\theta_\mu$ points between -1 and $+1$. Figures 6.12 and 6.13 show typical examples of the plots for ν_μ on C^{12}. Figure 6.12 shows the double-differential cross section at $E_\nu = 0.60$ GeV and $T_\mu = 0.341$ GeV, as a function of $\cos\theta_\mu$.

A number of point density distributions were inspected, and after several iterations it was decided to generate points with an exponentially increasing point density as a function of T_μ and $\cos\theta_\mu$, and with 31 points in each variable.

Equations were formulated which take as arguments the neutrino energy and the point index and yield a value of T_μ or $\cos\theta_\mu$ with an exponentially increasing point density. These are stated in Equations 6.8 and 6.6 for T_μ and $\cos\theta_\mu$ respectively. They are tunable by a single parameter, defining the ratio of the point densities at the position of the first to the last point index. Density ratios of 10 for T_μ and 25 for $\cos\theta_\mu$ were found to be sufficient. Typical 1D-slice plots for the final parameter choices are shown in Figures 6.14 and 6.15.

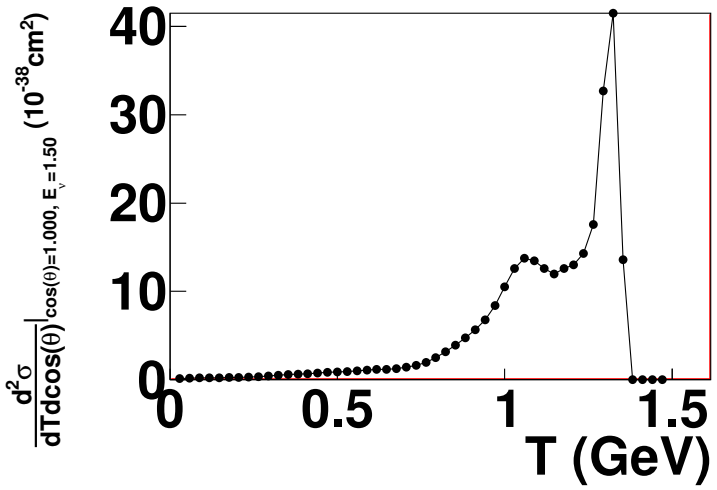

Figure 6.13.: Muon double-differential cross section as a function of T_μ for $E_\nu = 1.50$ GeV and cos = 1.0. Cross section is for ν_μ on C^{12}. Cross section calculated at 31 equally spaced points in T_μ.

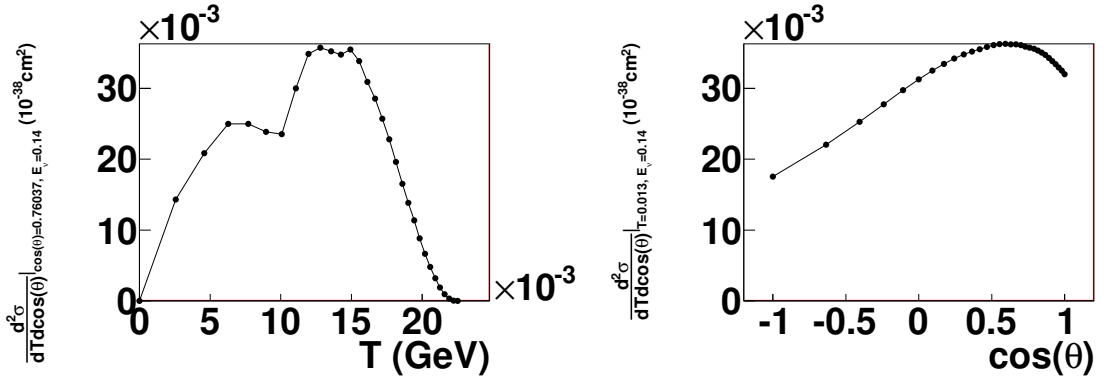

(a) As a function of T_μ for cos = 0.76. **(b)** As a function of $\cos\theta_\mu$ for $T_\mu = 12.8$ MeV.

Figure 6.14.: Muon double-differential cross section as a function of T_μ and $\cos\theta_\mu$ with $E_\nu = 0.14$ GeV. Cross section is for ν_μ on C^{12}. Cross section calculated at 31 points in both T_μ and $\cos\theta_\mu$ according to the Equations 6.8 and 6.6.

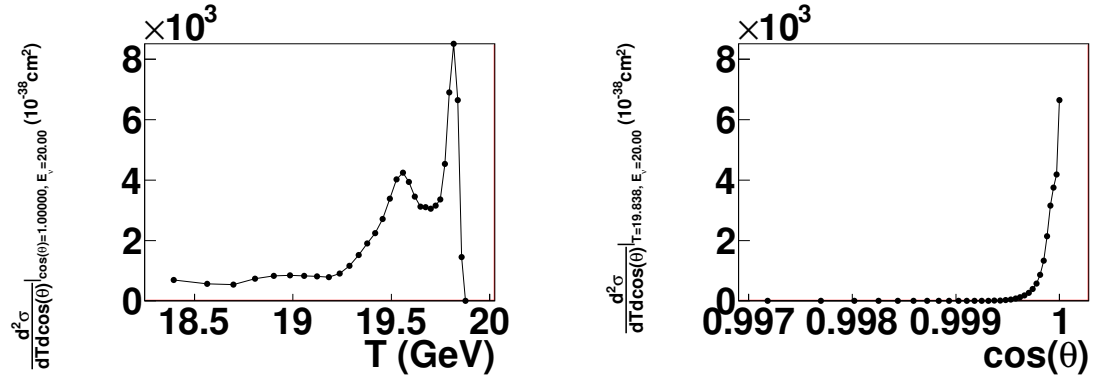

(a) As a function of T_μ for cos = 1.0. **(b)** As a function of $\cos\theta_\mu$ for $T_\mu = 19.8$ GeV.

Figure 6.15.: Muon double-differential cross section as a function of T_μ and $\cos\theta_\mu$ with $E_\nu = 20$ GeV. Cross section is for ν_μ on C^{12}. Cross section calculated at 31 points in both T_μ and $\cos\theta_\mu$ according to the Equations 6.8 and 6.6.

6.3.2. Study of energy interpolation method for double-differential cross section

The multinucleon neutrino simulation implemented in NEUT requires interpolation of differential cross section grids to obtain an estimate of the predicted differential cross section for a specific neutrino energy. The method employed is for the cross section to be interpolated between T_μ and $\cos\theta_\mu$ points with the same bin index in Equations 6.8 and 6.6 (as opposed to interpolation between points of constant T_μ and $\cos\theta_\mu$).

The purpose of the study described in this section was to confirm the accuracy of this method. More precisely, it is to compare the double-differential cross section produced with the interpolation method to that created using Nieves' multinucleon neutrino code, and to ensure that the difference between the two was sufficiently small such that the interpolation error could be neglected.

The study was performed as follows:

1. For a number of fixed E_ν, the multinucleon neutrino cross section was evaluated at all points in T_μ and $\cos\theta_\mu$ in Equations 6.8 and 6.6. The neutrino energies at which the tables are produced are labelled E_1, $E_2 \ldots$

2. The differential cross section was interpolated to E_{n+1} using the tables at E_n and E_{n+2} for all possible n.

3. For each n, the fractional difference in each bin between the interpolated and evaluated cross section grids was plotted.

4. The size of the fractional differences was inspected. When the fractional differences were too large, the energy point density in that region was increased and the study reperformed.

Note that this study shows the fractional difference if the spacing between the points was double that in the set of cross section grids (since the interpolation is between grids at E_n and E_{n+2}).

Figure 6.16 shows an example of this comparison for one neutrino energy. Figures 6.16a and 6.16b show the high and low cross section grids used as inputs into the interpolation. Figure 6.16c shows the cross section grid evaluated at the chosen energy, and Figure 6.16d shows the cross section grid obtained using the interpolation method. They appear very similar by-eye. Figure 6.16e shows a map of the fractional difference between the evaluated and interpolated cross sections. Although there are some areas with a large ($> 10\%$) fractional difference, these are confined to areas where the cross section is small. The fractional difference is a few-% in areas of appreciable cross section, and sub-% in the region of the peak. Figure 6.17 shows three maps of the fractional difference at three different energies, illustrating typical fractional differences in different energy regions.

The list of energies was modified until the fractional error between interpolated and evaluated grids for all energies was a few-% in the regions of low cross section, and sub-% in the regions of high cross section. The final list was used for the tables input into NEUT, and is stated in Section 6.2.2.

The interpolation method worked well for all energies, though energies around $E_\nu = 1.5$ GeV were problematic. The tables were produced with a value of $\alpha = 1.5$ GeV, and the equation for the values of $\cos\theta_\mu$ at which to evaluate the cross section, Equation 6.6, is discontinuous at $E_\nu = \alpha$. This problem is avoided by evaluating the cross section at two points very close to $E_\nu = 1.5$ GeV (one higher, one lower). The probability of an event being drawn with an energy between these is small, so the discontinuity is avoided. If an energy is drawn in this range, the energy is changed to be equal to the value at which the higher table is evaluated. Since the two tables are very close, this change is negligible.

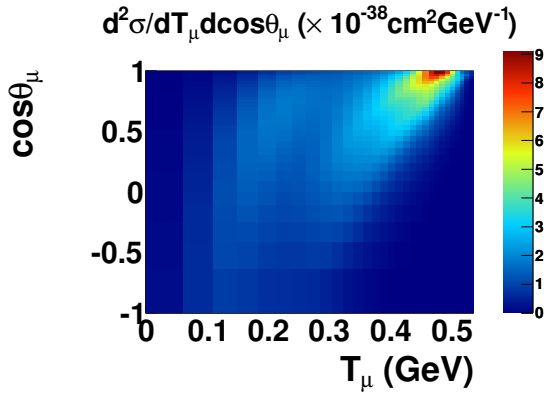

(a) Double-differential cross section grid evaluated at $E_\nu = 0.55$ GeV

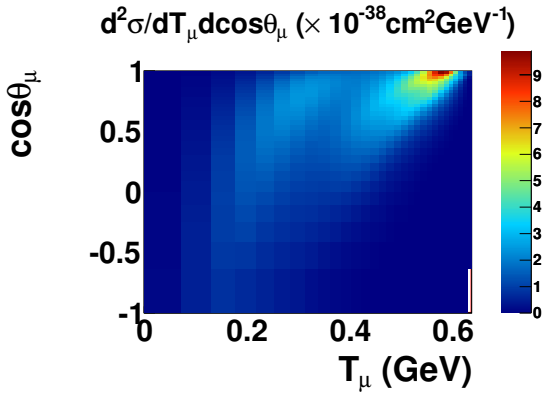

(b) Double-differential cross section grid evaluated at $E_\nu = 0.65$ GeV

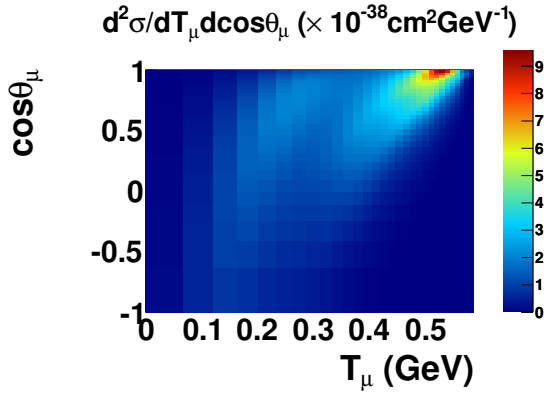

(c) Double-differential cross section grid evaluated at $E_\nu = 0.60$ GeV

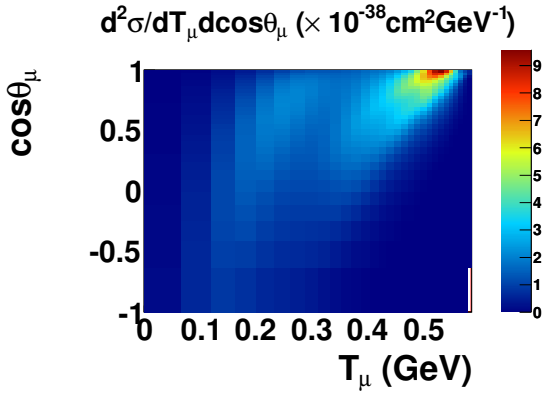

(d) Double-differential cross section grid obtained by interpolating between grids at $E_\nu = 0.55$ GeV and 0.65 GeV.

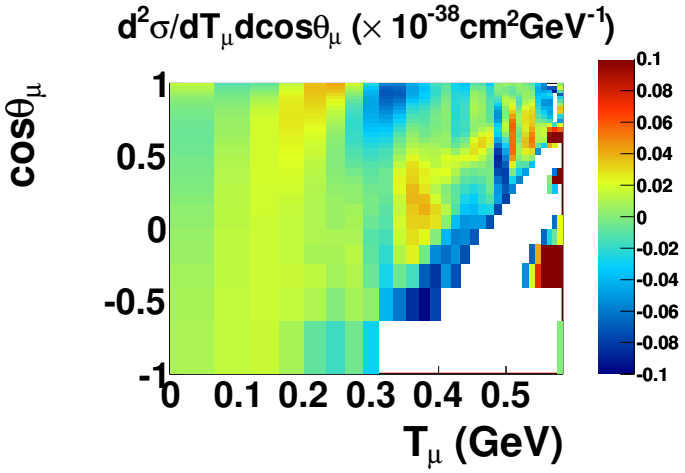

(e) Fractional difference between cross section grids interpolated to and evaluated at $E_\nu = 0.60$ GeV. Red and white bins indicate a fractional difference of $> \pm 10\%$ respectively.

Figure 6.16.: Set of plots illustrating a comparison between evaluated and interpolated grids. All are produced for ν_μ on O^{16}

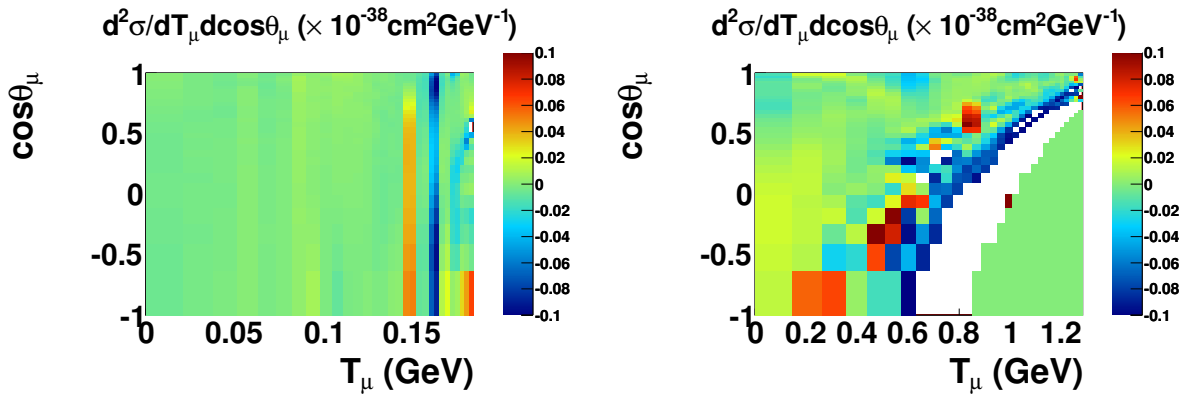

(a) Interpolated at $E_\nu = 0.200$ GeV from grids at 0.190 GeV and 0.205 GeV.

(b) Interpolated at $E_\nu = 1.30$ GeV from grids at 1.25 GeV and 1.40 GeV.

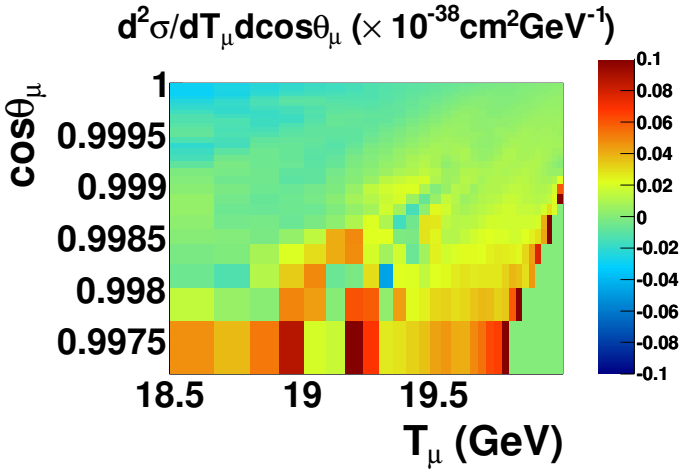

(c) Interpolated at $E_\nu = 20$ GeV from grids at 10 GeV and 30 GeV.

Figure 6.17.: Set of plots illustrating a comparison between evaluated and interpolated grids. All are produced for ν_μ on O^{16}

6.3.3. Validation of total cross section for multinucleon neutrino mode in NEUT

The section describes a validation study to confirm that the multinucleon neutrino mode was implemented with the correct total cross section for all relevant neutrino types and all targets. The correct total cross section is defined as that saved in the total cross section table, produced as described in Section 6.2.3. This study does not validate the production of the total cross section table itself, which was previously validated by a comparison of the ν_μ total cross section to that generated with NuWro.

The study is a by-eye comparison of the total cross section calculated from integration of the double differential cross section tables with the total cross section reconstructed from output NEUT MC files.

MC files were produced with 1×10^6 events. One file of ν_μ on C^{12} was produced with all interaction modes chosen according to their total cross sections. Eight additional files were produced with all events forced to be multinucleon neutrino interactions. One file was produced for each neutrino flavour (ν_μ, ν_e, $\overline{\nu}_\mu$, $\overline{\nu}_e$) on each target (C^{12} and O^{16}). All files were produced with a flat input neutrino flux between 0 and 30 GeV.

For each file, events were binned by neutrino energy. Bins were normalised by width, and the histograms were normalised by the number of events in the MC file. All bins were then normalised by the integral of the flux in the energy range of each bin, so the final histogram was equivalent to the average cross section in that bin. The bin widths were sufficiently narrow such that non-linear changes in the cross section in each bin were negligible, so the bin content is approximately the total cross section at the bin center. These histograms were then compared to the corresponding cross sections from the input cross section files. If the implementation is correct, they should be the same.

Figures 6.18 and 6.19 show a comparison of the total cross section for the multinucleon neutrino mode from the tables with that reconstructed from a NEUT MC file. Figures 6.18 shows all neutrino flavours on C^{12}, and Figure 6.19 shows all neutrino types on O^{16}. The two calculations for each flavour and target are the same within the MC statistical error.

Figures 6.20 and 6.21 show a comparison of the total cross sections input into NEUT for several groups of interaction modes with that reconstructed from a NEUT MC file. Figure 6.20 shows the cross section around the production threshold up to $E_\nu = 1.7$ GeV, and Figure 6.21 shows the cross section up to $E_\nu = 30$ GeV. These plots show that the

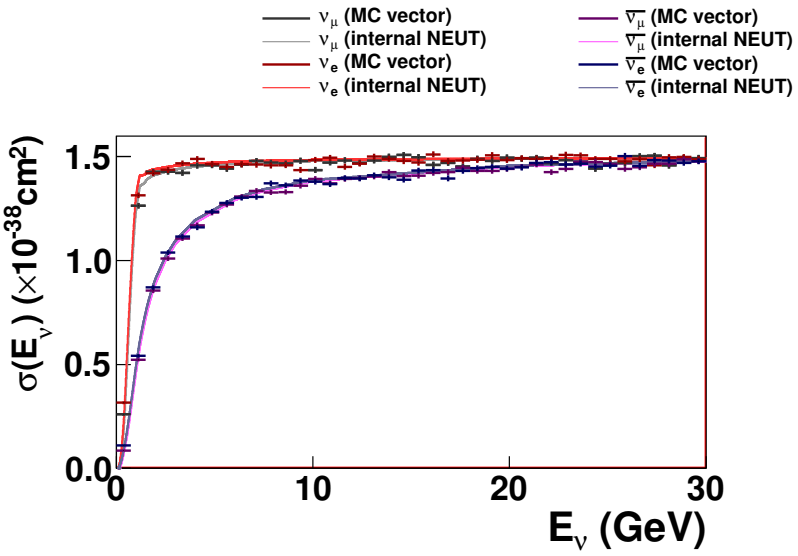

Figure 6.18.: Total cross section of multinucleon neutrino interactions on C^{12} from input table compared to that reconstructed from NEUT MC file.

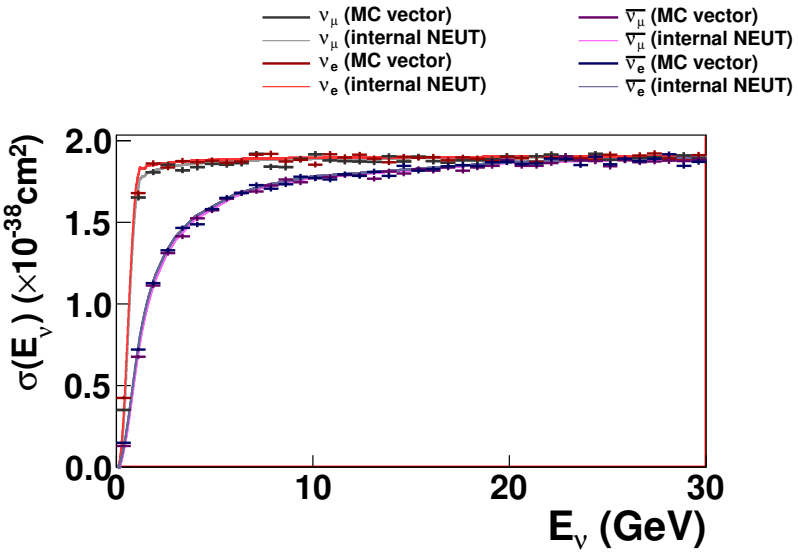

Figure 6.19.: Total cross section of multinucleon neutrino interactions on O^{16} from input table compared to that reconstructed from NEUT MC file.

cross sections reconstructed from the MC file are consistent with the input cross sections for all modes, so inclusion of the additional multinucleon neutrino mode does not affect the cross sections of other NEUT modes.

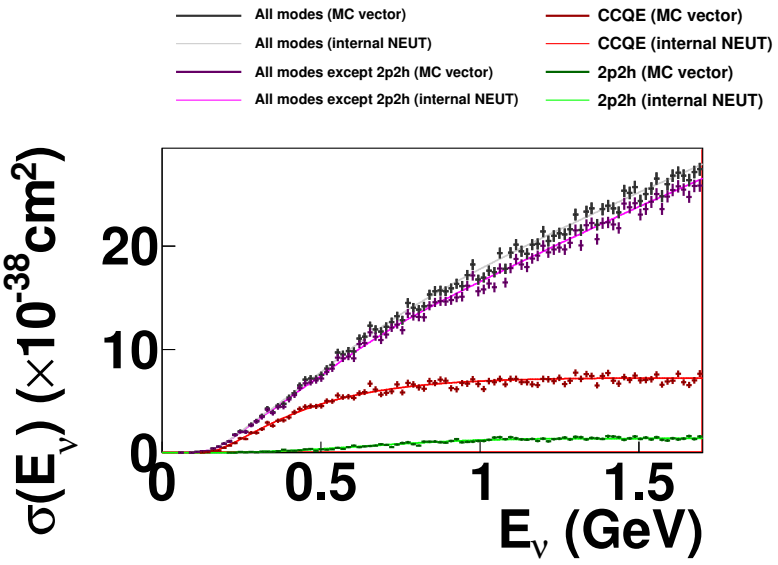

Figure 6.20.: Total cross section for multinucleon neutrino mode, CCQE, total CC and total CC minus multinucleon neutrino modes for ν_μ on C^{12} (lines) compared to the same mode reconstructed from NEUT MC file.

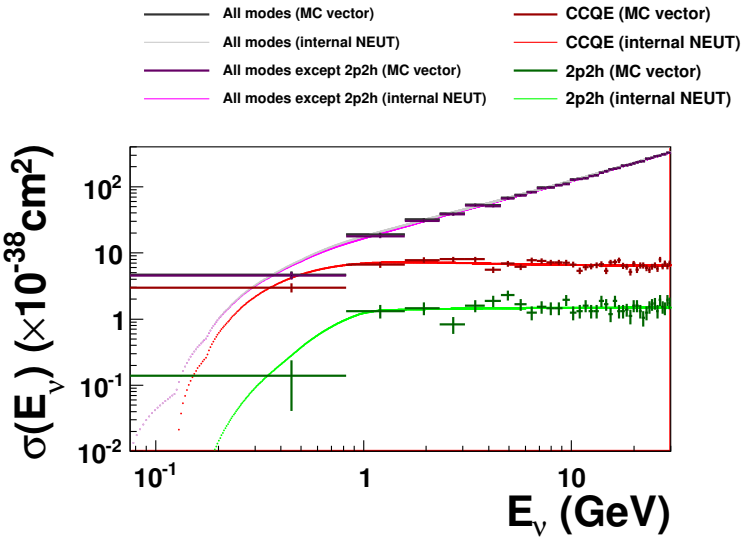

Figure 6.21.: Total cross section for multinucleon neutrino mode, CCQE, total CC and total CC minus multinucleon neutrino modes for ν_μ on C^{12} (lines) compared to the same mode reconstructed from NEUT MC file.

6.3.4. Validation of double-differential lepton cross section implementation

A study was performed to confirm the double-differential cross sections input into NEUT (as described in Section 6.2.4) are consistent with the muon kinematic distributions in the final NEUT MC files. The study was performed as follows:

1. For each energy, a 2D histogram was created in T_μ and $\cos\theta_\mu$, with the bin boundaries set to the points at which the differential cross section was evaluated.
2. The histogram was filled by linearly interpolating the cross section table from the bin corners to the bin centers
3. The total volume of this histogram is calculated by bilinear integration.
4. MC files were produced with 1×10^6 ν_μ on C^{12} for a number of fixed neutrino energies between zero and 30 GeV. All events were set to be multinucleon neutrino interactions.
5. For each file, a histogram was created with the same binning as before for each E_ν.
6. Events in each MC file were binned by the value of the muon T_μ and $\cos\theta_\mu$.
7. Each bin of the MC histogram was normalised by area, and the total volume was normalised to that of the equivalent cross section table histogram.
8. For each pair of histograms with the same E_ν (one created with the NEUT MC, the other with the cross section tables), the bin pulls were calculated.
9. The pull was plotted with the same binning scheme, and the plot was inspected for areas with consistently high values.
10. The pull was binned in 1D, and a Gaussian is fit to the histogram
11. For all energies, the mean and width of the fitted Gaussian are plotted as a function of neutrino energy.

The pull was defined as:

$$\mathrm{Pull_i} = \frac{N^{\mathrm{MC}_i} - N^{\mathrm{in}_i}}{\sigma^{\mathrm{MC}_i}}, \tag{6.11}$$

where N_i is the number of entries in histogram bin i, the superscript 'MC' relates to the NEUT MC histogram, the superscript 'in' relates to the input cross section table, and σ_i^{MC} is the statistical error of the MC histogram. The pull distribution calculated with two statistically consistent distributions will be Gaussian distributed with unit width and zero mean.

Figures 6.22 and 6.23 show the MC and reference histograms for two different energies, with maps of the pull in each T_μ-$\cos\theta_\mu$ bin, and 1D histograms of the pull. No structure can be seen in either residual map, showing that there are no areas of the T_μ-$\cos\theta_\mu$ space with particularly poor agreement. Both pull distributions appear to be Gaussian distributed, and the fitted Gaussian parameters are consistent with unit width and zero mean.

Comparisons were performed with 27 neutrino energies between zero and 30 GeV. No structure was noticeable in any pull map. The fitted Gaussian parameters were extracted, and are shown plotted as a function of E_ν in Figure 6.24. The error bars in the points are the fitted parameter errors. The means and widths are generally consistent with zero and one respectively, though there is possible evidence of a bias towards widths less than one. This bias was investigated, and the likely cause was found to be the fit method employed in ROOT. Repeating fits with different fitter settings (specifically the default χ^2 minimiser and a log-likelihood minimiser with the 'LL' setting) resulted in less bias in the width distribution, though introduced a bias in the means. By-eye inspection of all Gaussian distributions shows no obvious bias, so it is likely that the cause of the bias was in the fits to the residuals rather than in the implementation itself.

6.4. Validation of hadronic simulation

The model employed for simulation of the hadrons in the NEUT multinucleon neutrino mode is almost identical to that implemented in the NuWro generator, so a comparison of nucleon distributions between the two generators is an obvious check of the NEUT implementation. However, the minor differences in the implementations, notably in the nucleon momentum distributions, treatment of nucleon binding, and treatment of Pauli-blocking, are sufficient to make the nucleon kinematics in multinucleon neutrino interactions between NEUT and NuWro quite different, so validation by these comparisons is not possible.

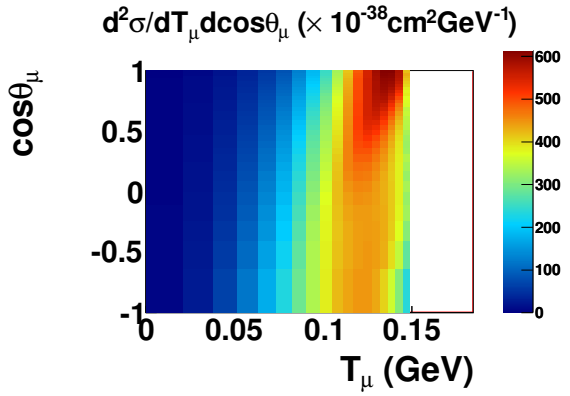

(a) Double-differential cross section input into NEUT

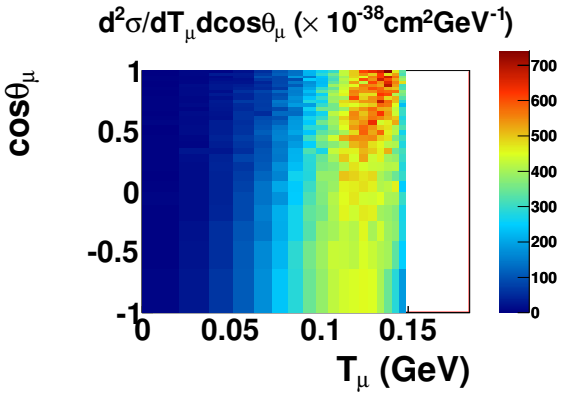

(b) Muon kinematic distribution. Bins normalised by area, total volume normalised to that of input histogram.

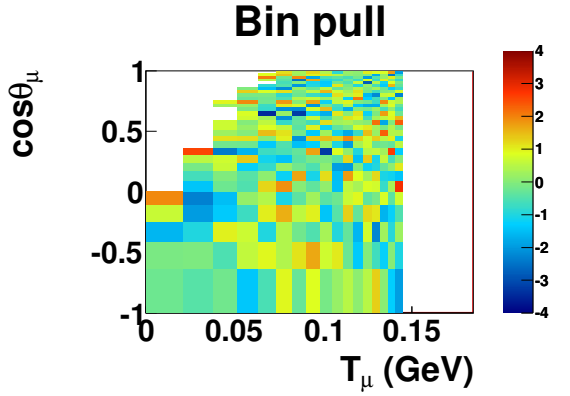

(c) Map of pulls between Figures 6.22a and 6.22b

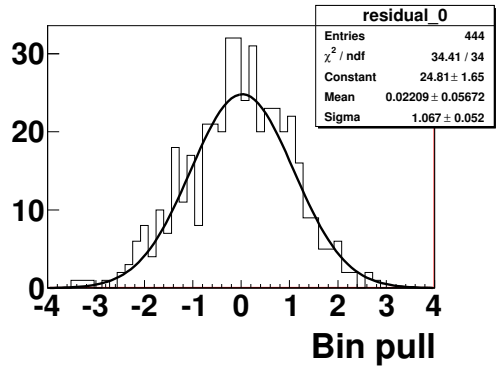

(d) Pull distribution

Figure 6.22.: Input and MC histograms for ν_μ on C^{12} with $E_\nu = 200$ MeV, shown with the map of pulls in each bin, and the pull distribution.

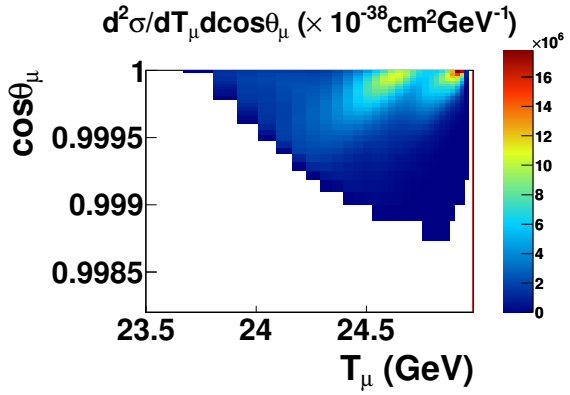

(a) Double-differential cross section input into NEUT

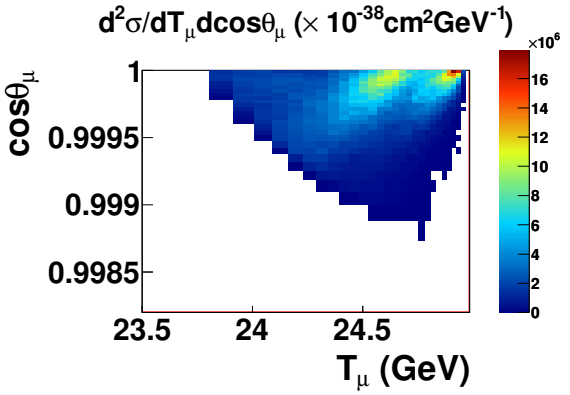

(b) Muon kinematic distribution. Bins normalised by area, total volume normalised to that of input histogram.

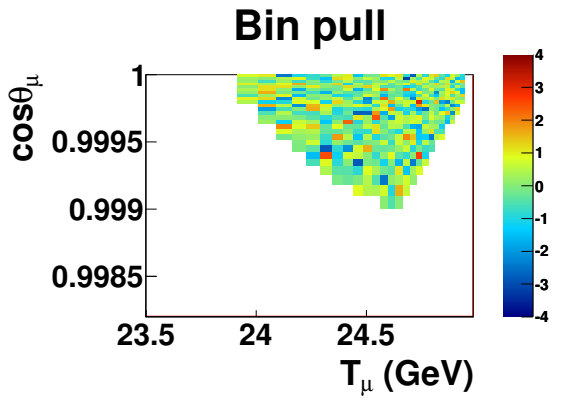

(c) Map of pulls between Figures 6.22a and 6.22b

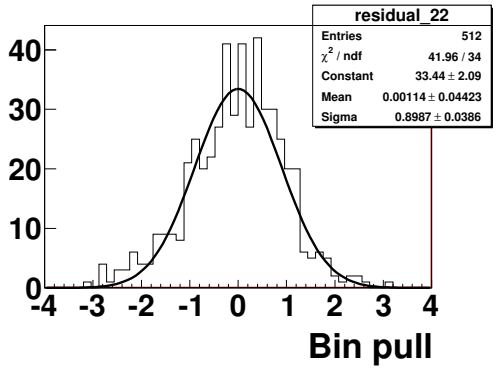

(d) Pull distribution

Figure 6.23.: Input and MC histograms for ν_μ on C^{12} with $E_\nu = 25$ GeV, shown with the map of pulls in each bin, and the pull distribution.

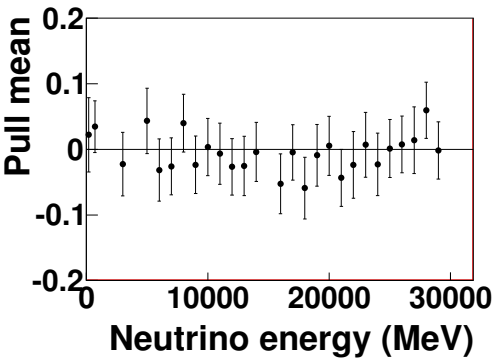

(a) Mean

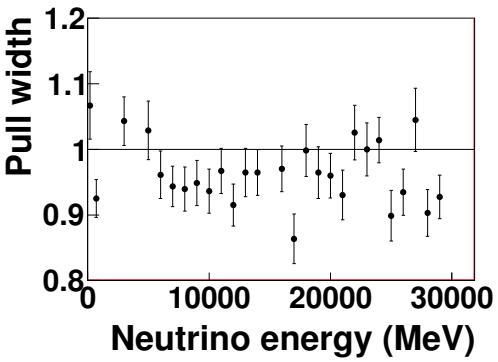

(b) Width

Figure 6.24.: Gaussian parameters in fits to pull distributions

The implementation of the hadron model in multinucleon neutrino interactions was validated by inspecting the distribution of a number of kinematic variables relating to the hadrons. The fine details of the distributions cannot be used to verify the validity of the implementation since there is no control sample to which they can be compared, however any obvious discrepancies should be identified (e.g. energy non-conservation or other unphysical effects). All plots shown in this section show hadron properties before FSI.

Figure 6.25 shows conserved properties of the multinucleon neutrino interactions for two neutrino energies: $E_\nu = 700$ MeV and 29 GeV. Figure 6.25a shows the difference in total energy between the initial and final state. For the low energy neutrinos the mean difference is very close to zero, though with some offset. The source of the offset was extensively checked but never confirmed, however the size of the offset is negligible ($\mathcal{O}(200$ eV)) compared to typical neutrino energies in the T2K flux ($\mathcal{O}(600$ MeV)). This can be seen in Figure 6.25b, which shows the energy difference as a fraction of the initial neutrino energy. The energy difference is $\mathcal{O}(10^{-6})$ as a fraction of the neutrino energy for interactions with $E_\nu = 700$ MeV, and smaller for larger neutrino energies. There is a small spread in the energy difference, the source of which is again unknown, and again small enough to be ignored. Figures 6.25c to 6.25e show difference in initial state momenta in the x, y, and z directions. Again there is a negligibly small spread in the momentum difference. The spread in the z-direction is larger because the neutrino momentum was set to be purely in the z-direction in the MC simulation.

Figure 6.26 shows properties of the multinucleon neutrino interaction vertex. Figure 6.26a shows the distance between the interaction vertex and the nuclear center. Figure 6.26b shows the distance between the interaction vertex and the final-state nucleon start position, illustrating the effect of the hadron formation length in NEUT.

Figures 6.27 and 6.28 show properties of the particles in the multinucleon neutrino interactions. Figures 6.27a to 6.27d show the initial and final-state nucleon momenta. The initial state momenta are the same for both energies, but higher energy neutrinos generally produce higher energy final-state hadrons. The affect of Pauli-blocking is seen by the deficit of very low momentum final-state nucleons. Figures 6.27e and 6.27f show the angle between the initial state nucleons and the neutrino. The nucleon momenta are slightly anti-correlated, which is the configuration which maximises center of mass energy, therefore maximising the probability of the hadronic system gaining enough energy to overcome the binding energy. Figures 6.28a and 6.28b show the angle between final-state nucleons and the neutrino. Differences between high and low-energy distributions are

driven by the Pauli-blocking of the low-energy hadron. Higher energy neutrinos tend to transfer more energy to the hadronic system so produce higher-momentum hadrons. These are less likely to be Pauli-blocked, so do not need to be as correlated with the neutrino direction. Figure 6.28c shows that the final-state nucleons are back-to-back in their center-of-mass frame as intended. Figure 6.28d shows the angle between final-state nucleons in the lab frame. Higher energy hadrons tend to be more colinear. Figure 6.28e shows that the initial-state hadrons are not correlated, as intended.

Figure 6.29 shows plots of higher-level properties of the multinucleon neutrino interactions. The energy-transfer from leptonic to hadronic systems is shown in Figure 6.29a, which is very similar to the total kinetic energy in the hadronic system shown in Figure 6.29b, especially for higher energy neutrinos. Figure 6.29c shows the difference between the true final-state nucleon and the direction which would be inferred by the muon kinematics, assuming a CCQE interaction with a stationary nucleon. This is an important variable which can be used to distinguish CCQE from non-CCQE interactions if one final-state nucleon is observed. Figure 6.29d shows the difference between the true neutrino energy and that reconstructed from the muon kinematics, again assuming a CCQE interaction on a stationary nucleon. Larger energy transfer to the hadronic system tends to produce a greater bias, as more energy is lost to the hadrons. Figure 6.29e shows the magnitude of the 3-momentum transfer from the leptonic to hadronic system. The 3-momentum cut-off can clearly be seen in the higher-energy neutrino sample. Figure 6.29f shows the Q^2 of the interaction, showing a harder spectrum for higher neutrino energies as expected.

The distributions all show spectra which are understandable and explainable given the leptonic and hadronic models. No obvious errors in the implementation of the hadronic simulation can be inferred from the plots shown in this section.

6.5. First comparisons of NEUT with multinucleon neutrino interactions to T2K data

The addition of the multinucleon neutrino interaction mode is a substantial change to the interaction model in NEUT, and the effect of this change on the T2K MC prediction should be understood before its inclusion into official T2K analyses. To this end a number of short studies were performed. The core of the studies is a comparison of the official

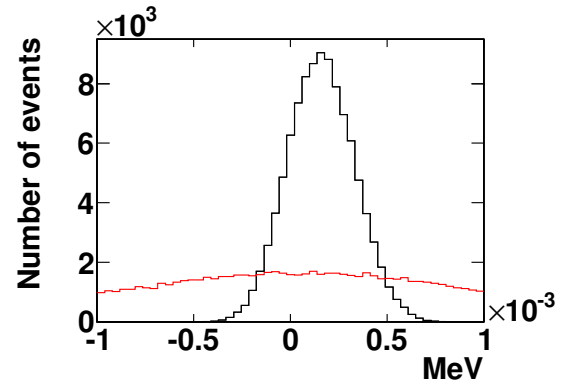

(a) Energy difference

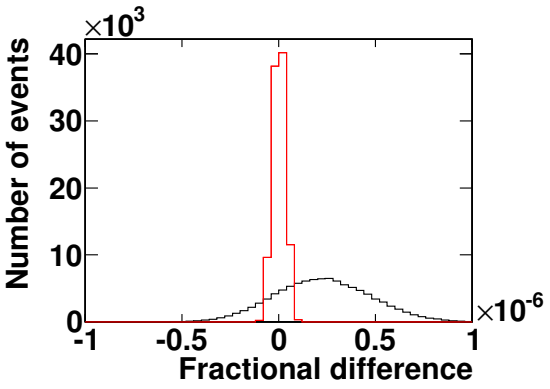

(b) Energy difference as a fraction of initial neutrino energy

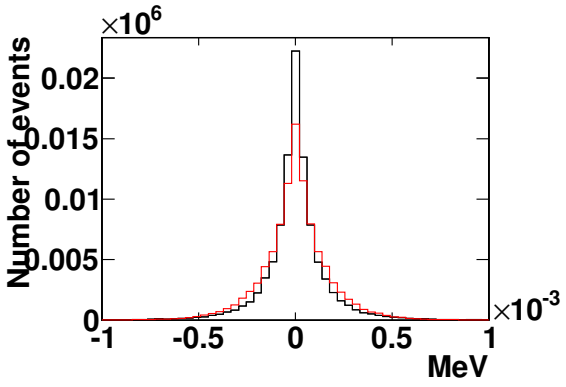

(c) Momentum difference (x-direction)

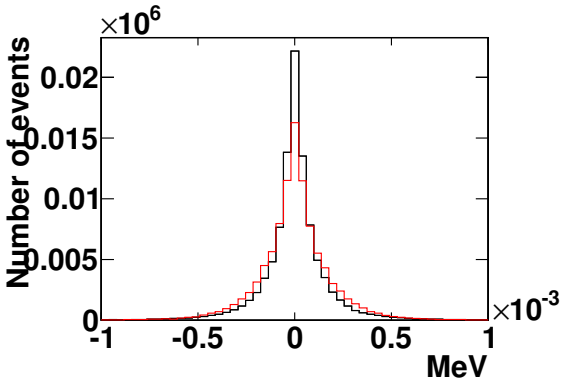

(d) Momentum difference (y-direction)

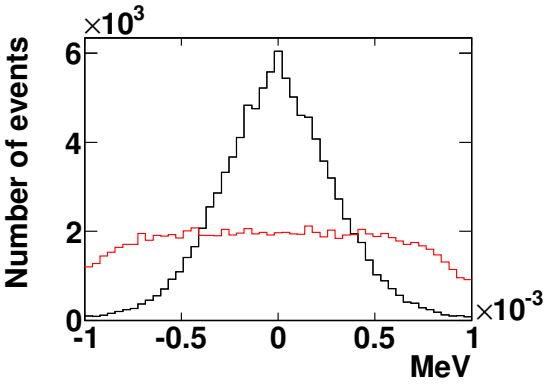

(e) Momentum difference (z-direction)

Figure 6.25.: Difference between quantities calculated from initial and final state particles. Black line shows properties for $E_\nu = 700$ MeV, red shows $E_\nu = 29$GeV.

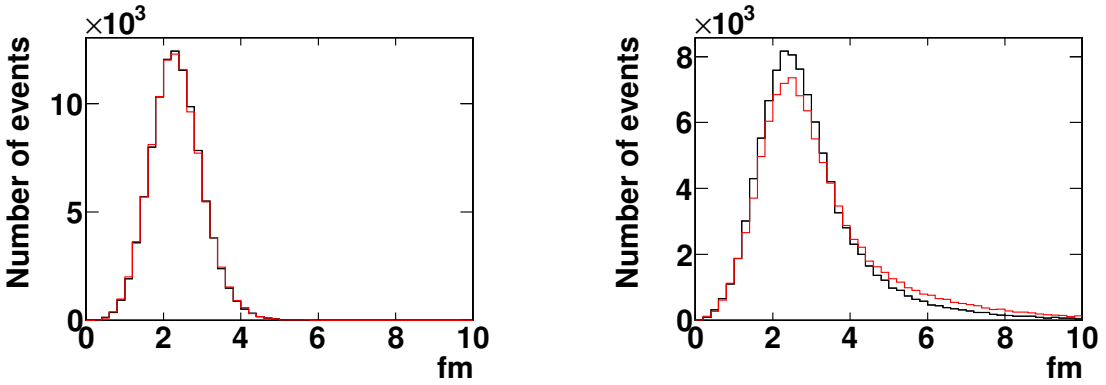

(a) Distance of neutrino interaction vertex to nucleus center

(b) Difference between vertex position and hadron start position

Figure 6.26.: Plots illustrating properties of the interaction vertex. Black line shows properties for $E_\nu = 700$ MeV, red shows $E_\nu = 29$GeV.

T2K detector MC production used in the 2013 analyses to an equivalent MC simulation including the multinucleon neutrino interaction mode.

A new version of NEUT was created, identical to the version used in the 2013 T2K analyses but with the addition of the multinucleon neutrino interaction mode as described in Section 6.2. Using this new version of NEUT as the generator, the entire MC production chain for the T2K near-detector was run as described in Section 4.5. This set of MC is referred to as the '2p2h MC' (though it contains all interaction modes). The set of MC used in the T2K analyses published in 2013 is hereafter referred to as the 'official MC'.

The T2K near-detector data has recorded interactions from 5.90×10^{20} POT as of the end of 2013. To minimise the effect of MC statistical errors in the fits, a much larger number of POT equivalent in the MC files is required. The standard for T2K oscillation analyses is to use at least 10 times the amount of POT in the MC files as in the data files, so 6.321×10^{21} POT was simulated in the 2p2h MC. Table 6.1 shows the breakdown into the different run periods of the data POT, the official MC, and the 2p2h MC.

As described in Section 3.3.2, the pionless delta decay component of Nieves' 2p2h model is included already in the previous version of NEUT. When using the 2p2h MC then, all pionless delta decay events simulated by NEUT (excluding those in the 2p2h mode) are removed from the analysis. Correspondingly, when the 2p2h mode is excluded

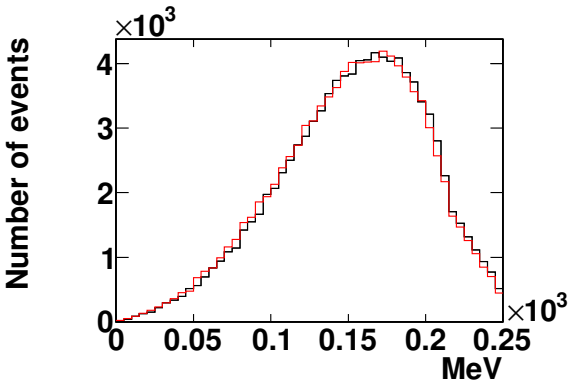

(a) Highest initial hadron momentum

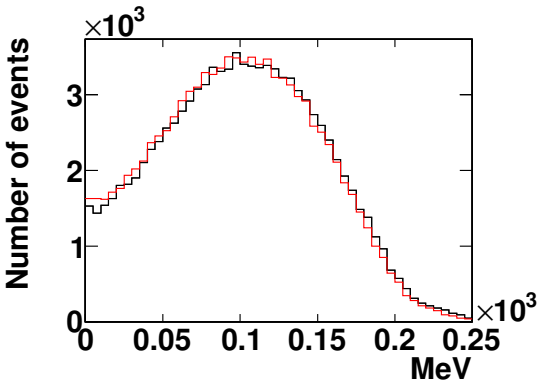

(b) Lowest initial hadron momentum

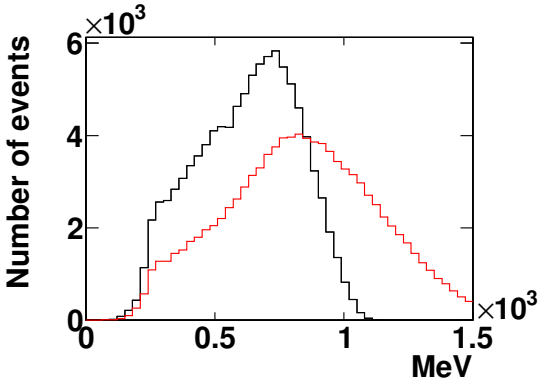

(c) Highest final hadron momentum

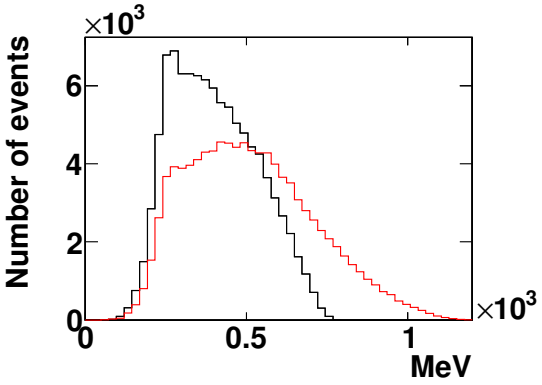

(d) Lowest final hadron momentum

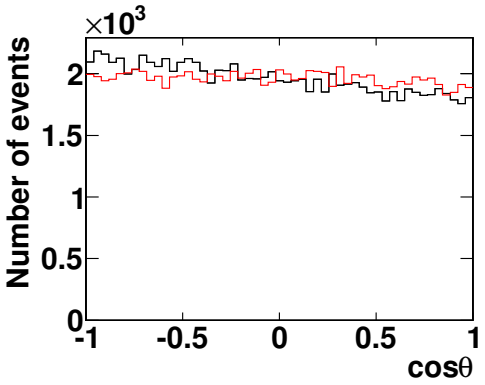

(e) Cosine of angle between highest initial hadron and neutrino

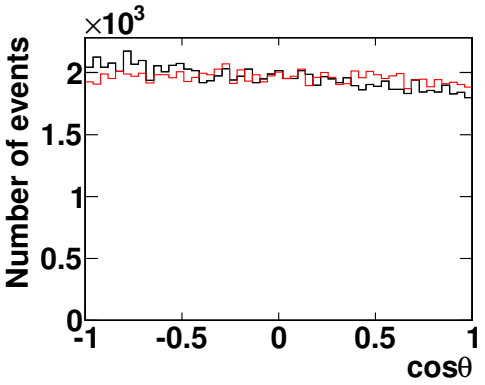

(f) Cosine of angle between lowest initial hadron and neutrino

Figure 6.27.: Plots illustrating properties of the particles in multinucleon neutrino interactions. Black line shows properties for $E_\nu = 700$ MeV, red shows $E_\nu = 29$GeV.

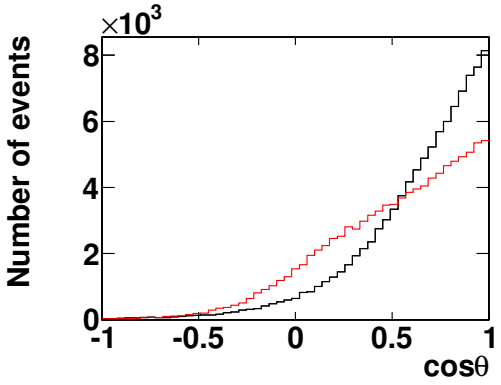

(a) Cosine of angle between highest final hadron and neutrino

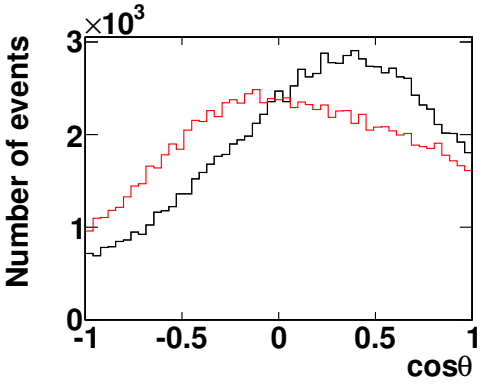

(b) Cosine of angle between lowest final hadron and neutrino

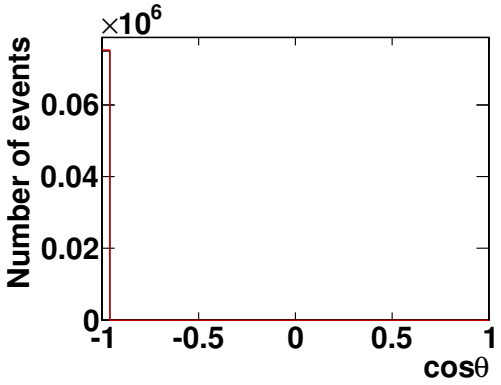

(c) Cosine of angle between the two final-state hadrons in hadron center of mass frame

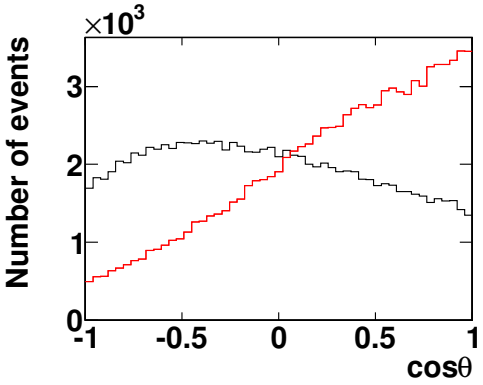

(d) Cosine between final-state nucleons in lab frame

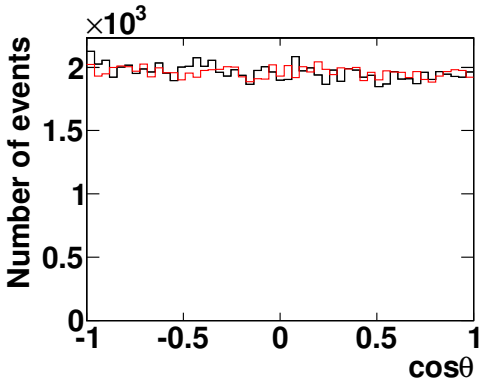

(e) Cosine of angle between initial-state hadrons

Figure 6.28.: Plots illustrating properties of the particles in multinucleon neutrino interactions. Black line shows properties for $E_\nu = 700$ MeV, red shows $E_\nu = 29$GeV.

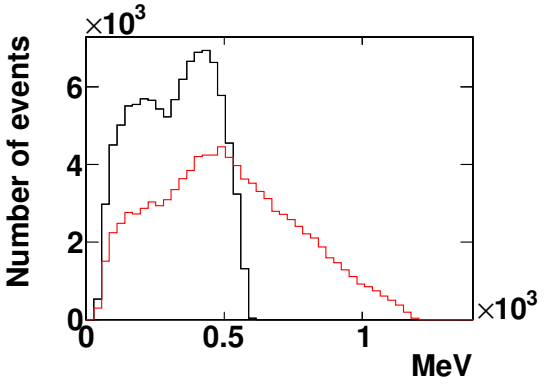

(a) Energy transfer from leptonic to hadronic system

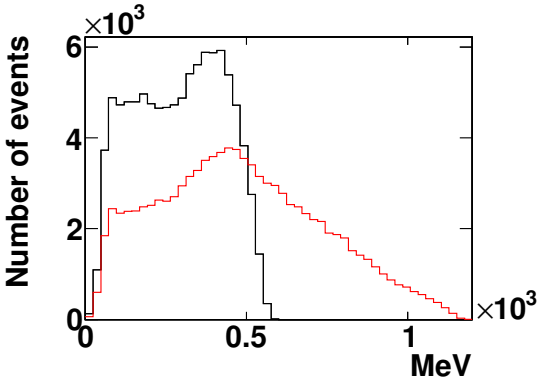

(b) Total final-state nucleon kinetic energy

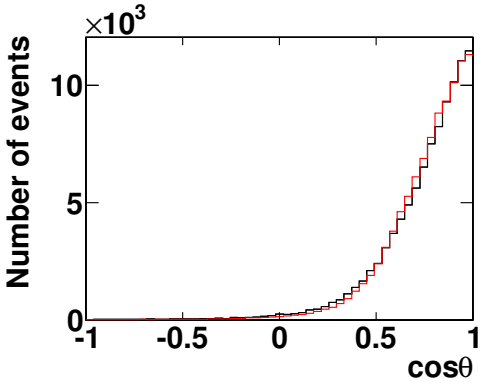

(c) Cosine between direction of highest final-state nucleon and direction inferred from muon kinematics assuming CCQE interaction

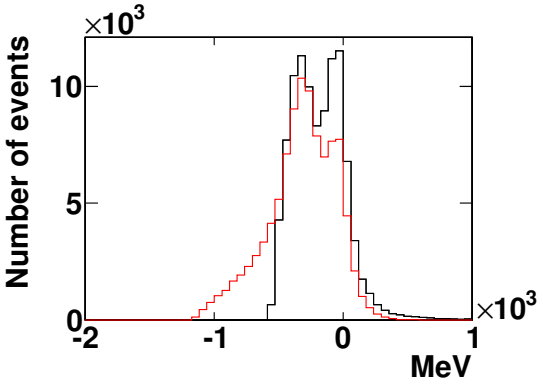

(d) Difference between true neutrino energy and E^{ν}_{QE}

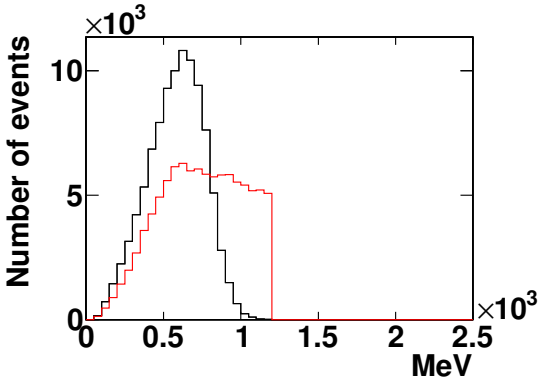

(e) Magnitude of 3-momentum transfer

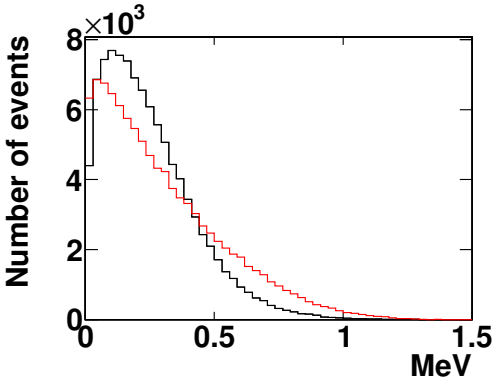

(f) 4-momentum transfer squared

Figure 6.29.: Plots illustration higher-level properties of multinucleon neutrino interactions. Black line shows properties for $E_{\nu} = 700$ MeV, red shows $E_{\nu} = 29$GeV.

Run period	Water/air	Data POT	Official MC POT	2p2h MC POT
1	Water	1.67×10^{19}	3.0×10^{20}	1.495×10^{20}
2	Water	4.28×10^{19}	6.0×10^{20}	3.945×10^{20}
2	Air	3.55×10^{19}	6.0×10^{20}	3.475×10^{20}
3b	Air	2.14×10^{19}	3.0×10^{20}	2.15×10^{20}
3c	Air	1.348×10^{20}	1.5×10^{21}	1.35×10^{21}
4	Water	1.625×10^{20}	1.8×10^{21}	1.975×10^{21}
4	Air	1.762×10^{20}	1.6135×10^{21}	1.8895×10^{21}
Total		5.899×10^{20}	6.7135×10^{21}	6.321×10^{21}

Table 6.1.: Data POT for each run period and equivalent POT in official and 2p2h MC files. The water/air configuration labels run periods in which the water bags in the PØD were filled with water or air, which require a different geometry configuration in the MC.

(for a comparison to the original NEUT MC prediction), pionless delta decay events are included as normal. This is done in all studies described in this section.

Using the official and 2p2h MC sets, some basic event selections were performed, and kinematic distributions were compared between those from T2K data. This is described in Section 6.5.1.

Next, fits were performed to the near-detector data using a Markov Chain Monte Carlo parameter estimation method. This was done using the 2p2h MC, and separately using the 2p2h MC while explicitly excluding all 2p2h events. This study is described in Section 6.5.2.

Finally, a Bayesian goodness-of-fit method was used to compare the two fits (one using the 2p2h MC, and one using the 2p2h MC excluding 2p2h events). The goodness-of-fit method is described, and a toy MC study of the properties of the method is shown in Appendix A. The goodness-of-fit method is performed using the output of the two Markov Chain fits. This is described in Section 6.5.3.

6.5.1. Comparison of untuned MC prediction to T2K data

In the T2K oscillation analyses published in 2013, three mutually exclusive near-detector data samples were selected. The samples are defined such that they can provide separation between different groups of interaction modes, with the intention of maximising sensitivity

to flux and cross section parameters which are constrained with near-detector data. These samples of events are then used to tune the flux and cross section parameters.

The three standard samples are a good place for a first-order comparison of the NEUT model including multinucleon neutrino interactions with T2K data. The selections are simple and well-established, so a direct comparison of the untuned models and the data can be made.

The three samples are separated based on the number of reconstructed pions in the event, and are labelled: CC0π, CC1π^+, and CCother (the CC stands for charged current, since all selected events must have a reconstructed charged lepton). The three event selections are summarised here, and are described in detail in [80]. The three selections are made identically for data and MC.

First, a general inclusive sample is selected by performing the following cuts:

1. Reject all tracks in spills that do not have a good global ND280 data quality flag. Associate remaining tracks with events using their hit times.
2. Reject events with no reconstructed tracks in the TPCs
3. Reject events with no reconstructed tracks in the FGD1 fiducial volume
4. Reject events with no muon candidate tracks. Muon candidates are defined by the following criteria:
   a) Reconstructed in both the TPC and FGD
   b) Start in the fiducial volume of FGD1
   c) Associated with at least 18 TPC clusters
   d) Negative charge (from track curvature)
5. For events with greater than one track, reject events in which the highest momentum track with an associated energy deposit in the TPC has a start position greater than 150 mm upstream of the start position of the muon candidate.
6. Define tracks which are reconstructed in FGD1 with no associated energy deposit in the TPCs as FGD-only tracks. Reject events in which the muon candidate has a start position greater than 425 mm from the upstream edge of FGD1, and in which there is an FGD-only track with a start position outside of the FGD fiducial volume.

7. Reject events in which the muon candidate fails a muon-like PID cut

Events which pass all of these cuts are separated into the three samples. The CC0π sample is selected by the following criteria:

1. Reject events with one or more tracks in either the TPC or the FGD which have pion-like PID
2. Reject events with a reconstructed Michel electron.

The CC1π^+ sample is selected by the following criteria:

1. Reject events included in the CC0π sample
2. Reject events with reconstructed negatively charged pions in the TPC
3. Reject events with reconstructed electrons or positrons in the TPC
4. Select events with one reconstructed positive pion or one Michel electron.

All events which pass the general selection but are rejected by both the CC0π and CC1π^+ cuts are included into the CCother sample.

The three selections were performed on the 2p2h MC sample. Events were binned by reconstructed muon momentum and by the cosine of the reconstructed angle between the neutrino and muon directions. The MC was scaled to be equivalent to the number of POT in the T2K data. Figures 6.30 and 6.31 show the distribution of reconstructed muon momentum and muon–neutrino opening angle for the T2K data in run periods 1–4, the official MC simulation, and the 2p2h MC simulation.

The 2p2h MC is shown with two configurations. The first, labelled *2p2h MC* has no additional weighting applied to 2p2h events, and has pion-less delta decay events weighted to zero (i.e. these events do not contribute to the expectation). The second, labelled *2p2h MC without 2p2h*, has no additional weighting applied to pion-less delta decay events, and has 2p2h events weighted to zero. The 2p2h MC excludes pion-less delta decay events because this process is included in the 2p2h cross section, so including them would double-count these events.

The 2p2h MC without 2p2h is directly comparable to the official MC, and should produce an identical prediction. This appears true within statistical errors for the CC0π and CCother samples, but the prediction for the CC1π^+ selection is higher in the 2p2h MC predictions compared to the official prediction, particularly towards higher muon

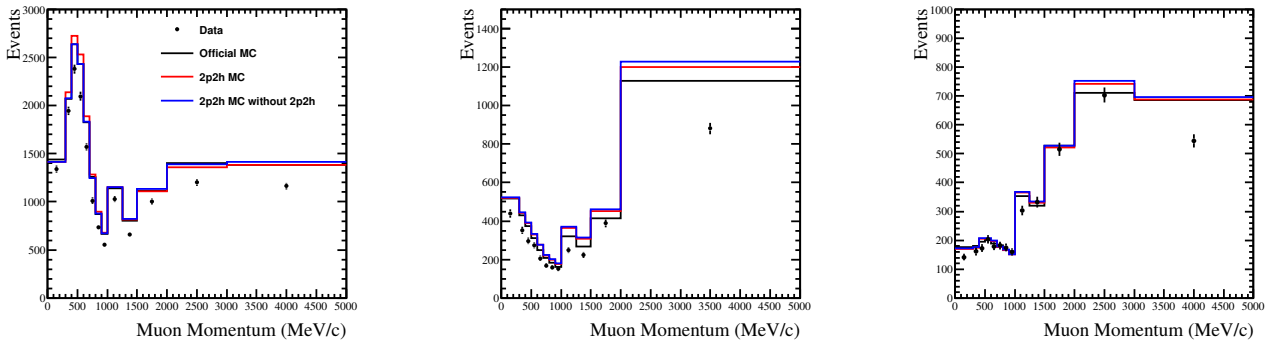

Figure 6.30.: Expected reconstructed muon momentum distributions for data periods 1–4 predicted by the official T2K MC (black), the 2p2h MC sample with pion-less delta decay events excluded (red) and the 2p2h MC sample with 2p2h events excluded (blue), with the T2K data in run periods 1–4. The three selections are shown separately: CC0π (left), CC1π^+ (middle), and CCother (right).

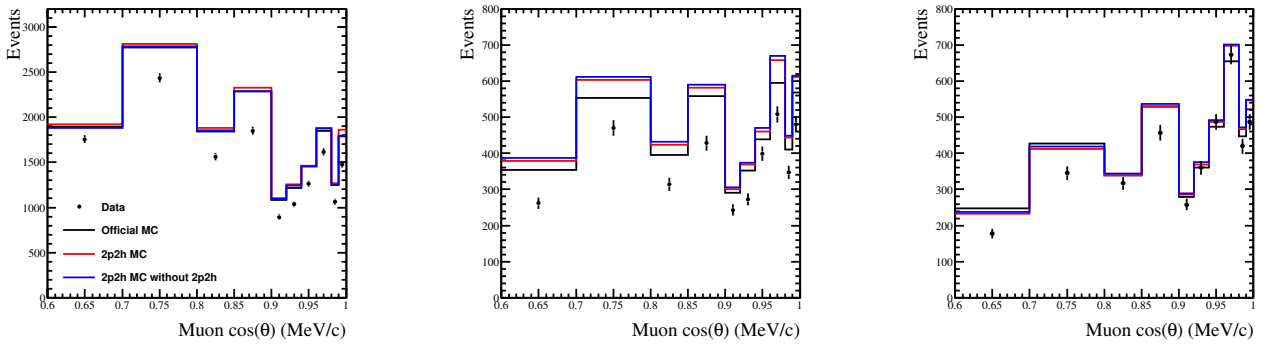

Figure 6.31.: Expected distributions for neutrino–muon opening angle for data periods 1–4 predicted by the official T2K MC (black), the 2p2h MC sample with pion-less delta decay events excluded (red) and the 2p2h MC sample with 2p2h events excluded (blue), with the T2K data in run periods 1–4. The three selections are shown separately: CC0π (left), CC1π^+ (middle), and CCother (right).

momentum. This discrepancy was the subject of extensive study, but the ultimate cause is unknown. As described in Section 6.3.3, validation studies were performed to ensure the cross sections of all processes in NEUT were the same before and after the modification, so it is likely the source of the difference lies in the detector simulation. The official and 2p2h MC samples may have been produced with slightly different detector MC or beam configurations.

This discrepancy should not obscure the main results of this work. As can be seen from the difference between the 2p2h MC and the 2p2h MC without 2p2h, the majority of the 2p2h events are included in the CC0π selection, which generally shows good agreement between the official and the 2p2h MC without 2p2h events. While differences in best-fit parameters which affect the CC1π^+ sample should not be trusted, firm conclusions can still be drawn from differences in best-fit parameters which affect the CC0π sample.

6.5.2. Fitting T2K data with NEUT including 2p2h

To see the effect of the multinucleon neutrino model on the far-detector prediction, the 2p2h MC (excluding pion-less delta decay events) was fit to the T2K near-detector data, and the values of the fitted parameters were compared to those from a fit using the 2p2h MC without 2p2h events.

The program which was used to fit the 2p2h MC to the T2K data is a preexisting fitter used in several T2K analyses, including near-detector fits using the official T2K MC, and simultaneous fits to near and far-detector data [81, 82]. This fitter uses a Markov chain Monte Carlo method with the Metropolis-Hastings algorithm [83] to sample the joint posterior distribution of a set of parameters.

First, the principles of Markov chain Monte Carlo are briefly reviewed, then the fit to the T2K data is described.

Markov chain Monte Carlo and the Metropolis-Hastings algorithm

A Markov process is a stochastic process whereby the state of the system at time $n+1$ is dependent only on the state at time n. This is written as

$$\begin{aligned} P(X_{n+1} = j | X_n = i_n, X_{n-1} = i_{n-1} \dots X_0 = i_0) &= P(X_{n+1} = j | X_n = i_n) \\ &= P(j|i), \end{aligned} \tag{6.12}$$

where $P(X_{n+1} = j)$ is the probability that the system is in state j at time $n + 1$. A Markov chain is a recording of many of these states.

The Metropolis-Hastings algorithm is an algorithm that produces a Markov chain in such a way that the equilibrium distribution of the chain is proportional to a random sample from a probability density function, $p(x)$. The algorithm defines the transition probability between states in the Markov chain, $P(j|i)$.

For this to be possible, two requirements must be met. The first is that transitions between states must be 'reversible', so that the probability of being in state i and transitioning to state j is the same as the probability of being in state j and transitioning to state i. This is written as:

$$p(i)P(j|i) = p(j)P(i|j). \tag{6.13}$$

This is also known as the requirement of detailed balance. The second requirement is that the equilibrium distribution must be aperiodic and positive recurrent, i.e. that there is a non-zero probability of being in the same state more than once in the Markov chain, but not periodically. The Metropolis-Hastings algorithm sets up the transition probability to fulfil these two requirements.

The derivation starts off with the detailed balance equation above. This can be rewritten as:

$$\frac{p(i)}{p(j)} = \frac{P(i|j)}{P(j|i)}. \tag{6.14}$$

The transition can be separated into two steps: a proposal step and an accept/reject step:

$$P(j|i) = g(j|i)A(j|i) \tag{6.15}$$

where $g(j|i)$ is the probability of proposing a step to state j given that the system is in state i, and $A(j|i)$ is the probability of accepting a step from state i to state j. This can be substituted into Equation 6.14:

$$\frac{A(j|i)}{A(i|j)} = \frac{p(j)}{p(i)}\frac{g(i|j)}{g(j|i)}. \tag{6.16}$$

A must be chosen to fulfill this requirement. A common choice, known as the Metropolis choice, is

$$A(j|i) = \min\left(1, \frac{p(j)}{p(i)}\frac{g(i|j)}{g(j|i)}\right). \tag{6.17}$$

This can be simplified using the Metropolis-Hastings choice, where $g(j|i) = g(i|j)$, so that

$$A(j|i) = \min\left(1, \frac{p(j)}{p(i)}\right). \tag{6.18}$$

The algorithm then runs as follows:

1. Choose some initial state i
2. Propose a new state according to $g(j|i)$
3. Accept or reject the state according to $A(j|i)$
    - If step is accepted, new state is j
    - If step is rejected, new state is i
4. Propose new state, iterate.

There is some freedom with this method. The initial state is not defined, and needs to be manually chosen. The final sample of points should be independent of the initial choice. Often, a *burn-in* period is defined, so that some number of chain entries at the start are discarded. The appropriate length of the burn-in depends on the particular fit, and often must be tuned.

A further freedom of the method is the definition of $g(j|i)$. Aside from the requirement in the Metropolis-Hastings choice that it should be symmetric, this is free to be chosen by the user. Again the appropriate choice depends on the particular fit, and it often must be tuned. A balance must be struck between efficient exploration of the parameter space (favouring large step sizes) and efficient acceptance of proposed steps (favouring small step sizes).

For parameter estimation we want the equilibrium distribution of the Markov chain to be proportional to the joint posterior probability of the parameters. This can be obtained by choosing an appropriate choice of the p in the expression for the acceptance

probability in Equation 6.18. If p is chosen to be a likelihood of a set of parameters given the data, the Markov chain will be a directed random walk around the posterior probability space of the parameters.

Application to T2K data

This section describes the application of the Metropolis-Hastings algorithm to the specific environment of T2K analyses, as implemented in the T2K parameter fitter described in References [81, 82].

The parameter fitter uses a proposal function which is a set of uncorrelated Gaussians for each parameter. The width of the Gaussians is approximately one third the width of the prior uncertainty on each parameter, a number chosen by trial-and-error to optimise the performance.

In the acceptance function of Equation 6.18, the p were chosen to be likelihoods, using the same definition of the likelihood as in the official T2K analyses. For fits to near-detector data only, the log-likelihood is defined as:

$$\begin{aligned}\ln\left[L(\vec{b},\vec{x},\vec{s}|d_{\mathrm{ND280}})\right] = &\ln\left[P(d_{\mathrm{ND280}}|\vec{b},\vec{x},\vec{s})\right] \\ &+ \ln\pi(\vec{b}) + \ln\pi(\vec{x}) + \ln\pi(\vec{s})\end{aligned} \tag{6.19}$$

where all quantities are defined in Section 4.6.

The datasets which enter into the likelihood are the three selections described in Section 6.5.1. Each event in the three selections is binned according to the reconstructed muon momentum, $|\mathbf{p}_\mu|$, and the angle between the muon and the neutrino beam direction, $\cos\theta_\mu$. The binning scheme is defined in Reference [84] as:

- CC0π:
  - $|\mathbf{p}_\mu|$: (0, 0.3, 0.4, 0.5, 0.6, 0.7, 0.8, 0.9, 1.0, 1.25, 1.5, 2.0, 3.0, 5.0, 30.0)GeV
  - $\cos\theta_\mu$: (-1, 0.6, 0.7, 0.8, 0.85, 0.9, 0.92, 0.94, 0.96, 0.98, 0.99, 1.0)
- CC1π^+:
  - $|\mathbf{p}_\mu|$: (0, 0.2, 0.3, 0.4, 0.5, 0.6, 0.7, 0.8, 0.9, 1.0, 1.25, 1.5, 2.0, 5.0, 30.0)GeV
  - $\cos\theta_\mu$: (-1, 0.6, 0.7, 0.8, 0.85, 0.9, 0.92, 0.94, 0.96, 0.98, 0.99, 1.0)

- CCother:
  - $|\mathbf{p}_\mu|$: (0, 0.3, 0.4, 0.5, 0.6, 0.7, 0.8, 0.9, 1.0, 1.25, 1.5, 2.0, 3.0, 5.0, 30.0)GeV
  - $\cos\theta_\mu$: (-1, 0.6, 0.7, 0.8, 0.85, 0.9, 0.92, 0.94, 0.96, 0.98, 0.99, 1.0)

The dataset included in the fits is the full accumulated T2K dataset in runs 1–4, with 5.9×10^{20} protons on target in ND280 data.

Both flux and cross section parameters are fit. The cross section parameterisation is as in the 2012 analyses, and the parameters are stated in Table 5.2. There are also six free parameters associated with FSI:

- Inelastic π-N ($p_\pi \leq 500$ MeV)
- Inelastic π-N ($p_\pi \geq 500$ MeV)
- π production
- π absorption
- π-N charge exchange ($p_\pi \leq 500$ MeV)
- π-N charge exchange ($p_\pi \geq 500$ MeV)

These are described in more detail in References [72] and [30]. Uncertainties on these parameters are set as described in Chapter 5, and the full list of uncertainties in each parameter can be found in Reference [72].

Uncertainties on the neutrino flux from a number of sources are evaluated and input into the fit as a covariance matrix in bins of true neutrino energy for the four principle neutrino flavours in the T2K beam. The neutrino flux normalisation in each of these bins is fit. The bin boundaries are:

- ν_μ: 0.0, 0.4, 0.5, 0.6, 0.7, 1.0, 1.5, 2.5, 3.5, 5.0, 7.0, 30.0 GeV
- $\overline{\nu}_\mu$: 0.0, 0.7, 1.0, 1.5, 2.5, 30.0 GeV
- ν_e: 0.0, 0.5, 0.7, 0.8, 1.5, 2.5, 4.0, 30.0 GeV
- $\overline{\nu}_\mathrm{e}$: 0.0, 2.5, 30.0 GeV

The covariance matrix for the flux parameter uncertainties, taken from Reference [84], is shown in Figure 6.32. Diagonal errors are on the order of 10% in the peak ν_μ flux region.

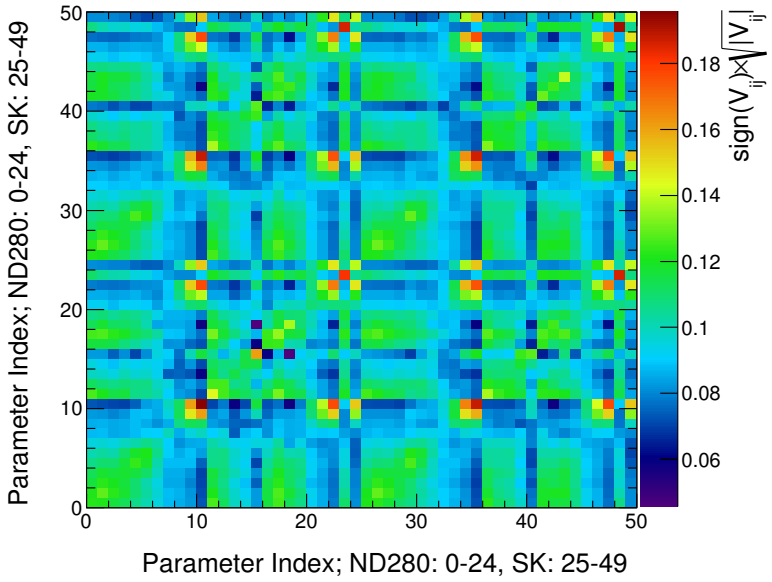

Figure 6.32.: Prior flux covariance matrix [84]. Paramers 0 to 24 are the ND280 flux normalisations for ν_μ, $\overline{\nu}_\mu$, ν_e, and $\overline{\nu}_\mathrm{e}$ in that order. Parameters 25 to 49 are the same for SK.

Detector systematic errors are also included in the fit. Since there are a large number of these parameters, the collective effect of all detector systematics is evaluated in terms of a covariance matrix of changes in $|\mathbf{p}_\mu|$-$\cos\theta_\mu$ bins for each of the three datasets [84]. These are produced by drawing a large number of random sets of the detector systematics, making the prediction for the bin contents in each histogram, and using the collection of all bin contents for each throw to make a covariance matrix. These matrices are included into the fit as an error on the data bin contents. A systematic is associated with each detector error bin, which are floated in the fit. The bin boundaries of the detector systematic covariance matrix are

- $|\mathbf{p}_\mu|$: 0.0, 0.3, 0.5, 0.6, 0.7, 1.0, 2.0, 30.0 GeV
- $\cos\theta_\mu$: -1.0, 0.85, 0.9, 0.94, 0.98, 1.0.

These are the same for the three data samples. There are 7 bins in $|\mathbf{p}_\mu|$ and 5 bins in $\cos\theta_\mu$, giving a total of 105 additional systematic parameters. The fractional errors for the three samples are shown in Figure 6.33.

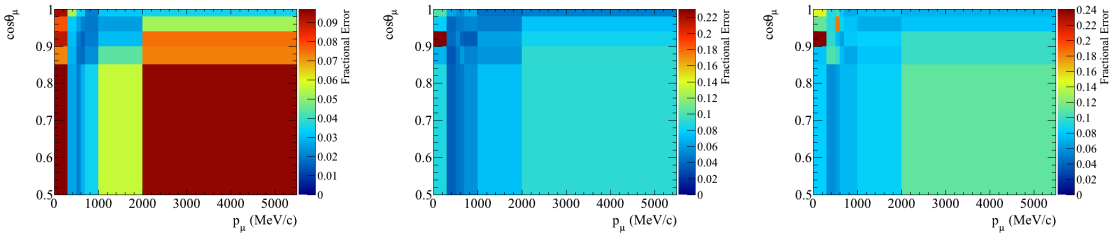

Figure 6.33.: Fractional errors from detector systematic and MC statistical errors for the CC0π (left), CC1π^+ (middle), and CCother (right) data samples [84].

Systematic errors associated with Monte Carlo statistics are included in the covariance matrices shown in Figure 6.33. These contribute an uncorrelated factor of $1/N_{\mathrm{MC}}$ in each $|\mathbf{p}_\mu|$ and $\cos\theta_\mu$ bin for each of the three samples (N_{MC} is the number of events expected in a given $|\mathbf{p}_\mu|$-$\cos\theta_\mu$ bin from the nominal MC prediction). This contribution is much smaller than the detector systematic errors.

Statistical errors for the data are included in the likelihood using the Poisson probability for the number of events in each bin. The likelihood for a Poisson distribution with N observed events and an expectation of λ is:

$$\begin{aligned} \mathcal{L}(N|\lambda) &= \frac{\lambda^N}{N!}e^{-\lambda} \\ \ln\mathcal{L}(N|\lambda) &= N\ln\lambda - \ln N! - \lambda \end{aligned} \tag{6.20}$$

When calculating the acceptance probability for a step in a Markov chain, we only care about the differences between two log-likelihoods with the same N and different λ, i.e. the expression

$$\ln\left[\frac{\mathcal{L}(N|\lambda)}{\mathcal{L}(N|N)}\right] = N - \lambda + N\ln\left(\frac{\lambda}{N}\right). \tag{6.21}$$

This amounts to an explicit expression of the data term in the likelihood of Equation 6.19 of:

$$\ln\left[P(d_{\mathrm{ND280}}|\vec{b},\vec{x},\vec{s})\right] = -\sum_i \left(N_i^p(\vec{b},\vec{x},\vec{s}) - N_i^d + N_i^d\ln\left[\frac{N_i^d}{N_i^p(\vec{b},\vec{x},\vec{s})}\right]\right) \tag{6.22}$$

where the index i runs over all bins in all samples, N_i^d is the number of data events in bin i, and $N_i^p(\vec{b},\vec{x},\vec{s})$ is the predicted number of events, which is a function of the beam, cross section and detector systematic parameters.

The nominal prediction for the number of events in each bin is produced by running the full ND280 MC simulation as detailed in Section 4.5, using the nominal parameters for all systematics. Subsequent predictions for non-nominal parameter sets are produced by calculating weights with either T2KReWeight or with the bespoke covariance matrix in the case of the detector systematic errors, then filling the appropriate histograms with each event weighted with the relative probability.

The initial position in the Markov chain is set by throwing one step from the nominal parameters according to $g(j|i)$ and forcing acceptance. The burn-in period is set to 2×10^4 steps, and 4×10^6 steps in total are performed to calculate the post-fit parameter estimates.

Post-fit parameter central values and widths are obtained for each parameter by marginalising over all other parameters in the post-fit Markov chain entries, then fitting a Gaussian to the data within 1 R.M.S of the mean. The central value is then the Gaussian mean, and the one sigma allowed region is the Gaussian width. This procedure ignores the non-Gaussian parts of the marginal probability, however the deviation of the marginalised Markov chain entries from a Gaussian distribution was observed to be small when using this fitter with the official T2K data.

Fitting T2K near-detector data with two models

Using the fitting procedure described in Section 6.5.2, two fits were performed. The first fit used as the MC prediction the 2p2h MC sample with pionless delta decay events weighted to zero. The second fit used the MC prediction from the 2p2h MC sample with 2p2h events weighted to zero, and pionless delta decay events given nominal weight.

The Markov chain fit was performed, and means and widths for each parameter were extracted from the marginalised Markov chain. Tables 6.2 to 6.4 show the best-fit values and uncertainties for ND280 flux, SK flux and cross section and FSI parameters respectively. These are shown graphically in Figures 6.34 to 6.36 for the flux (ND280 and SK), cross section and FSI parameters respectively.

The pionless delta decay normalisation parameter is fit for both MC sets, despite there being no contribution from these interactions in the 2p2h MC fit. The constraint on this parameter for this fit comes purely from the preconstraint on the parameter.

Number	Parameter name	with MEC	no MEC
0	ND280 ν_μ $0.0 < E_\nu < 0.4$ GeV	1.05 ± 0.09	1.04 ± 0.08
1	ND280 ν_μ $0.4 < E_\nu < 0.5$ GeV	1.04 ± 0.09	1.03 ± 0.09
2	ND280 ν_μ $0.5 < E_\nu < 0.6$ GeV	1.02 ± 0.08	1.01 ± 0.08
3	ND280 ν_μ $0.6 < E_\nu < 0.7$ GeV	1.00 ± 0.08	0.99 ± 0.08
4	ND280 ν_μ $0.7 < E_\nu < 1.0$ GeV	0.99 ± 0.08	0.98 ± 0.08
5	ND280 ν_μ $1.0 < E_\nu < 1.5$ GeV	1.00 ± 0.08	0.99 ± 0.08
6	ND280 ν_μ $1.5 < E_\nu < 2.5$ GeV	1.00 ± 0.07	1.00 ± 0.07
7	ND280 ν_μ $2.5 < E_\nu < 3.5$ GeV	1.06 ± 0.07	1.05 ± 0.07
8	ND280 ν_μ $3.5 < E_\nu < 5.0$ GeV	1.05 ± 0.07	1.06 ± 0.07
9	ND280 ν_μ $5.0 < E_\nu < 7.0$ GeV	0.95 ± 0.07	0.95 ± 0.07
10	ND280 ν_μ $7.0 < E_\nu < 30.0$ GeV	0.83 ± 0.06	0.83 ± 0.06
11	ND280 $\overline{\nu}_\mu$ $0.0 < E_\nu < 0.7$ GeV	1.04 ± 0.12	1.02 ± 0.11
12	ND280 $\overline{\nu}_\mu$ $0.7 < E_\nu < 1.0$ GeV	1.04 ± 0.10	1.03 ± 0.10
13	ND280 $\overline{\nu}_\mu$ $1.0 < E_\nu < 1.5$ GeV	1.01 ± 0.09	0.99 ± 0.09
14	ND280 $\overline{\nu}_\mu$ $1.5 < E_\nu < 2.5$ GeV	1.02 ± 0.10	1.01 ± 0.09
15	ND280 $\overline{\nu}_\mu$ $2.5 < E_\nu < 30.0$ GeV	0.94 ± 0.14	0.94 ± 0.13
16	ND280 ν_e $0.0 < E_\nu < 0.5$ GeV	1.03 ± 0.09	1.02 ± 0.09
17	ND280 ν_e $0.5 < E_\nu < 0.7$ GeV	1.03 ± 0.10	1.02 ± 0.09
18	ND280 ν_e $0.7 < E_\nu < 0.8$ GeV	1.08 ± 0.11	1.07 ± 0.11
19	ND280 ν_e $0.8 < E_\nu < 1.5$ GeV	1.02 ± 0.08	1.01 ± 0.08
20	ND280 ν_e $1.5 < E_\nu < 2.5$ GeV	1.03 ± 0.08	1.03 ± 0.07
21	ND280 ν_e $2.5 < E_\nu < 4.0$ GeV	0.99 ± 0.06	0.99 ± 0.06
22	ND280 ν_e $4.0 < E_\nu < 30.0$ GeV	0.86 ± 0.07	0.86 ± 0.06
23	ND280 $\overline{\nu}_e$ $0.0 < E_\nu < 2.5$ GeV	1.01 ± 0.16	1.01 ± 0.16
24	ND280 $\overline{\nu}_e$ $2.5 < E_\nu < 30.0$ GeV	0.90 ± 0.07	0.90 ± 0.07

Table 6.2.: Best-fit values and uncertainties for ND280 flux parameters in fits to T2K data with 2p2h and 2p2h without 2p2h MC samples. Best-fit values are defined as (1+fractional difference from nominal).

Number	Parameter name	with MEC	no MEC
25	SK ν_μ $0.0 < E_\nu < 0.4$ GeV	1.05 ± 0.09	1.04 ± 0.08
26	SK ν_μ $0.4 < E_\nu < 0.5$ GeV	1.04 ± 0.09	1.04 ± 0.09
27	SK ν_μ $0.5 < E_\nu < 0.6$ GeV	1.02 ± 0.08	1.02 ± 0.08
28	SK ν_μ $0.6 < E_\nu < 0.7$ GeV	1.00 ± 0.08	0.99 ± 0.08
29	SK ν_μ $0.7 < E_\nu < 1.0$ GeV	0.99 ± 0.09	0.98 ± 0.09
30	SK ν_μ $1.0 < E_\nu < 1.5$ GeV	1.01 ± 0.07	1.00 ± 0.08
31	SK ν_μ $1.5 < E_\nu < 2.5$ GeV	1.02 ± 0.07	1.02 ± 0.07
32	SK ν_μ $2.5 < E_\nu < 3.5$ GeV	1.05 ± 0.06	1.05 ± 0.06
33	SK ν_μ $3.5 < E_\nu < 5.0$ GeV	1.05 ± 0.07	1.06 ± 0.07
34	SK ν_μ $5.0 < E_\nu < 7.0$ GeV	0.92 ± 0.07	0.93 ± 0.07
35	SK ν_μ $7.0 < E_\nu < 30.0$ GeV	0.83 ± 0.07	0.83 ± 0.07
36	SK $\overline{\nu}_\mu$ $0.0 < E_\nu < 0.7$ GeV	1.04 ± 0.10	1.02 ± 0.10
37	SK $\overline{\nu}_\mu$ $0.7 < E_\nu < 1.0$ GeV	1.02 ± 0.09	1.00 ± 0.09
38	SK $\overline{\nu}_\mu$ $1.0 < E_\nu < 1.5$ GeV	1.02 ± 0.09	1.01 ± 0.09
39	SK $\overline{\nu}_\mu$ $1.5 < E_\nu < 2.5$ GeV	1.02 ± 0.11	1.00 ± 0.10
40	SK $\overline{\nu}_\mu$ $2.5 < E_\nu < 30.0$ GeV	0.98 ± 0.11	0.97 ± 0.10
41	SK ν_e $0.0 < E_\nu < 0.5$ GeV	1.06 ± 0.10	1.05 ± 0.10
42	SK ν_e $0.5 < E_\nu < 0.7$ GeV	1.05 ± 0.09	1.04 ± 0.09
43	SK ν_e $0.7 < E_\nu < 0.8$ GeV	0.98 ± 0.11	0.97 ± 0.11
44	SK ν_e $0.8 < E_\nu < 1.5$ GeV	1.02 ± 0.07	1.02 ± 0.07
45	SK ν_e $1.5 < E_\nu < 2.5$ GeV	1.02 ± 0.07	1.02 ± 0.07
46	SK ν_e $2.5 < E_\nu < 4.0$ GeV	0.97 ± 0.06	0.98 ± 0.06
47	SK ν_e $4.0 < E_\nu < 30.0$ GeV	0.86 ± 0.07	0.86 ± 0.07
48	SK $\overline{\nu}_e$ $0.0 < E_\nu < 2.5$ GeV	1.01 ± 0.17	1.01 ± 0.17
49	SK $\overline{\nu}_e$ $2.5 < E_\nu < 30.0$ GeV	0.90 ± 0.08	0.90 ± 0.07

Table 6.3.: Best-fit values and uncertainties for SK flux parameters in fits to T2K data with 2p2h and 2p2h without 2p2h MC samples. Best-fit values are defined as (1+fractional difference from nominal).

Number	Parameter name	with MEC	no MEC
50	$M_{\mathrm{A}}^{\mathrm{QE}}$	1.00 ± 0.06	1.00 ± 0.05
51	M_{A}^{res}	0.79 ± 0.06	0.77 ± 0.05
52	CC other shape $(*)$	0.30 ± 0.26	0.30 ± 0.25
53	Spectral function $(*)$	0.38 ± 0.15	0.35 ± 0.14
54	E_b	1.34 ± 0.22	1.26 ± 0.23
55	p_F	1.31 ± 0.05	1.27 ± 0.05
56	π-less Δ decay $(*)$	0.06 ± 0.16	0.14 ± 0.08
57	CCQE norm. $0.0 < E_\nu < 1.5$ GeV	0.93 ± 0.07	0.98 ± 0.07
58	CCQE norm. $1.5 < E_\nu < 3.5$ GeV	1.01 ± 0.10	1.01 ± 0.11
59	CCQE norm. $E_\nu < 3.5$ GeV	0.86 ± 0.10	0.83 ± 0.12
60	CC1π norm. $0.0 < E_\nu < 2.5$ GeV	1.04 ± 0.16	1.21 ± 0.17
61	CC1π norm. $E_\nu < 2.5$ GeV	1.16 ± 0.19	1.31 ± 0.18
62	CC coherent norm.	0.50 ± 0.15	0.51 ± 0.15
63	NC1π^0 norm.	0.98 ± 0.25	1.11 ± 0.24
64	NC1$\pi^\pm$ norm.	1.11 ± 0.29	1.09 ± 0.30
65	NC coherent norm.	0.97 ± 0.30	1.00 ± 0.29
66	NC other norm.	1.29 ± 0.21	1.25 ± 0.21
67	ν_μ/ν_{e} ratio	1.00 ± 0.03	1.00 ± 0.03
68	$\overline{\nu}_{\mathrm{e}}$ ν_μ ratio	0.91 ± 0.34	0.86 ± 0.35
69	2p2h norm.	1.00 ± 0.00	0.00 ± 0.00
70	FSI (low p_π inelastic scattering) $(*)$	-0.19 ± 0.14	-0.19 ± 0.13
71	FSI (high p_π inelastic scattering) $(*)$	0.23 ± 0.22	0.26 ± 0.20
72	FSI (π production) $(*)$	-0.33 ± 0.31	-0.37 ± 0.29
73	FSI (π absorption) $(*)$	-0.02 ± 0.26	-0.10 ± 0.26
74	FSI (low p_π charge exchange) $(*)$	-0.01 ± 0.40	-0.01 ± 0.39
75	FSI (high p_π charge exchange) $(*)$	-0.18 ± 0.17	-0.20 ± 0.16

Table 6.4.: Best-fit values and uncertainties for cross section and FSI parameters in fits to T2K data with 2p2h and 2p2h without 2p2h MC samples. Parameters marked with $(*)$ have a nominal value of zero, with the best-fit value showing fractional difference from nominal. All others are defined as (1+fractional difference from nominal).

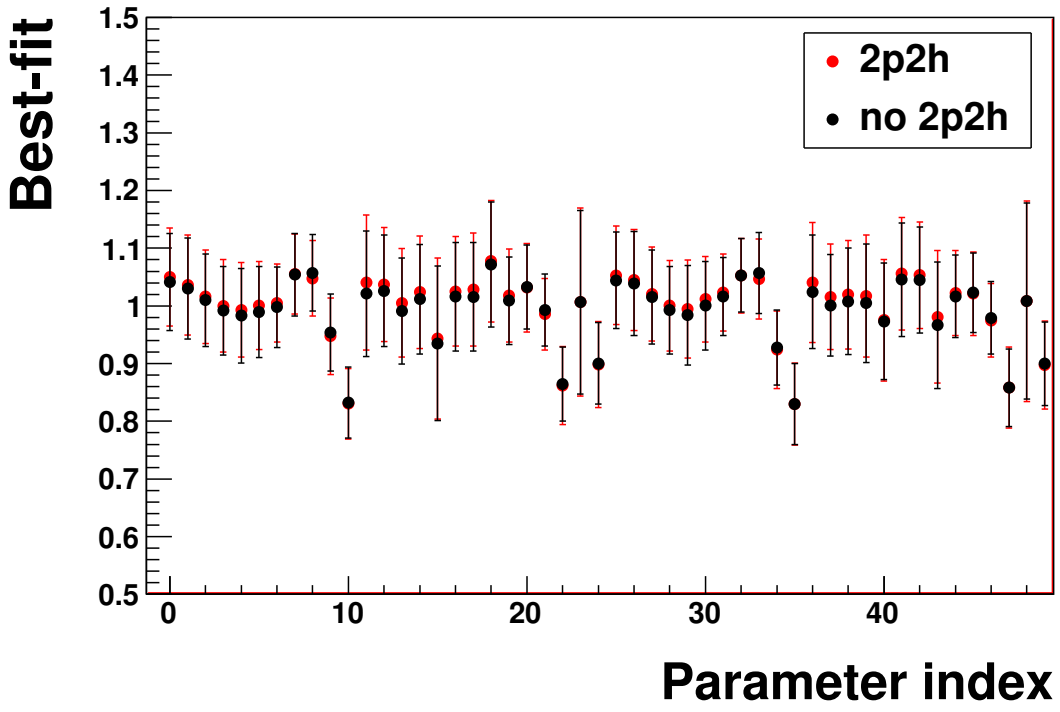

Figure 6.34.: Best-fit values and uncertainties of ND280 and SK flux parameters.

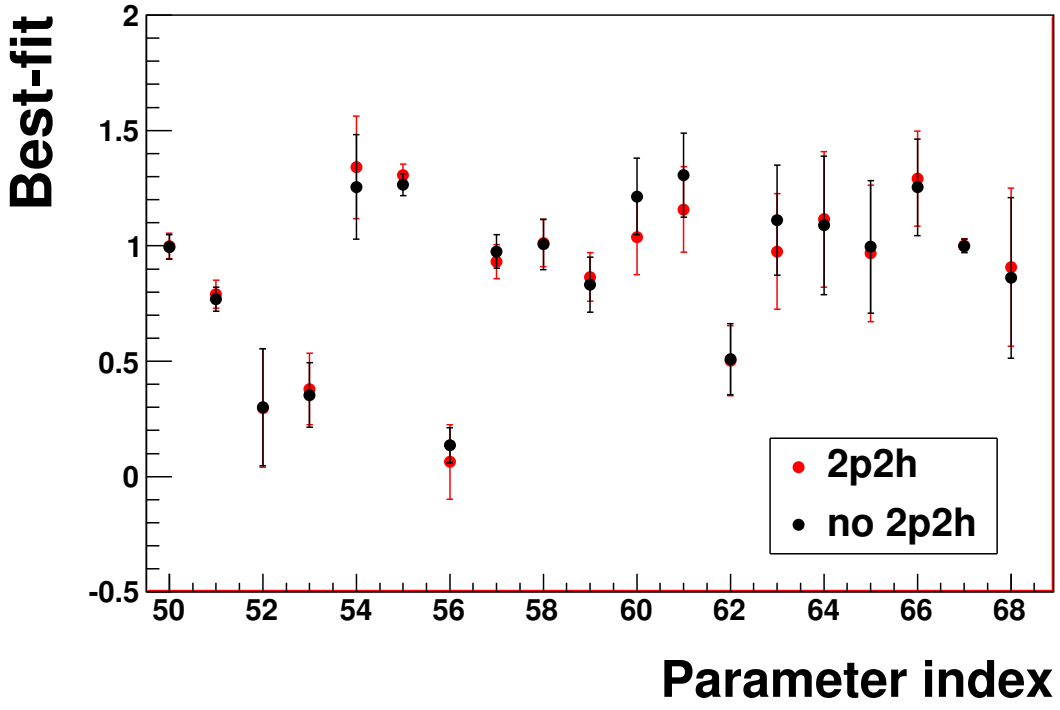

Figure 6.35.: Best-fit values and uncertainties of cross section parameters.

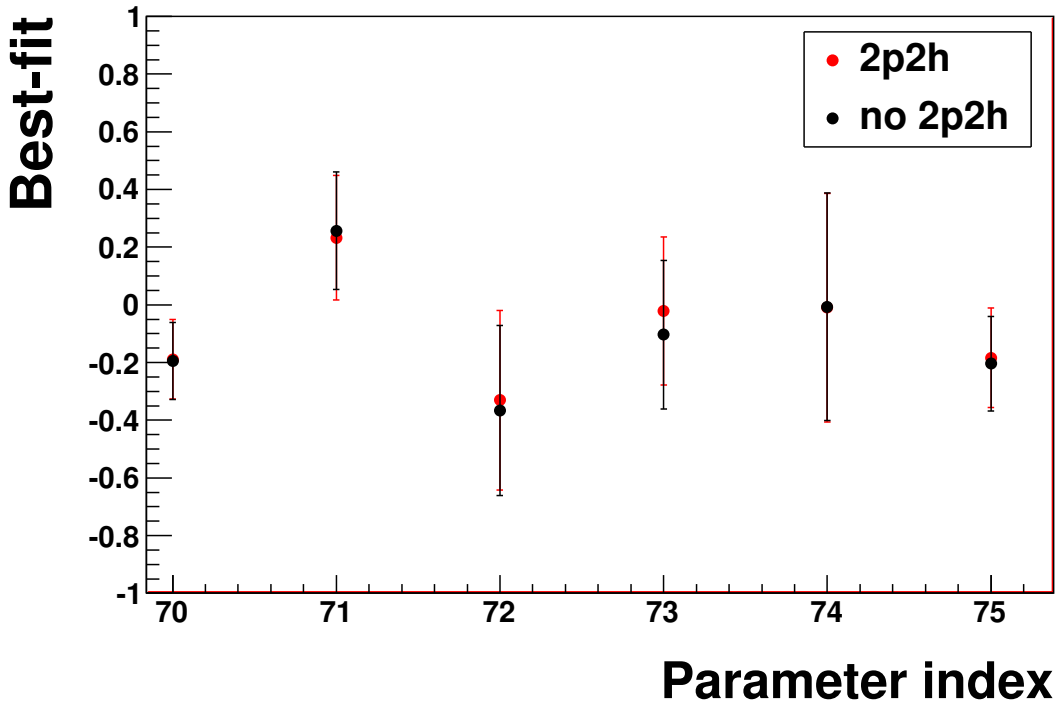

Figure 6.36.: Best-fit values and uncertainties of FSI parameters.

The differences in the best-fit neutrino flux between the two fits are overall very small. All differences are not large compared to the uncertainty on the datapoints, which comes mostly from the statistical error of the data. The small differences in the best-fit fluxes do show some general features. The best-fit flux for the MC including 2p2h events tends to be higher than that for the MC excluding 2p2h. This trend reverses for the high-energy ν_μ and ν_e flux. The SK flux is constrained by its correlation to the ND280 flux, so the same trends are observed in both the ND280 and SK best-fit fluxes.

The best-fit value of M_A^{QE}, shown as parameter 50 in Figure 6.35, has the same best-fit value for both fits. This is not an unexpected outcome: although the full neutrino interaction of Nieves *et al.* is able to describe the MiniBooNE data with a best-fit value of $M_A^{QE} \approx 1$, their model contains a number of differences from the NEUT model, most notably a different nuclear model for the CCQE mode (local Fermi-gas as opposed to global) and a full implementation of the random phase approximation (essentially modelling long-range correlations between nucleons). Recent developments in the NEUT CCQE model will soon include an implementation of the random phase approximation, and the present analysis would benefit from inclusion of this effect.

Parameter 51 in Figure 6.35 is M_A^{res}. The best-fit value for this parameter is slightly higher for the MC sample including 2p2h showing a slight preference for higher Q^2 resonant events, though the difference is small. This parameter is anti-correlated with the pionless delta decay parameter, which also increases the normalisation of the resonant events. Parameters 54 and 55 are the Fermi-gas parameters, E_b and p_F respectively. These both show higher best-fit values in the fits including 2p2h. Parameter 56 scales the pionless delta decay mode normalisation. As the pionless delta decay events are excluded from the 2p2h sample, the constraint in this fit comes purely from the pre-constraint. The best-fit is different from nominal due to the limited number of Markov chain steps. For the sample excluding 2p2h, the best-fit value is higher than nominal showing a preference for more pionless delta decay events. This is effectively a shift of events from the CC0π to the CC1π^+ samples. Parameter 57 is the normalisation of the CCQE mode for $E_\nu < 1.5$ GeV. The fit value for the 2p2h sample is lower, since most multinucleon neutrino events are selected into the CC0π sample. Parameters 60 and 61 are normalisations for the resonant CC1π modes. These are higher for the MC fit excluding multinucleon neutrino interactions, and is probably anti-correlated with the pionless delta decay parameter.

The best-fits for the FSI parameters are very similar for both fits, with the largest difference being in the pion absorption parameter. Again, this parameter transfers events between the CC0π and CC1π^+ samples.

Figures 6.37 to 6.39 show the best-fit muon momentum and muon–neutrino opening angle spectra for the two fits, compared with their nominal spectra and the nominal spectra from the official T2K MC. The two post-fit spectra are effectively identical, showing that both models—before and after the addition of the multinucleon neutrino mode—offer very similar descriptions of the T2K near-detector data. There are a large number of parameters in the fits, and in the present parameterisation, a large degree of flexibility in them, which makes a good fit to the data easy for the fitter to achieve. Predictions outside the kinematic reach of the data are not necessarily the same, and we should be cautious extrapolating the predictions to broader areas of phase-space.

The obvious next step in this analysis would be to extrapolate the best-fit parameters to predictions for expected numbers of events in the far-detector, then fit the oscillation parameters to the new far-detector spectrum. Currently this is not possible because the far-detector simulation has not been run with a version of NEUT containing 2p2h events. This should be done in the near future, as it would certainly benefit the oscillation analysis to know the size of the effect of 2p2h events, and to be able to account for them.

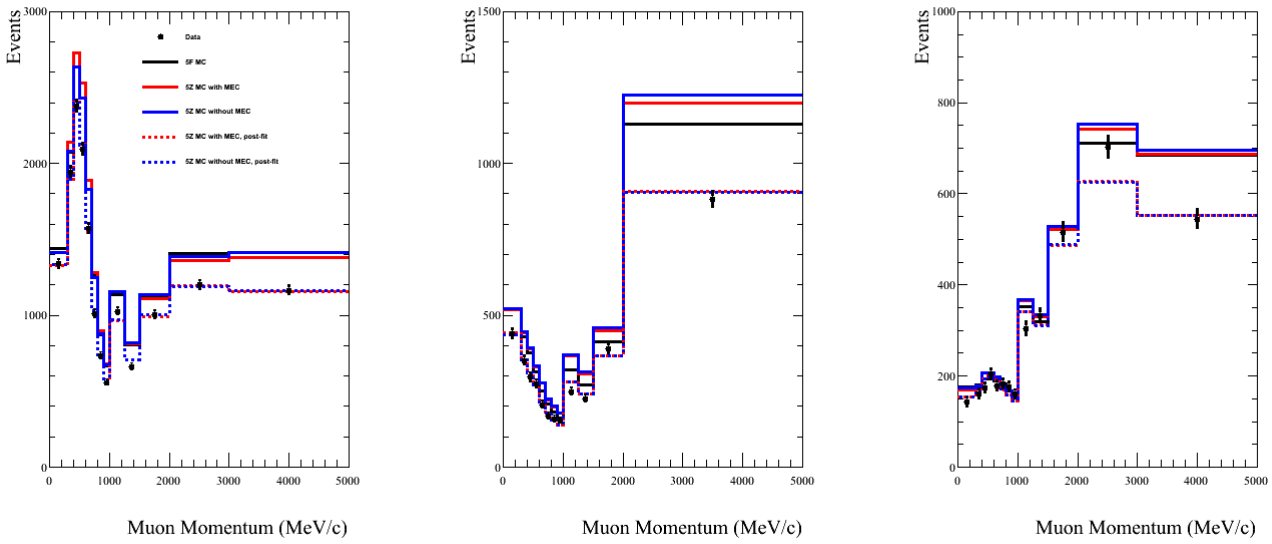

Figure 6.37.: Reconstructed muon momentum distributions for data periods 1–4. Official pre-fit T2K prediction (black), pre-fit prediction of 2p2h MC (blue solid), pre-fit prediction of 2p2h MC excluding 2p2h events (red solid), best-fit spectrum from 2p2h MC fit (blue dashed) and best-fit spectrum from 2p2h MC excluding 2p2h events (red dashed). The three selections are shown separately: CC0π (left), CC1π^+ (middle), and CCother (right).

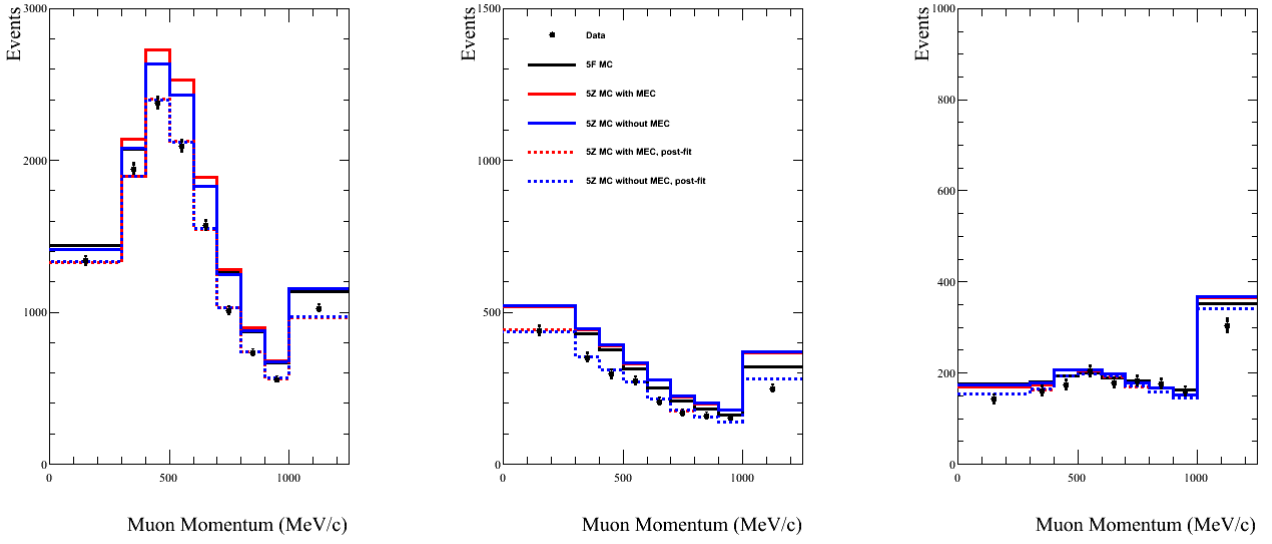

Figure 6.38.: Low momentum part of the muon momentum distributions of Figure 6.37.

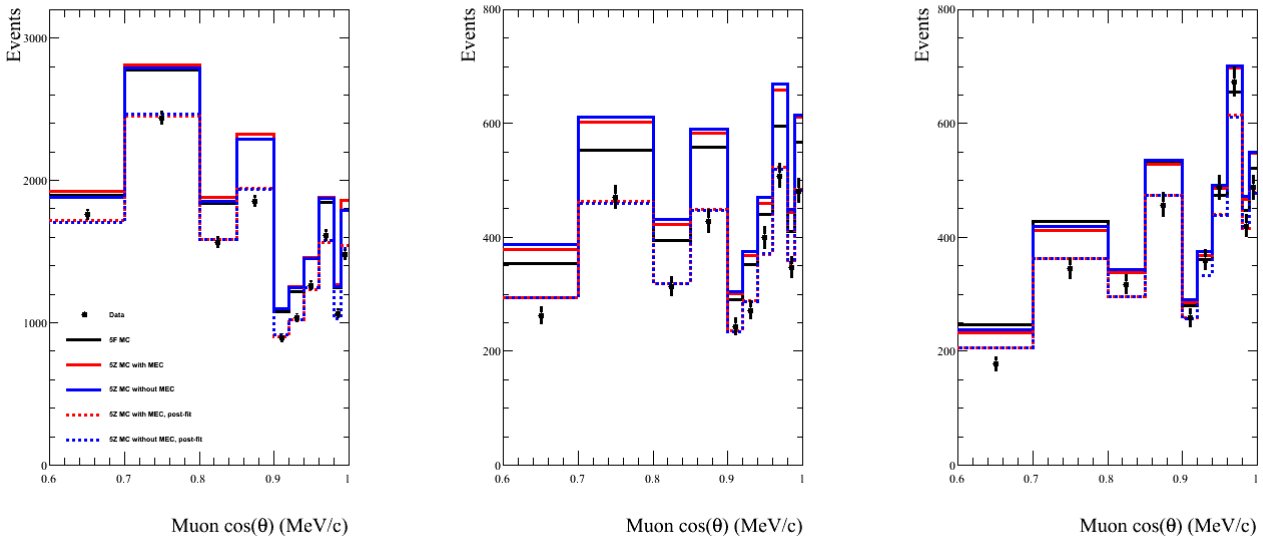

Figure 6.39.: Expected distributions for neutrino–muon opening angle for data periods 1–4. Official pre-fit T2K prediction (black), pre-fit prediction of 2p2h MC (blue solid), pre-fit prediction of 2p2h MC excluding 2p2h events (red solid), best-fit spectrum from 2p2h MC fit (blue dashed) and best-fit spectrum from 2p2h MC excluding 2p2h events (red dashed). The three selections are shown separately: CC0π (left), CC1π^+ (middle), and CCother (right).

Although the differences in best-fit values between the two fits shown here are modest, there may be an additional effect on oscillation parameters due to the differences in energy reconstruction between multinucleon neutrino interactions and CCQE events.

6.5.3. Goodness-of-fit of NEUT models to T2K data

It is essential for the integrity of the oscillation results reported by T2K that the interaction model used in the analysis is able to accurately predict observations in the near-detector. If this is not the case, we can not be sure that deviation from the 'no oscillation' prediction and the far-detector data are due to neutrino oscillations, and could be due to the mis-modelling of neutrino interactions.

To test whether the NEUT model including multinucleon neutrino interactions is a good description of neutrino interactions in the absence of oscillation, we can perform a goodness-of-fit test to compare the model with near-detector data (it is assumed that no oscillation occurs between the neutrino source and the near detector). To this end a Bayesian goodness-of-fit test is performed to compare the NEUT prediction with and without the multinucleon neutrino interaction mode to the near-detector data. The goodness-of-fit for the two models are compared to test whether the addition of multinucleon neutrino interactions into NEUT improves the description of the data.

Bayesian goodness-of-fit

The method chosen to compare the goodness-of-fit of the models to the data is the posterior predictive assessment method of Gelman *et al.* [85]. Unlike classical goodness-of-fit tests based on the minimum χ^2, this method takes into account the whole joint posterior prediction of the model parameters, so better includes the effects of non-linear parameter predictions and correlations. Further, calculating the posterior predictive assessment in practice is a simple and natural extension from a Markov chain Monte Carlo parameter estimation.

It is useful to first illustrate a classical goodness-of-fit test, then show how this relates the Bayesian version. Define y to be the data collected in some experiment, H is a model, θ is a d-dimensional set of model parameters, T is a test statistic (e.g. a χ^2), and $A(y)$ is a set of auxiliary statistics which stay the same in repetitions of the experiment (e.g. sample size, time). Finally, define y^{rep} to be data that would appear if the experiment

was replicated with the same H, θ and $A(y)$. The reference distribution for y^{rep} is $P_A(y^{\text{rep}}|H,\theta)$, where the subscript A indicates that $A(y^{\text{rep}}) = A(y)$ (i.e. the hypothetical replicated experiment is exactly the same as the original one). The classical p-value is calculated from:

$$p_c(y,\theta) = P_A(T(y^{\text{rep}}) \geq T(y)|H,\theta). \tag{6.23}$$

where T is defined in such a way that it is large for large fluctuations from a reasonable prediction of H and θ. This is calculated for fixed values of θ.

The output from a Bayesian parameter estimation is the posterior distribution of the parameters θ, denoted $P(\theta|H,y)$. The reference distribution for a replicated dataset is then:

$$P_A(y^{\text{rep}}|H,y) = \int P_A(y^{\text{rep}}|H,\theta)P(\theta|H,y)d\theta. \tag{6.24}$$

The test statistics, written $T(y)$ and $T(y^{\text{rep}})$ in the classical case, are now functions of the parameters θ as well as the data, so are written $D(y,\theta)$ and $D(y^{\text{rep}},\theta)$. In the terminology of Reference [85] these are called discrepancy variables. A p-value can be calculated by sampling y^{rep} from the reference distribution then locating $D(y,\theta)$ in the distribution of $D(y^{\text{rep}},\theta)$. This is expressed as:

$$p_b(y) = P_A(D(y^{\text{rep}},\theta) \geq D(y,\theta)|H,y). \tag{6.25}$$

This can be related directly to the classical p-value as:

$$p_b(y) = \int p_c(y,\theta)P(\theta|H,y)d\theta. \tag{6.26}$$

This quantity is referred to as the posterior predictive p-value. It allows comparison between observed data and the posterior of a model, rather than just the best-fit point.

This quantity is simple to calculate from a Markov chain, since the values of θ in the Markov chain are by construction a sample from $P(\theta|H,y)$. The p-value is calculated using the following method:

1. Sample n draws of θ from the Markov chain

2. Simulate replicated datasets for each draw (i.e. draw from $P_A(y^{\text{rep}}|H,\theta)$). For the T2K datasets, this is simply a Poisson fluctuation from the prediction of each θ in each data bin.

3. Calculate $D(y,\theta)$ and $D(y^{\text{rep}},\theta)$

4. Estimate $p_b(y)$ from $P(D(y^{\text{rep}},\theta) \geq D(y,\theta))$

It is also useful to plot $D(y,\theta)$ against $D(y^{\text{rep}},\theta)$ to see if the typical magnitudes of the two are similar.

The user of the method is free to choose the definition of D. A standard definition for a general comparison would be a χ^2 or a likelihood ratio. The definition of D used in the goodness-of-fit test for the near-detector data is the log of the likelihood ratio:

$$\begin{aligned} -D(\lambda,N) = \ln\left[\frac{\mathcal{L}(N|\lambda)}{\mathcal{L}(N|N)}\right] &= \ln\left[\frac{\frac{\lambda^N}{N!}e^{-\lambda}}{\frac{N^N}{N!}e^{-N}}\right] \\ &= \ln\left[\frac{\lambda^N}{N^N}e^{N-\lambda}\right] \\ &= N-\lambda+N\ln\frac{\lambda}{N} \end{aligned} \tag{6.27}$$

This is the same as the data-term of the likelihood used in the Markov chain Monte Carlo parameter fitter. Variations of the systematic parameters are not included in the goodness-of-fit metric, since the parameter posteriors are taken into account automatically when sampling from $P(\theta|H,y)$.

A toy MC study was performed to understand and validate the properties of this goodness-of-fit method, and is described in Apprendix A. It was found that the posterior predictive assessment method enabled good discrimination between correct and incorrect models, so could be used for the T2K data fits.

Bayesian goodness-of-fit using T2K near-detector data

Using the Markov chains from the fits to T2K data with the 2p2h MC, the posterior predictive assessment was performed. Predictions for expected numbers of events in each data bin were produced from 5×10^3 samples from the parameter sets in the Markov chain. Replicated datasets, y^{rep} for each of these expectations were created by drawing from a Poisson distribution in each data bin, with the mean set to the expected bin content. Using these replicated datasets, the posterior predictive model assessment described in

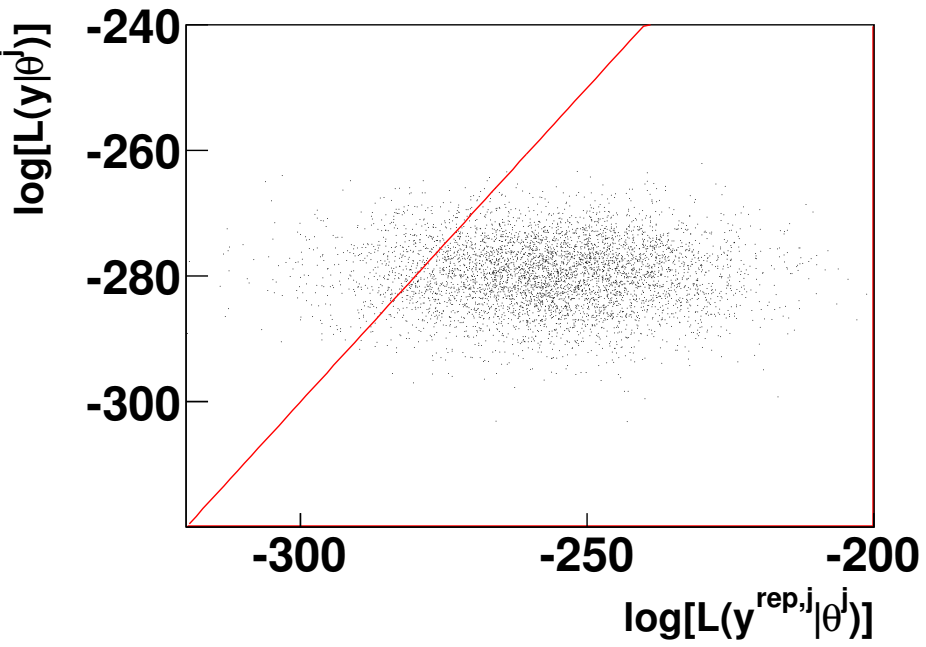

Figure 6.40.: Discrepancy variable for the data (y-axis) against the discrepancy variable for the replicated data (x-axis) using the Markov chain from the fit with the full 2p2h simulation (including multinucleon neutrino interactions, excluding pionless delta decay). The red line shows the line of $y = x$. There are a significant number of points with $y > x$, showing reasonable agreement between the MC and the data.

Section 6.5.3 was performed. The discrepancy variable was defined as in Equation 6.27, summed over all bins in the three datasets.

Figure 6.40 shows a plot of the discrepancy variable for the data against the discrepancy variable for the replicated datasets for the Markov chain from the fit with the full 2p2h MC. Each point on this plot shows the discrepancy variable calculated for a unique draw of the fitted parameters from the Markov chain, θ_j, comparing this throw with the T2K data for the y-axis value, and with a replicated data-set (i.e. fake-data drawn from the prediction of the model with parameters θ_j) for the x-axis value. The p-value is the fraction of throws which result in a higher discrepancy variable for the data given the parameters than the fake-data given the parameters. This is visualised by the fraction of points above the line of $y = x$. For the fit with the full 2p2h MC, the p-value is 0.1188 ± 0.0003. The uncertainty is from the limited number of replications. Figure 6.41 shows a plot of the same variables for the fit using the 2p2h MC excluding 2p2h events. The p-value for this sample is 0.1136 ± 0.0002.

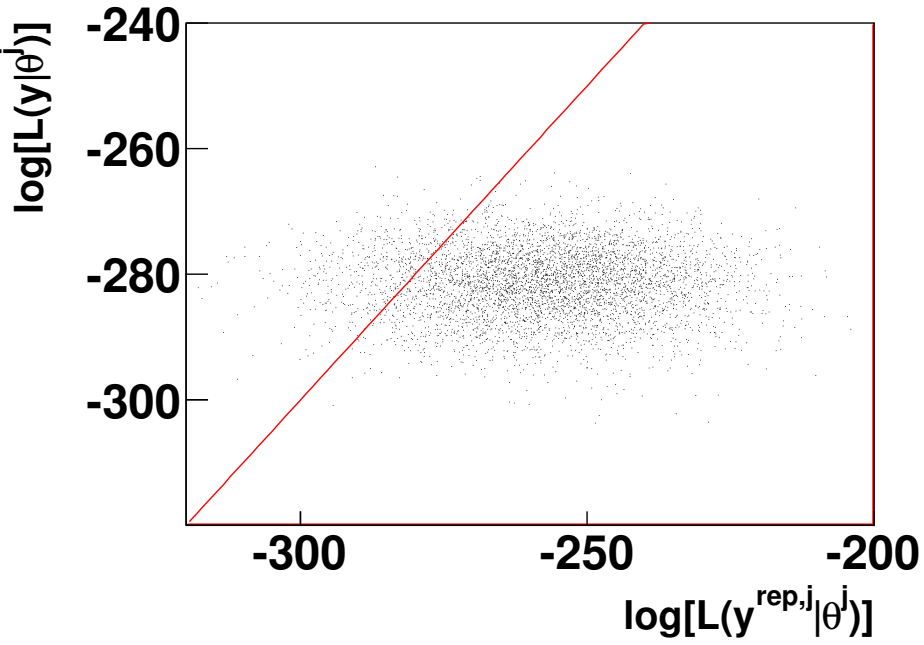

Figure 6.41.: Discrepancy variable for the data (y-axis) against the discrepancy variable for the replicated data (x-axis) using the Markov chain from the fit with the 2p2h MC without 2p2h events (including pionless delta decay events). The red line shows the line of $y = x$. There are a significant number of points with $y > x$, showing reasonable agreement between the MC and the data.

The difference between the two p-values is small, showing that both models have comparable agreement between themselves and the T2K data. The values themselves show a good fit, certainly not small enough to indicate a major discrepancy between the fitted models and the data. This result is unsurprising: there are a large number of parameters in the fit, many of which were introduced in order to ensure agreement between the MC and the data, so that deviations from the no-oscillation expectation can be confidently attributed to the effect of neutrino oscillations rather than mismodelled neutrino interactions. The good p-values show that this procedure has been successful.

This work shows the first comparison between the T2K data and an interaction model which includes multinucleon neutrino interactions, and the interaction model implemented is a significant update to the model of the NEUT generator. A number of refinements to this analysis are possible which will enable a more rigorous test of the model itself. The T2K data selections described in this work are not an ideal testbed for this model. Notably, the phase-space which is sampled by the selections is small compared to the phase-space populated by the products of the interaction model, and there are significant differences in the high Q^2 predictions of the NEUT model with multinucleon neutrino interactions and, for example, the previous NEUT model with a high value of M_{A}. Enlarging the phase-space by inclusion of higher-angle muon tracks into the selections would add significant power to the T2K samples, though this is not simple given the geometry of the T2K near-detector. More preferable still would be the development of a specific selection of multinucleon neutrino events, triggering on multiple particle tracks and tailored for this interaction mode. This is particularly important given the wide variety of predictions by different multinucleon neutrino interaction models.

Chapter 7.

Conclusion

T2K is one of the world's flagship neutrino oscillation experiments. The experiment has produced several world-leading measurements of oscillation parameters, with more powerful results expected as the dataset increases. While still statistics-limited, there is significant focus on reduction of systematic errors, including those associated with neutrino interactions. This is an essential component of the research program of T2K, ensuring the experiment can maximise the use of the data and produce results which are both interesting to the current neutrino physics community, and can also serve as a guide for the future direction in the field.

The work in this thesis has focussed on understanding the affects of neutrino interaction modelling, and improving the precision with which we can make our predictions.

Data from the MiniBooNE experiment was used to prepare a prior uncertainty on CCQE interaction parameters as an input to the T2K oscillation analyses. The predictions from the NEUT MC generator were fit to the MiniBooNE data, and best-fit parameters were found for $M_{\mathrm{A}}^{\mathrm{QE}}$ and the CCQE mode normalisation. Uncertainties on the best-fit values were very small due to the absence of correlation information between the MiniBooNE data points. The prior uncertainty on the CCQE parameters was taken as the difference between their NEUT nominal values and the values found by the fits, resulting in a weak constraint in the prior. Reweighting functionality was developed for the Fermi-gas parameters, p_F and E_b, to allow them to be included into the T2K oscillation analysis in a unified way with other cross section parameters.

The interaction model assumed by the T2K analyses, encoded in the NEUT MC generator, was updated to include a multinucleon neutrino interaction mode. The multinucleon neutrino interaction total cross section and muon double-differential cross

sections were predicted by Nieves *et al.* [42], and code was provided by the authors of the model to calculate the cross section for these events. This code was used to implement an MC simulation into NEUT. Hadron kinematics are not predicted by the model of Nieves, so they were included into the simulation using a method based on the method of Sobczyk for simulation of isotropic hadrons in multinucleon neutrino interactions [78]. Simulations for ν_μ, ν_e, $\overline{\nu}_\mu$, and $\overline{\nu}_\mathrm{e}$ on C^{12} and O^{16} were implemented into NEUT. The model was extensively validated, and was shown to be consistent with the theoretical predictions.

The updated NEUT model including multinucleon neutrino interactions was simulated in the T2K near-detector software, and a MC set comparable with the full T2K near-detector dataset (runs 1–4) was produced. Using a Markov chain Monte Carlo method employing the Metropolis-Hastings algorithm, the simulation was fit to the T2K data. Fits were performed with two MC configurations, once with all multinucleon neutrino interactions included and pionless delta decay events excluded, and once with multinucleon neutrino interactions excluded and pionless delta decay included. The latter was comparable with the previous NEUT model. Differences in best-fit parameters between the two configurations were found to be small.

A Bayesian goodness-of-fit method was employed to evaluate the quality of the fit of the two MC configurations to the T2K data. The method used the output of the Markov chain from the parameter fits. The p-values were found to be 0.1188 ± 0.0003 for the fit including multinucleon neutrino interactions and excluding pionless delta decay, and 0.1136 ± 0.0002 for the fit excluding multinucleon neutrino interactions and including pionless delta decay. Differences between predictions of observed muon kinematics at the best-fit point for the two MC fits were small.

Appendix A.

Toy Monte Carlo study of Bayesian Goodness-of-Fit Metric

Before using the posterior predictive assessment to compare NEUT to the T2K data, a toy Monte Carlo study was performed to understand and validate the properties of the method. The method of the study was to fit a simple model to data, and inspect the distribution of the p-value when this model is the true distribution of the data, and when it is not.

The toy experiment models measurement of a Gaussian parameter. The pdf of the data was defined as a Gaussian distribution with a mean of zero and a width of 0.2, and a normalisation of 500. The fake data were to be collected in 10 bins between -0.5 and 0.5, and the expected number of events in each bin was calculated by integrating the pdf within all bin boundaries. This is the definition of the true model, H. The fake-data, y, was generated by throws from a Poisson distribution in each bin, with the Poisson mean equal to the expected bin content in H. One fake data set is illustrated in Figure A.1.

Part of the definition of the model is a definition of the prior constraints on the parameters. The two parameters which were fit were the mean and width of the Gaussian. The prior of the mean was taken to be uniform between -2 and $+2$, and the prior of the width was taken to be a Gaussian distribution, centered on zero with a width of 0.05. These choices were made to ensure the constraint of the data was larger than the constraint of the priors. The prior constraints are illustrated in Figure A.2

The Metropolis-Hastings method for Markov chain parameter estimation was implemented to estimate the posterior probabilities of the mean and the width of the data. The start position of the Markov chain was chosen the be the true parameter values.

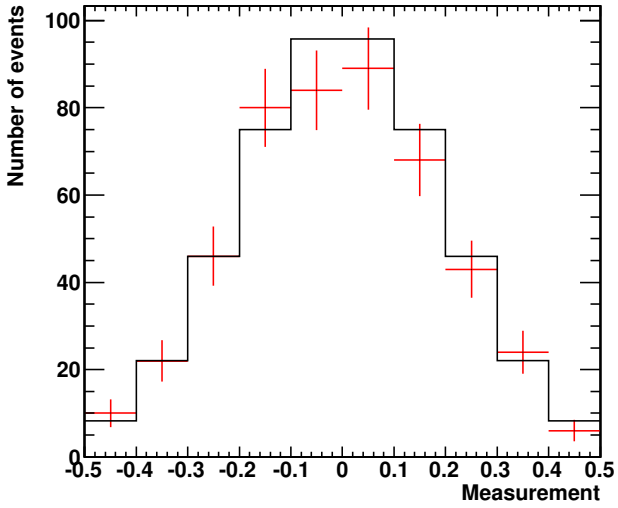

Figure A.1.: Expected distribution, H, of the toy MC model (black), and a simulated dataset y (red).

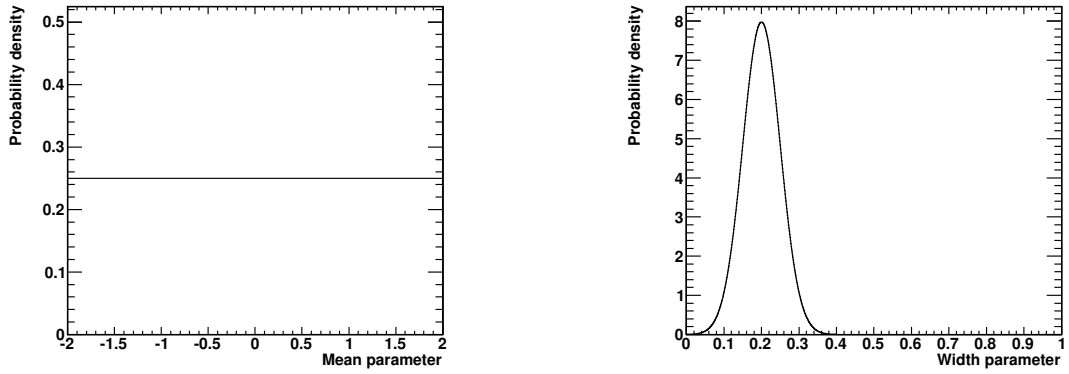

Figure A.2.: Prior constraint on the mean (left) and width (right) of the data in the toy MC experiment.

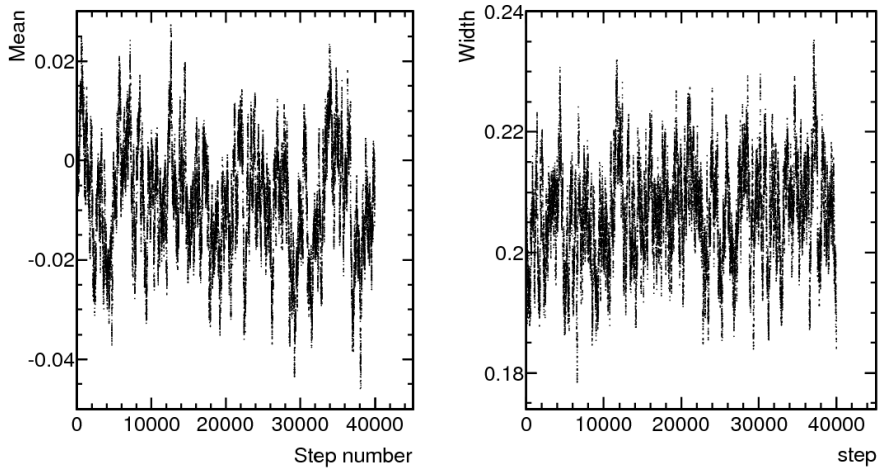

Figure A.3.: Entries in the Markov chain for the two fitted parameters: mean (left) and width (right) of the toy MC data.

4×10^4 steps were found to be sufficient to establish a good constrain of both parameters. The step size was chosen by trial-and-error to be 0.05 times the respective prior widths.

Figure A.3 shows the values of the two parameters at each step in the Markov chain. Figure A.4 shows the Markov chain entries in the joint parameter space, and marginalised over each variable. Gaussian fits to the marginal parameter entries yield estimates of the best-fit values and allowed regions of each parameter.

For this fit, the best-fit parameters were estimated to be:

- mean: 0.008 ± 0.011
- width: 0.207 ± 0.008

These are consistent with the true parameter values in the model. The χ^2 of the Gaussian fits to the marginal posteriors are very high showing that the distribution of points it not exactly Gaussian. The reason for this can be seen in the 2D joint posterior plot in Figure A.4: the steps in the joint parameter space tend to form clusters which indicate the step size is too small (or the number of Markov chain entries is too few). Nevertheless, the Gaussian fits are good enough for the purpose of this study.

Following the steps described in Section 6.5.3, all parameter sets in the Markov chain, θ_j, were sampled and a prediction was made for event distributions for each j. For each j, a set of replicated data, y^{rep} was produced by generating Poisson fluctuations

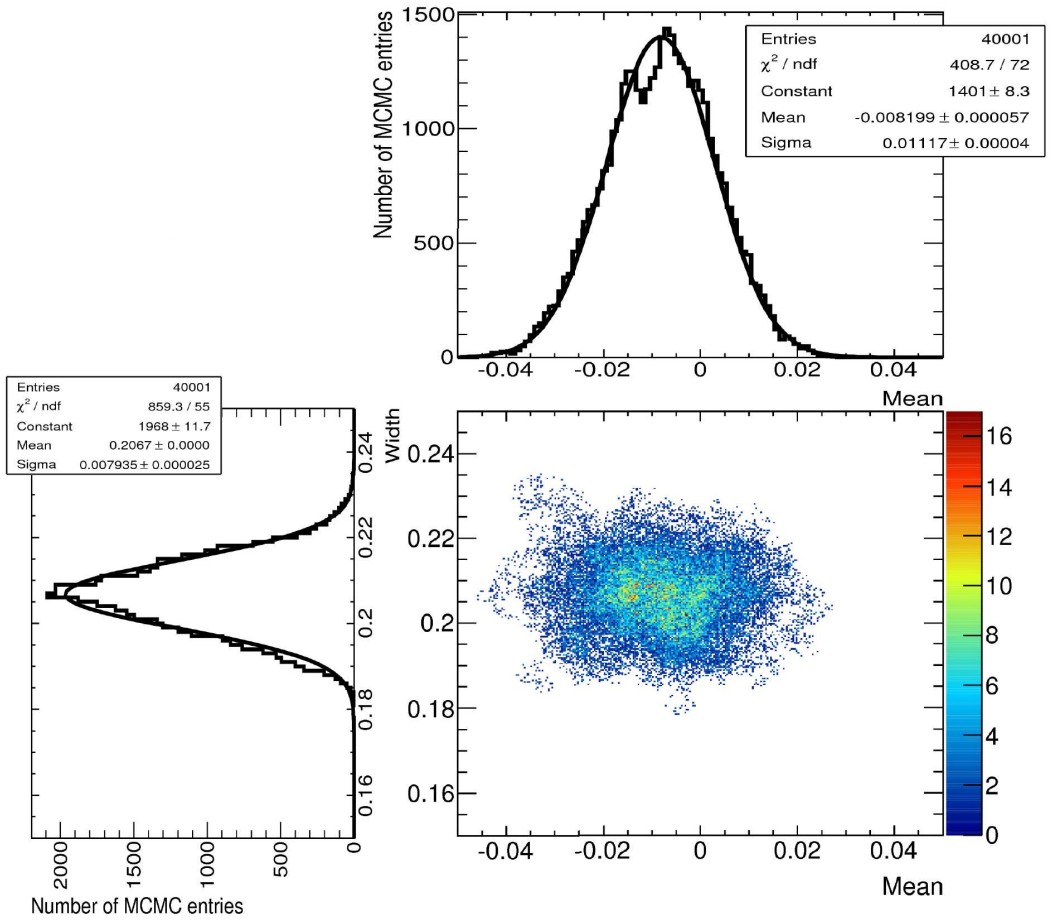

Figure A.4.: All entries in the Markov chain, plotted together (2D, center) and shown marginalised over width (top) and marginalised over mean (left).

around each bin entry. Next, for each j, $D(y, \theta_j)$ and $D(y^{\text{rep}}, \theta_j)$ were calculated using the definition in Equation 6.27.

Figure A.5 shows a plot of $-D(y^{\text{rep}}, \theta_j)$ against $-D(y, \theta_j)$ for each j. A clear maximum can be seen in $-D(y, \theta_j)$, which occurs at the best-fit θ: there is a limit to how good the fit can get given fixed data. No such limit is seen in $-D(y^{\text{rep}}, \theta_j)$ since each replicated dataset is different. From the number of entries with $D(y^{\text{rep}}, \theta_j) \geq D(y, \theta_j)$, $p_b(y)$ can be estimated as $p_b(y) = 0.7853$ for this toy dataset. This value is far from zero, indicating the model is a good description of the data. This is expected, since the data was drawn from exactly the model which was fit.

To inspect the properties of the p-value itself, the toy MC study was repeated using 10^4 different toy datasets y. $p_b(y)$ was calculated for each. Figure A.6 shows histogram of $p_b(y)$ in each toy MC experiment. The plot shows a strong deviation from uniform,

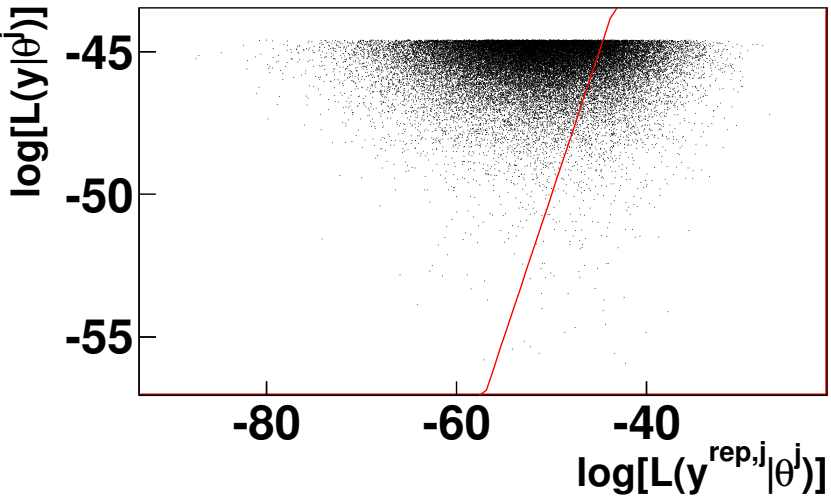

Figure A.5.: Scatter plot of $-D(y^{\text{rep}}, \theta_j$ (x-axis) against $-D(y, \theta_j)$ (y-axis) for each j. The red line is at $D(y^{\text{rep}}, \theta_j) = D(y, \theta_j)$ allowing a by-eye estimate of the p-value.

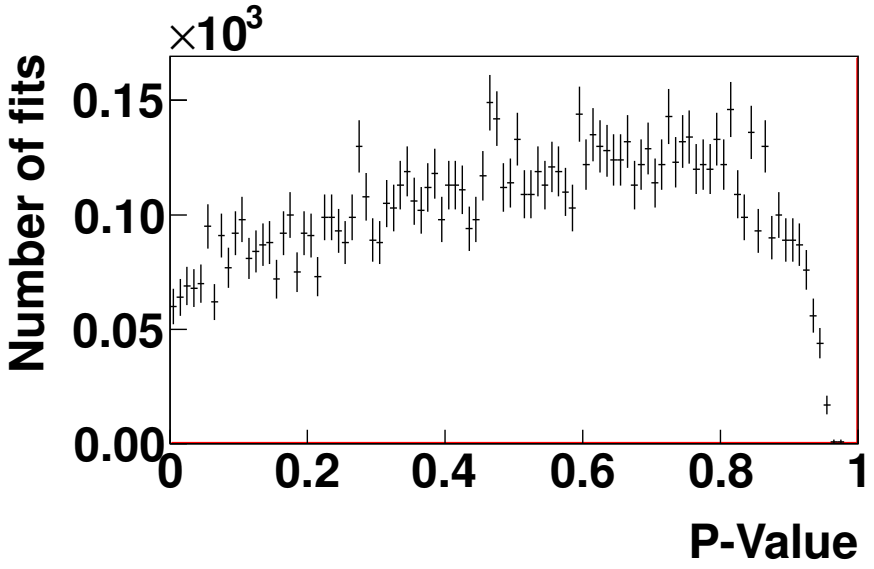

Figure A.6.: Histogram of all p-values for 10^4 repetitions of the toy MC study.

with a significant deficit towards $p_b = 1$, as well as significant slope. The reason for this was suspected to be that the toy MC data had relatively low statistics, and low numbers of bins, leading to a quantification effect: toy datasets with different distributions may appear the same when events are binned.

To test this hypothesis, the entire study was performed again, but with an expectation of 2×10^3 events, and with events divided into 100 bins. Figure A.7 shows an example toy

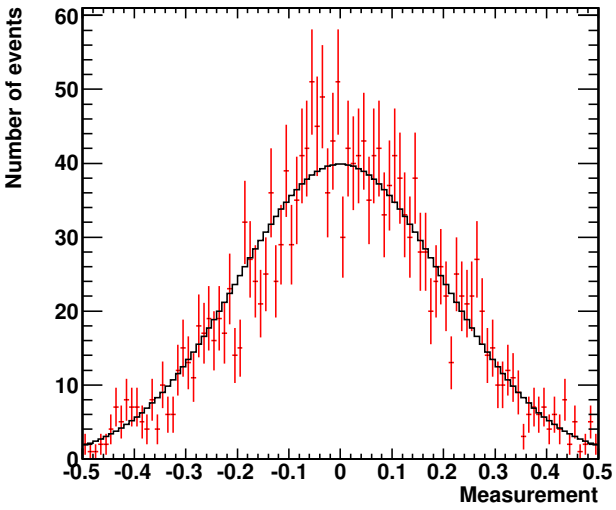

Figure A.7.: Expected distribution, H, of the toy MC model with 2×10^3 events and events divided into 100 bins (black), and a simulated dataset y (red).

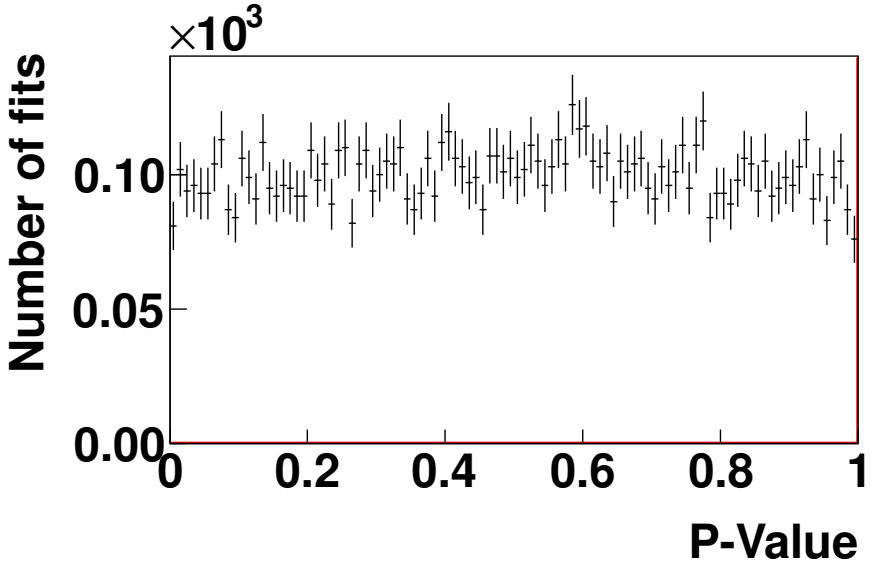

Figure A.8.: Histogram of all p-values for 10^4 repetitions of the toy MC study with 2×10^3 events, and with events divided into 100 bins.

MC dataset. As before, the p-value was calculated from 10^4 Markov chains with different y. A histogram of the p-values is shown in Figure A.8. The distribution of p-values now appears uniform, showing that the test-statistic is good as long as the measurement has sufficient resolution.

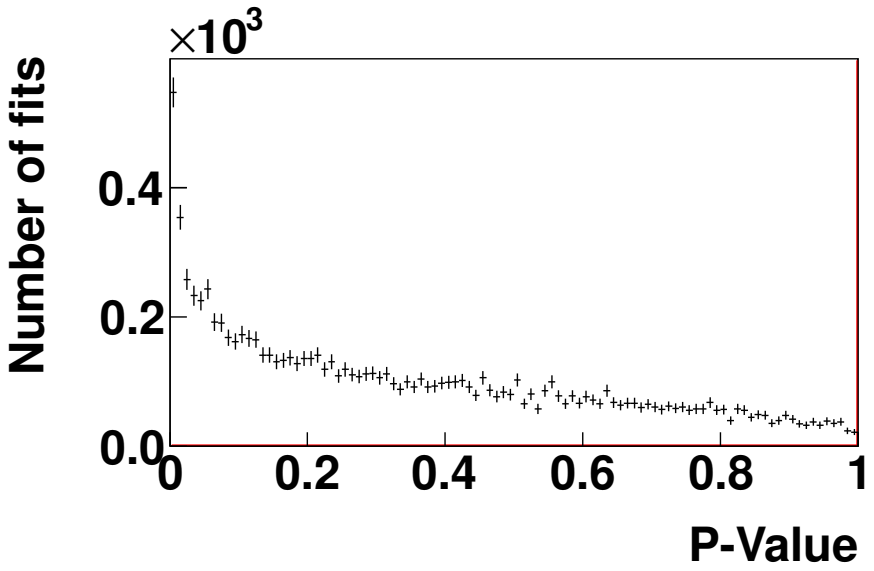

Figure A.9.: Histogram of all p-values for the toy MC fit in which the data y and the repeated data y^{rep} are drawn from different distributions.

For the final part of the study, the p-value distribution is inspected when the wrong model is fit to the data. The study was carried out in exactly the same way as the previous study with 2×10^3 events and 100 bins, however after the dataset had initially been chosen, the value of the 50^{th} bin was multiplied by 1.5. The model H was kept as the Gaussian without the modification, so the model used in both the parameter estimation and the goodness-of-fit test were slightly different to the one from which the toy MC data were drawn, and slightly different from the distribution of y^{rep}.

The distribution of p-values from these fits are shown in Figure A.9. There is a clear tendency towards lower values, showing that this test can successfully discriminate between good and bad fits to data. The preference here is not large since the distribution from which the data were drawn and the model are very similar. For larger differences, the tendency towards $p_b(y)$ will be more pronounced.

The properties of the posterior predictive assessment investigated in these studies show good behaviour when fitting the correct model, and also show discrimination between correct and incorrect models.

Bibliography

[1] Carlo Giunti and Chung W. Kim. *Fundamentals of Neutrino Physics and Astrophysics*. 2007.

[2] B. Kayser, F. Gibrat-Debu, and F Perrier. *The Physics of Massive Neutrinos*. 1989.

[3] R. Davis, D. S. Harmer, and K. C. Hoffman. Search for Neutrinos from the Sun. *Phys. Rev. Lett.*, 20(21):1205–1209, May 1968.

[4] J. Beringer et al. Neutrino mass, mixing and oscillations (2013 and partial update for 2014 edition). *Phys. Rev. D*, 86:010001, 2012.

[5] S. Fukuda et al. Solar ^8B and hep Neutrino Measurements from 1258 Days of Super-Kamiokande Data. *Phys. Rev. Lett.*, 86:5651–5655, Jun 2001.

[6] Q. R. Ahmad et al. Measurement of the Rate of $\nu_e + p \rightarrow p + p + e^-$ Interactions produced by ^8B Solar Neutrinos at the Sudbury Neutrino Observatory. *Phys. Rev. Lett.*, 87:071301, Jul 2001.

[7] Q. R. Ahmad et al. Direct Evidence for Neutrino Flavor Transformation from Neutral-Current Interactions in the Sudbury Neutrino Observatory. *Phys. Rev. Lett.*, 89:011301, Jun 2002.

[8] K. Eguchi et al. First Results from KamLAND: Evidence for Reactor Antineutrino Disappearance. *Phys. Rev. Lett.*, 90:021802, Jan 2003.

[9] A. Gando et al. Constraints on θ_{13} from a three-flavor oscillation analysis of reactor antineutrinos at KamLAND. *Phys. Rev. D*, 83:052002, Mar 2011.

[10] A. Gando et al. Reactor on-off antineutrino measurement with KamLAND. *Phys. Rev. D*, 88:033001, Aug 2013.

[11] Y. Fukuda et al. Evidence for Oscillation of Atmospheric Neutrinos. *Phys. Rev. Lett.*, 81:1562–1567, Aug 1998.

[12] Y. Ashie et al. Evidence for an Oscillatory Signature in Atmospheric Neutrino Oscillations. *Phys. Rev. Lett.*, 93:101801, Sep 2004.

[13] M. H. Ahn et al. Measurement of neutrino oscillation by the K2K experiment. *Phys. Rev. D*, 74:072003, Oct 2006.

[14] P. Adamson et al. Measurement of Neutrino and Antineutrino Oscillations Using Beam and Atmospheric Data in MINOS. *Phys. Rev. Lett.*, 110:251801, Jun 2013.

[15] K. Abe et al. First muon-neutrino disappearance study with an off-axis beam. *Phys. Rev. D*, 85:031103, Feb 2012.

[16] K. Abe et al. Measurement of Neutrino Oscillation Parameters from Muon Neutrino Disappearance with an Off-Axis Beam. *Phys. Rev. Lett.*, 111:211803, Nov 2013.

[17] Y. Itow. Recent results in atmospheric neutrino oscillations in the light of large θ_{13}. *Nucl. Phys. Proc. Suppl.*, 235-236:79–86, 2013.

[18] M. Apollonio et al. Search for neutrino oscillations on a long base-line at the CHOOZ nuclear power station. *Eur. Phys. J.*, C27:331–374, 2003.

[19] K. Abe et al. Indication of Electron Neutrino Appearance from an Accelerator-Produced Off-Axis Muon Neutrino Beam. *Phys. Rev. Lett.*, 107:041801, Jul 2011.

[20] K. Abe et al. Evidence of electron neutrino appearance in a muon neutrino beam. *Phys. Rev. D*, 88:032002, Aug 2013.

[21] K. Abe et al. Observation of Electron Neutrino Appearance in a Muon Neutrino Beam. 2013, 1311.4750.

[22] P. Adamson et al. Improved Search for Muon-Neutrino to Electron-Neutrino Oscillations in MINOS. *Phys. Rev. Lett.*, 107:181802, Oct 2011.

[23] P. Adamson et al. Electron Neutrino and Antineutrino Appearance in the Full MINOS Data Sample. *Phys. Rev. Lett.*, 110:171801, Apr 2013.

[24] F. P. An et al. Observation of Electron-Antineutrino Disappearance at Daya Bay. *Phys. Rev. Lett.*, 108:171803, Apr 2012.

[25] F. P. An et al. Improved measurement of electron antineutrino disappearance at Daya Bay. *Chinese Physics C*, 37:011001, 2013.

[26] J. K. Ahn et al. Observation of Reactor Electron Antineutrinos Disappearance in

the RENO Experiment. *Phys. Rev. Lett.*, 108:191802, May 2012.

[27] S.-H. Seo et al. New Results from RENO. *Proceedings of XVth International Workshop on Neutrino Telescopes*, March 2013.

[28] Y. Abe et al. Indication of Reactor ν_e Disappearance in the Double Chooz Experiment. *Phys. Rev. Lett.*, 108:131801, Mar 2012.

[29] Y. Abe et al. Reactor $\bar{\nu}_e$ disappearance in the Double Chooz experiment. *Phys. Rev. D*, 86:052008, Sep 2012.

[30] Y. Hayato. A Neutrino Interaction Simulation Program Library NEUT. *Acta Physica Polonica B*, 40(9):2477, Sep 2009.

[31] C. Andreopoulos et al. The GENIE neutrino Monte Carlo generator. *Nuclear Instruments and Methods in Physics Research A*, 614:87–104, February 2010, 0905.2517.

[32] C. H. Llewellyn-Smith. Neutrino Reactions at Accellerator Energies. *Phys. Rep.*, 3:261–379, 1972.

[33] E. J. Moniz and R. A. Smith. Neutrino Reactions on Nuclear Targets. *Nucl. Phys.*, B101:605–622, 1972.

[34] Omar Benhar and Adelchi Fabrocini. Two nucleon spectral function in infinite nuclear matter. *Phys.Rev.*, C62:034304, 2000, nucl-th/9909014.

[35] D. Rein and L. M. Sehgal. Neutrino-excitation of baryon resonances and single pion production. *Annals of Physics*, 133(1):79–153, 1981.

[36] M. Glück, E. Reya, and A. Vogt. Dynamical Parton Distributions Revisited. *Eur. Phys. J*, C5:461, 1998.

[37] A. Bodek and U. K. Yang. Modeling Neutrino and Electron Scattering Cross Sections in the Few GeV Region with Effective LO PDFs. *AIP Conf. Proc.*, 670:110–117, 2003.

[38] H. Surikko. *Neutrino 1979: International conference on neutrinos, weak interactions and cosmology (proceedings).* University of Bergen, 1980.

[39] E. Oset and L. L. Salcedo. Delta self-energy in nuclear matter. *Nuclear Physics A*, 468(3–4):631–652, 1987.

[40] A. Bodek, S. Avvakumov, R. Bradford, and H. Budd. Vector and axial nucleon form

factors: A duality constrained parameterization. *The European Physical Journal C*, 53(3):349–354.

[41] E. J. Moniz, I. Sick, R. R. Whitney, J. R. Ficenec, R. D. Kephart, and W. P. Trower. Nuclear Fermi Momenta from Quasielastic Electron Scattering. *Phys. Rev. Lett.*, 26:445–448, Feb 1971.

[42] J. Nieves, I. Ruiz Simo, and M. J. Vicente Vacas. Inclusive charged-current neutrino-nucleus reactions. *Phys. Rev. C*, 83:045501, Apr 2011.

[43] A. A. Aguilar-Arevalo et al. First measurement of the muon neutrino charged current quasielastic double differential cross section. *Phys. Rev. D*, 81:092005, May 2010.

[44] Cezary Juszczak, Jan T. Sobczyk, and Jakub Żmuda. Extraction of the axial mass parameter from MiniBooNE neutrino quasielastic double differential cross-section data. *Phys. Rev. C*, 82:045502, Oct 2010.

[45] Véronique Bernard, Latifa Elouadrhiri, and Ulf-G Meißner. Axial structure of the nucleon. *Journal of Physics G: Nuclear and Particle Physics*, 28(1):R1, 2002.

[46] V. Lyubushkin et al. A study of quasi-elastic muon neutrino and antineutrino scattering in the NOMAD experiment. *The European Physical Journal C*, 63(3):355–381, 2009.

[47] S. Boyd, S. Dytman, E. Hernández, J. Sobczyk, and R. Tacik. Comparison of Models of NeutrinoNucleus Interactions. *AIP Conference Proceedings*, 1189(1):60–73, 2009.

[48] L. AlvarezRuso. 2p2h or not 2p2h? *AIP Conference Proceedings*, 1405(1):71–76, 2011.

[49] G. A. Fiorentini, D. W. Schmitz, P. Rodrigues, et al. Measurement of Muon Neutrino Quasielastic Scattering on a Hydrocarbon Target at $E_\nu \sim 3.5$ GeV. *Phys. Rev. Lett.*, 111:022502, Jul 2013.

[50] L. Fields, J. Chvojka, et al. Measurement of Muon Antineutrino Quasielastic Scattering on a Hydrocarbon Target at $E_\nu \sim 3.5$ GeV. *Phys. Rev. Lett.*, 111:022501, Jul 2013.

[51] A. Bodek, H. S. Budd, and E. Christy. Neutrino quasielastic scattering on nuclear targets. *Eur. Phys. J. C*, 71:1726, 2011.

[52] A. Gil, J. Nieves, and E. Oset. Many-body approach to the inclusive (e, e') reaction

from the quasielastic to the Δ excitation region. *Nuclear Physics A*, 627(4):543–598, 1997.

[53] J. Nieves, J. E. Amaro, and M. Valverde. Inclusive quasielastic charged-current neutrino-nucleus reactions. *Phys. Rev. C*, 70:055503, 2004.

[54] R. E. Cutkosky. Singularities and Discontinuities of Feynman Amplitudes. *J. Math. Phys.*, 1:429, 1960.

[55] R. Gran, J. Nieves, F. Sanchez, and M. J. Vicente Vacas. Neutrino-nucleus quasi-elastic and 2p2h interactions up to 10 GeV. 2013, hep-ph/13078105.

[56] M. Martini, M. Ericson, G. Chanfray, and J. Marteau. A Unified approach for nucleon knock-out, coherent and incoherent pion production in neutrino interactions with nuclei. *Phys.Rev.*, C80:065501, 2009, 0910.2622.

[57] D. Beavis, A. Carroll, I. Chiang, et al. Physics Design Report, BNL 52459. 1995.

[58] K Abe et al. The T2K Experiment. *Nuclear Instruments and Methods in Physics Research Section A: Accelerators, Spectrometers, Detectors and Associated Equipment*, 659(1):106–135, 2011.

[59] S. Assylbekov et al. The T2K ND280 off-axis pi–zero detector. *Nuclear Instruments and Methods in Physics Research Section A: Accelerators, Spectrometers, Detectors and Associated Equipment*, 686(0):48–63, 2012.

[60] N. Abgrall et al. Time projection chambers for the T2K near detectors. *Nuclear Instruments and Methods in Physics Research Section A: Accelerators, Spectrometers, Detectors and Associated Equipment*, 637(1):25–46, 2011.

[61] P.-A. Amaudruz et al. The T2K fine-grained detectors. *Nuclear Instruments and Methods in Physics Research Section A: Accelerators, Spectrometers, Detectors and Associated Equipment*, 696(0):1–31, 2012.

[62] D. Allen et al. The electromagnetic calorimeter for the T2K near detector ND280. *Journal of Instrumentation*, 8:10019, Oct 2013.

[63] M. Scott. *Measuring charged current neutrino interactions in the electromagnetic calorimeters of the ND280 detector*. PhD thesis, Imperial College London, 2013.

[64] S. Aoki et al. The T2K Side Muon Range Detector (SMRD). *Nuclear Instruments and Methods in Physics Research Section A: Accelerators, Spectrometers, Detectors*

and Associated Equipment, 698(0):135–146, 2013.

[65] Y. Fukuda, T. Hayakawa, E. Ichihara, Ishitsuka M., Y. Itow, et al. The Super-Kamiokande detector. *Nuclear Instruments and Methods in Physics Research Section A: Accelerators, Spectrometers, Detectors and Associated Equipment*, 501(2–3):418–462, 2003.

[66] K. Abe et al. T2K neutrino flux prediction. *Phys. Rev. D*, 87:012001, Jan 2013.

[67] N. Abgrall et al. Pion emission from the T2K replica target: Method, results and application. *Nuclear Instruments and Methods in Physics Research Section A: Accelerators, Spectrometers, Detectors and Associated Equipment*, 701(0):99–114, 2013.

[68] R. Brun and F. Rademakers. ROOT: An object oriented data analysis framework. *Nucl.Instrum.Meth.*, A389:81–86, 1997.

[69] Agostinelli, S. and others. Geant4: a simulation toolkit. *Nuclear Instruments and Methods in Physics Research Section A: Accelerators, Spectrometers, Detectors and Associated Equipment*, 506(3):250–303, 2003.

[70] P. de Perio et al. Constraining the Flux and Cross Section Models with Data from the ND280 Detector for the 2012a Oscillation Analysis. *T2K-TN-106*, 2012.

[71] K. Abe et al. Measurement of the inclusive ν_μ charged current cross section on carbon in the near detector of the T2K experiment. *Phys. Rev. D*, 87:092003, May 2013.

[72] P. de Perio et al. Cross section parameters for 2012 oscillation analysis . *T2K-TN-108*, 2012.

[73] A. A. Aguilar-Arevalo et al. Neutrino flux prediction at MiniBooNE. *Phys. Rev. D*, 79:072002, April 2009.

[74] G. D'Agostini. On the use of the covariance matrix to fit correlated data. *Nucl. Instrum. and Methods A*, 346(12):306 – 311, 1994.

[75] H. S. Budd, A. Bodek, and J. Arrington. Modeling quasielastic form-factors for electron and neutrino scattering. 2003, hep-ex/0308005.

[76] R. Bradford, A. Bodek, H. Budd, and J. Arrington. A New Parameterization of the Nucleon Elastic Form Factors. *Nuclear Physics B - Proceedings Supplements*,

159(0):127 – 132, 2006.

[77] T. Dealtry et al. Studies of the Effect of Neutrino-Multinucleon Interactions in the 2013 Disappearance Analysis. *T2K-TN-172*, 2013.

[78] J. T. Sobczyk. Multinucleon-ejection model for two-body-current neutrino interactions. *Phys. Rev. C*, 86:015504, Jul 2012.

[79] Roger D. Woods and David S. Saxon. Diffuse surface optical model for nucleon-nuclei scattering. *Phys. Rev.*, 95:577–578, Jul 1954.

[80] C. Bojechko et al. CC-multiple-pion ν_μ event selections in the ND280 tracker using Run 1+2+3+4 data. *T2K-TN-152*, 2013.

[81] C. Bojechko and A. Kaboth. Muon neutrino disappearance simultaneous fit of ND280 and SK with Run 1+2+3 data using Markov Chain Monte Carlo analysis. *T2K-TN-140*, 2013.

[82] R. Calland et al. Joint ND280 and SK 3-flavor oscillation fit using Markov Chain Monte Carlo (MaCh3). *T2K-TN-171*, 2014.

[83] W. K. Hastings. Monte carlo sampling methods using markov chains and their applications. *Biometrika*, 57(1):97–109, 1970.

[84] M. Hartz et al. Constraining the Flux and Cross Section Models with Data from the ND280 Detector for the 2013 Oscillation Analysis. *T2K-TN-166*, 2013.

[85] Andrew Gelman, Xiao li Meng, and Hal Stern. Posterior predictive assessment of model fitness via realized discrepancies. *Statistica Sinica*, pages 733–807, 1996.